2008

Molecular-Beam Mass-Spectrometric Analyses of Hydrocarbon Flames

Saugata Gon
University of Massachusetts Amherst

MOLECULAR-BEAM MASS-SPECTROMETRIC ANALYSES OF HYDROCARBON FLAMES

A Thesis Presented

by

SAUGATA GON

Submitted to the Graduate School of the
University of Massachusetts Amherst in partial fulfillment
Of the requirements for the degree of

MASTER OF SCIENCE IN CHEMICAL ENGINEERING

FEBRUARY 2008

MOLECULAR-BEAM MASS-SPECTROMETRIC ANALYSES OF HYDROCARBON FLAMES

A Thesis Presented

By

SAUGATA GON

Approved as to style and content by:

_____

Phillip R. Westmoreland, Chair

_____

T. J. Mountziaris, Member

_____

Dimitrios Maroudas, Member

_____

T. J. Mountziaris, Department Head
Department of Chemical Engineering

ACKNOWLEDGEMENTS

I would like to thank my advisor Prof. P. R. Westmoreland for giving the opportunity to work with him. I had several ups and downs during this study and he was there, all through to encourage me. He was very patient, understanding and supportive. I just want to say thank you Phil. During this study I got several feedbacks from my committee members Prof. Maroudas and Prof. Mountziaris. I want to take this opportunity to thank them for their eager help and advice, without which it would have been very difficult for me. I want to thank our LBNL team, Dr. Nils Henson, Prof. Terrill Cool, Juan Wang, Patrick Osswald and Tina Kasper for their help and support during getting the experimental data from ALS.

I would also like to thank my group members, specially Matt Law, Ken Smith, Aurelie Schoemann, Sonia Tulyani, Wenjun Li and Nicole Labbe for their help and feedback on my work. My friends have been a great support for my stay in Amherst. Without their help and support it would not have been possible to see this far. So I would like thank all of my friends and class mates for their help. After coming to an unknown country, the company and support I got from my roommates and seniors made my stay enjoyable here. So I would like to thank Souvik, Prashant, Nilesh, Deepak and Manish for being there for me as friends.

Support for this project by the U. S. Department of Energy, under grants DE-FG02-91ER14192 is greatly acknowledged.

ABSTRACT

MOLECULAR-BEAM MASS-SPECTROMETRIC ANALYSES OF HYDROCARBON FLAMES

FEBRUARY 2008

SAUGATA GON, B.TECH., Ch.E, HALDIA INSTITUTE OF TECHNOLOGY, HALDIA, INDIA
M. TECH., Ch.E, INDIAN INSTITUTE OF TECHNOLOGY BOMBAY, POWAI, MUMBAI, INDIA
M.S. Ch.E, UNIVERSITY OF MASSACHUSETTS AMHERST

Directed by: Professor Phillip R. Westmoreland

Laminar flat flame combustion has been studied with molecular-beam mass-spectrometry (MBMS) for a fuel-rich cyclohexane ($\Phi = 2.003$) flame, a fuel-lean toluene ($\Phi = 0.895$), and a fuel-rich toluene ($\Phi = 1.497$) flame. Different hydrocarbon species in these flames were identified, and their mole fraction profiles were measured. The information can be used to propose reaction mechanisms for the different hydrocarbon flames.

One MBMS apparatus located at Advanced Light Source (ALS) at Lawrence Berkeley National Laboratory was used to identify and measure the mole-fraction profiles of different species in these flames. The MBMS apparatus located at University of Massachusetts Amherst was used to measure the temperature profile of the cyclohexane flame. The temperature profile of two different fuel-rich toluene flames (Φ= 2.02 , $\Phi = 3.94$) and a fuel-lean (Φ=0.452) methane flame were also measured with the UMass apparatus.

TABLE OF CONTENTS

Page

APPENDICES

LIST OF TABLES

LIST OF FIGURES

CHAPTER 1

INTRODUCTION

Combustion can be broadly defined as a series of self-sustaining exothermic reactions. Combustion with the ability to propagate through a suitable reaction medium can be called a flame (Fristrom, 1995). Flames constitute a particularly complex phenomenon representing a strong coupling between chemical reactions and heat, momentum, and species transport processes (Stavropoulos, 2005). We see the application of combustion in our everyday life. Its applicability has spread from our kitchen to the power plants, from automobiles to spacecrafts. Despite the long history of combustion in human society, its quantitative understanding is relatively new, because of the complexity involved in combustion. To find some of the answers to the numerous riddles of combustion, we study premixed laminar flames with flat flame structure. A general description of this type of flame is given below.

1.1 Premixed laminar flame

As the name suggests, the gaseous fuel and oxidizer are premixed on the molecular level and the flow is laminar in a premixed laminar flame. Such a flame is most easily visualized as a thin reaction sheet separating unburned from burned gases and propagating normal to themselves at a characteristic velocity. This surface can be approximately identified with the thin luminous zone characteristic of common flames (Fristrom, 1995).

Based on the flow characteristics of the fuel-oxidizer mixture, a flame can form several structures. The flat flame is one of them. The premixed fuel-oxidizer mixture is passed through a water-cooled sintered plate, which produces a uniform velocity field, and when ignited, it forms a flat flame structure. In a flat flame, the temperature gradient along the radial direction is negligible. As a result, the diffusion of the species along the radial direction can also be neglected. Hence these flames can be described with one-dimensional transport models.

1.2 The motivation

It is hard to detect the unstable species in a combustion process because of the lack of suitable techniques. However, combustion studies with molecular-beam mass spectrometry (MBMS) have been able to solve this aspect of the problem to some extent. With the help of MBMS, new insights can be obtained into several reaction pathways in combustion for better understanding. Combustion processes may produce air-toxic pollutants as byproducts, especially at fuel-rich combustion. The formation of intermediate products like polycyclic aromatic hydrocarbons (PAH) and soot occurs under fuel-rich conditions in the flames. Because radiation from soot particles dominates the energy transfer in large fires, soot formation influences the combustion efficiency in furnaces. Particle formation and amount of energy transfer control smoke production, which is important for fire detection (Smyth and Miller, 1987). All these issues couple to motivate the study hydrocarbons flames to bring insights into production of soot.

1.3 Research objectives

Research objectives for this project include understanding the flame microstructure of different premixed laminar hydrocarbon flames in detail. Characterizing the flame microstructure requires identifying the different products in a particular flame, mapping them spatially, and measuring the temperature profile for the flame. The bigger objectives behind this approach were to understand the molecular growth chemistry of higher hydrocarbons and to investigate the oxidation chemistry of these hydrocarbons. Mainly two flames were studied for this purpose, a fuel-rich cyclohexane flame ($\Phi = 2.003$) and a lean toluene flame ($\Phi = 0.895$). A fuel-rich toluene flame ($\Phi = 1.497$) was also studied, but further experiments are required for that flame.

1.4 Hydrocarbon combustion - An overview

1.4.1 Different reaction zones, reaction products, radical reactions

The combustion of hydrocarbons can be broadly categorized as oxidation. The final byproducts would be CO_2 and H_2O if combustion to fully oxidized products were complete. Equation 1.1 describes the overall combustion reaction for an ideal, stoichiometric combustion process of a hydrocarbon.

$$C_xH_y + (x+y/4)\ O_2 = xCO_2 + y/2\ H_2O \qquad (1.1)$$

In reality, all the carbon and hydrogen may not get fully oxidized during the combustion process, and some of the species may remain partially oxidized to form CO and H_2. The intermediate species that are formed in the process of getting to CO_2 and

H_2O make combustion an interesting problem chemically. The reaction-pathway analysis for these intermediates can lead to insights into the formation of major pollutants like PAHs and soot. It can be broadly said that the final products found in the post-flame zone of almost all fuel-rich hydrocarbon fuels are CO, CO_2, C_2H_2, H_2 and H_2O (Homann and Wagner, 1968). Other types of species observed in the flames are polyacetylenes, intermediate hydrocarbons, oxygenates, and PAH like naphthalene, phenanthrene, pyrene, and coronene.

Radicals play a crucial role in combustion. The reactions associated with radicals can be broadly categorized as four types (Borghi and Destriau, 1998):

- **Initiation.** When a radical is produced in the flame from a nonradical, the process is called initiation.
- **Chain Propagation.** When a radical reacts with a molecule or atom to produce another radical, the process is called chain propagation.
- **Chain Branching.** When one radical gives rise to more than one radical, the process is called chain branching.
- **Chain Termination.** When the radical recombination gives rise to formation of stable species, the process is called chain termination.

There are three zones that are observed in an laminar premixed flat flame. These zones can be explained in terms of the radical reactions described above. The zones are:

- **Preheat Zone.** The fuel-oxidizer mixture travels a small distance before it is ignited. This region close to the burner and just underneath the flame is called the preheat zone. Some of the radicals that get produced in the flame zone undergo molecular or thermal diffusion, diffuse back to the fuel-oxidizer mixture in this

zone, and are terminated. The temperature in this region is not high, and heating occurs mainly by conduction from the hotter flame zone back to the burner (Dixon-Lewis, 1979).

- **Luminous Flame Zone.** This is the hottest region in the flame. Chain initiation, propagation, and branching reactions occur here. This zone is also termed as the oxidation zone. Various hydrocarbon intermediates go through maxima in this zone, and molecular oxygen gets almost used up by the end of flame zone (Homann and Wagner, 1968).
- **Post-Flame Zone.** This zone is downstream of the flame zone. Mostly chain-termination reactions occur in this zone. Mostly CO, CO_2, H_2O, radicals, and unburned hydrocarbons are present in this zone.

The reactions between oxygen and hydrogen are the core of the hydrocarbon combustion reactions. According to Dixon-Lewis (1979), the important hydrogen-oxygen chemistry information is found from the following reactions:

$$OH + H_2 \rightarrow H_2O + H \quad (1.2)$$

$$H + O_2 \rightarrow OH + O \quad (1.3)$$

$$O + H_2 \rightarrow OH + H \quad (1.4)$$

$$H + O_2 + M \rightarrow HO_2 + M \quad (1.5)$$

$$H + HO_2 \rightarrow O + H_2O \quad (1.6)$$

$$H + HO_2 \rightarrow O_2 + H_2 \quad (1.7)$$

$$OH + HO_2 \rightarrow O_2 + H_2O \quad (1.8)$$

$$O + HO_2 \rightarrow OH + O_2 \quad (1.9)$$

$$H + H + M \rightarrow H_2 + M \quad (1.10)$$

$$H + OH + M \rightarrow H_2O + M \quad (1.11)$$

$$H + O + M \rightarrow OH + M \quad (1.12)$$

$$OH + OH \rightarrow H_2O + O \quad (1.13)$$

Dixon-Lewis (1979) suggested that the heat release occurred principally by reaction 1.5, followed by one of 1.6, 1.7, 1.8 or 1.9 of HO_2 with H, OH or O, and then, where appropriate, by one or both of 1.2 and 1.4 to reform H. These heat-releasing reactions depend on the radicals being produced by reaction 1.2, 1.3 and 1.4 in the hotter region of the flame. The radicals diffuse upstream to meet O_2 and react with it by reaction 1.5. The radical recombination reactions 1.10, 1.11 and 1.13 are coupled with this process, but these three reactions can dominate only in the absence of O_2 because of competition with reaction 1.5.

1.4.2 Hydrocarbon growth chemistry

Smyth and Miller (1987) suggested that soot formation is influenced by two major steps.

i) Production of precursor molecules, which react rapidly to give larger species;

ii) Chemical growth that results in formation of several small primary particles.

Different models have been proposed with different precursors for soot. Homann and Wagner (1967) suggested that polyacetylene plays the major role in soot formation. Calcote (1981) suggested that the precursor would be chemiions on which free radicals, polyacetylenes and PAHs add in repeatedly in fast ion-molecule reactions and produce soot. Benson (1982) suggested that neutral radicals are the most significant intermediate.

Smyth and Miller (1987) suggested that vinyl and ethynyl radicals are important precursors to benzene and that benzene in turn is an important precursor to soot formation; however, McEnally and Pfefferle (2004) suggested that benzene formation is not the rate-determining step for soot formation in non-premixed flames. Öktem et al. (2005) suggested during particle inception and initial growth the PAHs contribute significantly, but after a stage, aliphatic compounds can also play a major role in soot formation.

As benzene is widely considered as an crucial intermediate to PAH formation, detailed research work has been done on understanding the benzene formation pathway. According to Westmoreland et al. (1989), three main reaction pairs have been suggested for benzene formation. $C_2 + C_4$, $C_3 + C_3$ and $C_1 + C_5$ species. Among these three, the most widely accepted mechanism is Hydrogen Abstraction / Carbon Addition or the HACA mechanism ($C_2 + C_4$), suggested by Wang and Frenklach (1997). Law (2005) found that with a stoichiometric cyclohexane flame, a dehydrogenation mechanism is the major benzene formation pathway.

Zervas et al. (2004) empirically found that benzene formation increases with high fuel equivalence ratio from a SI engine. They also found that with addition of oxidants, the soot formation decreased. This result supports the idea that for understanding molecular weight growth in hydrocarbons, fuel-rich flames should be studied.

1.5 Molecular-beam mass spectrometry (MBMS)

Molecular-beam mass spectrometry has long been recognized to be one of the most powerful techniques in analyzing flame structure (Biordi, 1977; Turbiez et al.,

1999). Molecular-beam sampling probes coupled with mass-spectrometric detection can detect species that are unstable to wall and/or gas collisions, such as atoms, radicals, and highly reactive stable species (Biordi, 1977).

1.5.1 General idea of the MBMS apparatus

A molecular-beam mass spectrometer system consists of a source combustion chamber, source orifice, source chamber, skimmer, collimation chamber, collimating orifice, detection chamber and mass-spectrometer detector (Knuth, 1973). Under conditions of vacuum, the source gas expands via the source orifice into the source chamber. The skimmer transfers the core of the free jet into the collimating chamber. The collimating orifice passes those molecules flying near the system centerline into the detection chamber. The mass spectrometer then is used to generate a signal proportional to the species density in the beam at the detector. Based on the conditions of operation, the molecular beam can be of two types, as discussed below.

1.5.2 Beams from effusive sources

Anderson et al. (1965) defined beams from effusive sources as classical oven beams. According to them, the beam source, which can be called an oven, is a cavity that communicates with an evacuated chamber through a small orifice or slit. They further pointed out that if the gas density in the oven is such that the mean free path (the average distance between collisions for a gas molecule) is greater than the diameter of the orifice, then there would be effusive flow of molecules into the evacuated chamber. In other words, the molecules would wander through the orifice without colliding with each other.

Due to the low intensity of the beam from effusive sources (Biordi, 1977), this type of beam is not desirable to flame sampling. It was early proposed that the oven beams could be replaced by supersonic jets (Anderson et al., 1965).

1.5.3 Beams with supersonic jets

The present work uses nozzle beams. Biordi (1977) noted that if the mean free path, λ, of a gas flowing through the orifice is small relative to the orifice diameter, d (i.e. if $\lambda/d \equiv Kn_0 << 1$, where the subscript zero refers to source condition and Kn_0 is Knudsen number) and if the pressure ratio across the orifice is sufficiently large ($10^5 - 10^6$), then the gas flow across the orifice is supersonic and the initial stage of expansion may be treated as isentropic expansion of a macroscopic bulk fluid. Anderson et al. (1965) described this type of beam as a beam from a nozzle source. According to Biordi (1977), as the gas expands across the orifice, it experiences a rapid reduction in temperature and collision frequency, and molecular flow prevails. This expansion quenches the chemical reactions occurring in the source and species such that atoms and radicals may survive. A skimmer isolates the central portion of the beam. Thus, one can discriminate against the peripheral region of the beam, which can be expected to have some interactions with the cone walls.

During the course of this study, two molecular-beam mass spectrometers were used. One in the laboratory at the University of Massachusetts Amherst, which will be referred as the UMass equipment, and the other is at the Advanced Light Source of the Lawrence Berkeley National Laboratory in Berkeley, California. This system will be referred as the ALS equipment.

CHAPTER 2

EXPERIMENTAL EQUIPMENT AND PROCEDURES

During the course of this study, two molecular-beam mass spectrometers were used. One is in the Westmoreland laboratory at the University of Massachusetts Amherst, which will be referred as the UMass equipment, and the other is at the Advanced Light Source of the Lawrence Berkeley National Laboratory in Berkeley, California. This system will be referred as the ALS equipment.

2.1 UMass equipment

The original equipment incorporated into the MBMS apparatus at the University of Massachusetts Amherst was built by Biordi, Lazzara, and Papp (1973) at the Pittsburgh Mine and Safety Research Center of the U.S. Bureau of Mines, Pittsburgh, PA. The Westmoreland research group at the University of Massachusetts Amherst acquired the system in 1986, and thereafter the group has made several modifications in the system. Figure 2.1 shows a schematic diagram of the UMass equipment. The different parts of the equipment will be described under the equipment description section, and the feed delivery will be covered subsequently.

2.1.1 Equipment description

The reaction chamber of the UMass equipment is a vertical cylindrical chamber of 45.7 cm diameter and 48.3 cm height. It was built of steel with an alumina (Al_2O_3) coating inside. It has several small ports for windows and feedthroughs. A large window (8 cm x 12 cm) is used for viewing and maintenance. A 5.3-cm-diameter circular window

is used for viewing and positioning the igniter on top of the burner. This window is on the right side of the chamber when the large window is faced. An identical viewing window of diameter 5.3 cm is on the left side of the reaction chamber. When the temperature measurements are conducted, the thermocouple probe is mounted through this opening.

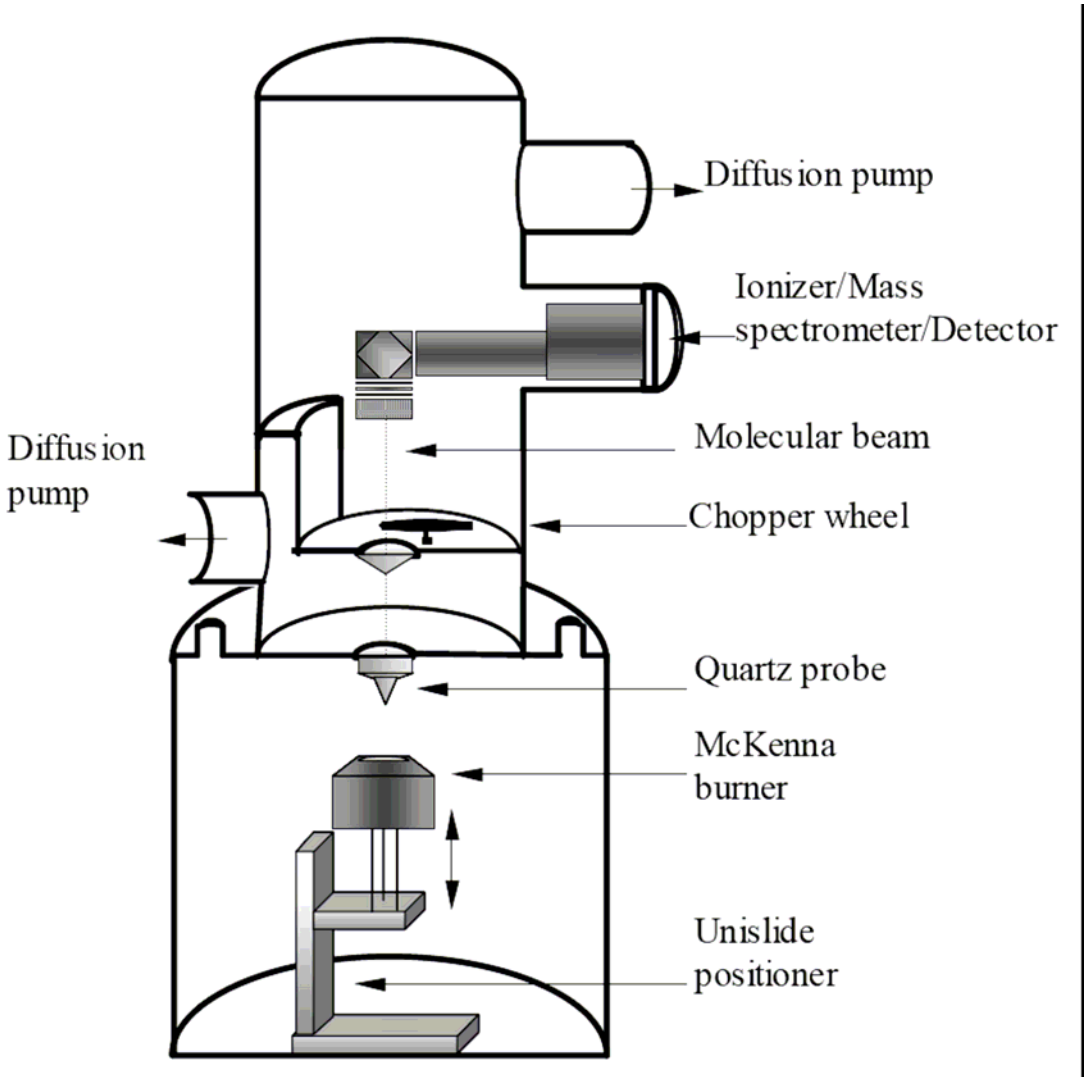

Figure 2.1. Schematic of the UMass molecular-beam mass spectrometer system.

Inside the chamber, a 6.03-cm-diameter, McKenna-type burner (Holthuis & Associates) is mounted on a positioning system (Velmex Unislide), which can move the burner toward the sampling quartz cone (axially) or normal to this axis (radially). A code written by Law (2005) in LabVIEW (National Instruments, Inc.) can control the movement of the burner. The burner must be water-cooled when a flame is lit. A water inlet line, a water outlet line, a fuel gas line and a shroud argon inlet line are connected to the burner. As argon shroud is found to diffuse into the flame away from the burner (Morel, 2005), the shroud argon inlet is not used.

Two single-stage pumps (Busch RS super series) are used to create the vacuum in the combustion chamber. One of them has 20 CFM pumping capacity (BP – RA0025101) while the other one (BP – RA0040101) has a 28 CFM pumping capacity. The Busch pumps need to be shut off after every 10 hours of operation to allow opening the check valve to drain back the oil that is collected in the exhaust filter (Busch maintenance and repair manual). [An effort is underway to connect the chamber to a 300 CFM Stokes pump (CB82518). The Stokes pump would be able to take the load off the Busch pumps and would deliver a continuous pumping capability.] The chamber pressure is maintained mainly by the gate valve between the Busch pumps and the chamber and more precisely by a control valve (MKS 0248A) that introduces a ballast flow of air and maintains the pressure within ± 0.01 Torr from the set point.

The chamber pressure is read approximately by a Bourdon-tube pressure gauge (Wallace and Tiernan FA160 with a range of 0 to 800 Torr) and precisely by a diaphragm-deflection gauge (MKS Baratron, 50230-1-5) which has a maximum pressure range of 100 Torr.

In the present work, this system's capabilities for molecular-beam sampling and quadrupole mass spectrometry were not used and so are not described further here. The interested reader may refer for its details to Law (2005).

2.1.2 Feed delivery system for the UMass system

The flames that were studied with the UMass system were toluene, cyclohexane and methane. Methane is a gas at room temperature but toluene and cyclohexane are liquid at room temperature, therefore both liquid and gas delivery systems were required. The fuel is mixed with premixed with oxygen and argon and then fed into the burner. The schematic of the feed delivery system is given in Figure 2.2.

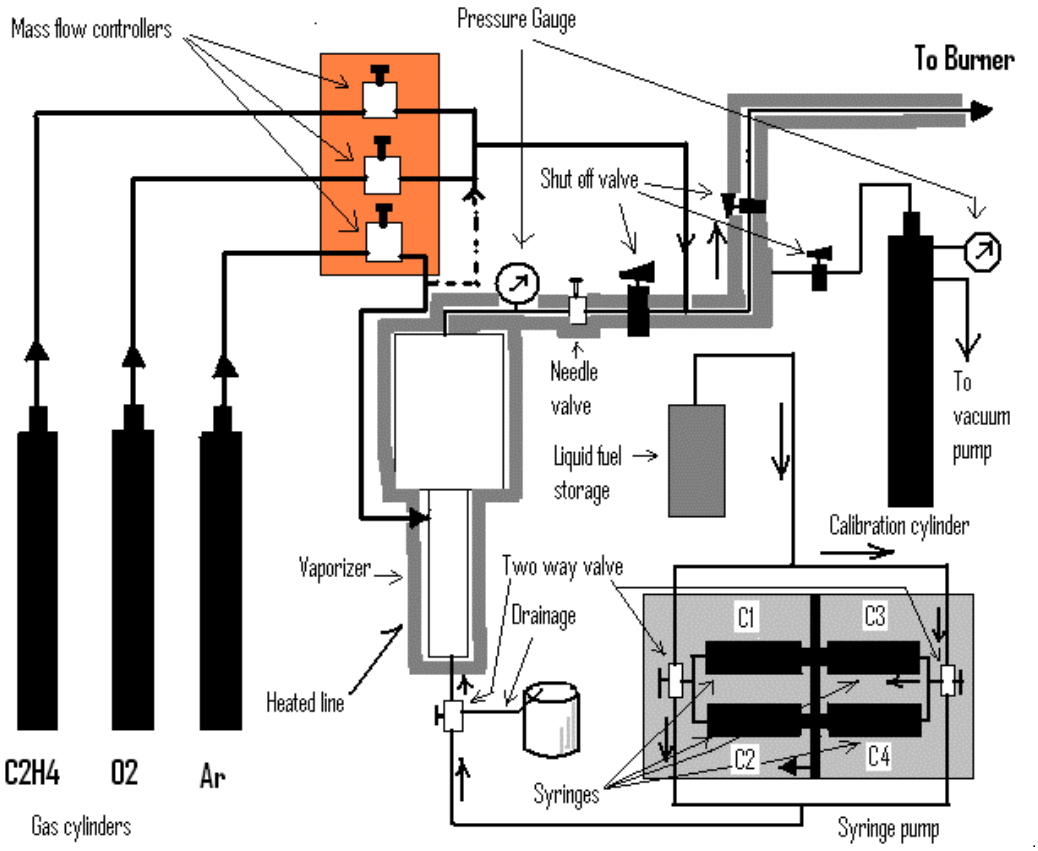

Figure 2.2. Feed delivery system for the UMass system.

Gas feed delivery system. Argon and oxygen were gases used in all the flames studied with the UMass apparatus. Ethylene was used as a fuel to ignite the flame before introducing vapor-phase feed of the liquid fuels toluene and cyclohexane. The gases were metered with individual mass flow controllers (MKS Instruments 2259 B with a MKS 247-C power supply and read-out). The gases were premixed in heat-traced, stainless-steel tubing (approximately 23 ft long).

Gas flow rates were calibrated by flowing the gas into a calibration cylinder with a volume of 43.364 liters. The pressure rise in the cylinder was noted at different times, and the molar flow rate was calculated using the ideal gas law. The calibration of argon and oxygen for the fuel-rich cyclohexane flame is presented in Appendix A.1. The MKS Baratron gauge that reads the chamber pressure is also used to read the pressure in the calibration chamber. As the Baratron can read the pressure only up to 100 Torr, when the pressure in the cylinder rises to 100 Torr, gas flow is stopped and the calibration cylinder is evacuated using a vacuum pump. As the pressure lowers below 10 Torr, the vacuum line is closed and gas flow into the cylinder is resumed.

Liquid feed delivery system. The liquid delivery system has two main components, the syringe pump and the vaporizer.

A Harvard Apparatus PHD 2000 syringe pump was used to deliver the liquid. It operates four 50-ml glass syringes. The pump operates with a push/pull mechanism. While two syringes deliver the liquid, the other two syringes get refilled. Two two-way valves alternate flow from the feed line or to the delivery line for the syringes. The arrow in Fig. 2.2 refers to the motion of the plungers in the syringe pumps. When one set of syringes approaches empty, the other set becomes almost filled. Then the pump is

stopped briefly, the delivery mode of the pump (infuse/refill) is changed, and the flow paths for the two-way valves are switched, and the pump is re-started. This sequence takes care of continuous delivery of liquid to the vaporizer with a small transition time while altering the pump motion.

The required flow rate can be set for the pump, and the pump generally obeys its set point quite accurately. However, when high flow rate through the pump is required, the actual flow delivered starts deviating from the set point. A calibration curve given in Appendix A.2 gives this variation. In order to get the calibration curve, the syringes are filled with water, a required flow rate is set in the syringe pump, and then the pump is run for a certain time. The water coming out of the syringe is collected in a beaker of known weight, and then sample is weighed. The room temperature is noted, and water density at that temperature is looked up. From the density and the weight of the water sample, the volume of the water collected in a known time period is found out, and thus the exact volumetric flow rate delivered by the syringe pump can be calibrated.

The liquid from the syringe pump then goes into the vaporizer. It is a cylindrical pipe (2.2 cm diameter and 14.9 cm long) wrapped with heating tape. A variable-voltage transformer (Variac) is used to control the heating tape. The liquid fed into the vaporizer forms a liquid pool at the bottom of the vaporizer and gets vaporized continuously. A K-type thermocouple is placed just above the pool of vaporizing gas. A digital thermometer (Omega 650) reads the temperature from the thermocouple. The temperature in the vaporizer is set high above the boiling point of the liquid fuel.

The diluent gas argon is fed to a ¼-inch tube connecting the vaporizer and a surge volume. The argon serves as a carrier gas for the vaporized fuel, and it also maintains the

pressure in the vaporizer. The fuel and the diluent enter a constriction volume. The purpose of the constriction volume is to diminish any fluctuation in the flow of liquid fuel vapor.

The vapor and the diluent gas mixture then reach the surge volume, which further diminishes the fluctuations in the flow. The pressure in the surge volume is controlled by a needle valve. The pressure in the surge volume needs to be at atmospheric pressure. If the pressure becomes higher than atmospheric pressure, it would push the liquid out of the syringes in the syringe pump. If the pressure in the surge volume is far lower than one atmosphere, air would be sucked into the syringes. This limitation is solely due to the operating-range pressure limitation of the syringe pump.

The downstream line of the vaporizer that goes into the burner is made of stainless steel. Approximately 23 feet of stainless-steel tubing is used to premix the argon, fuel vapor and oxygen before it is fed to the burner. The tubing is heated with heating tape to prevent formation of liquid droplets. Four variable-voltage transformers are used to heat the tubing. Three K-type thermocouples are used to read the temperature of the tubing at three different points.

2.2 ALS equipment

The MBMS apparatus situated at the Advanced Light Source (ALS) Laboratory of the Lawrence Berkeley National Laboratory was built in an combined effort of Prof. Terrill Cool of Cornell University, Prof. Phillip R. Westmoreland of University of Massachusetts Amherst, and Dr. Andrew McIlroy of Sandia National Laboratories.

The ALS apparatus is similar to the UMass apparatus. The main difference between the two apparatuses lies in the method of ionization and the mass spectrometers used for the two apparatuses.

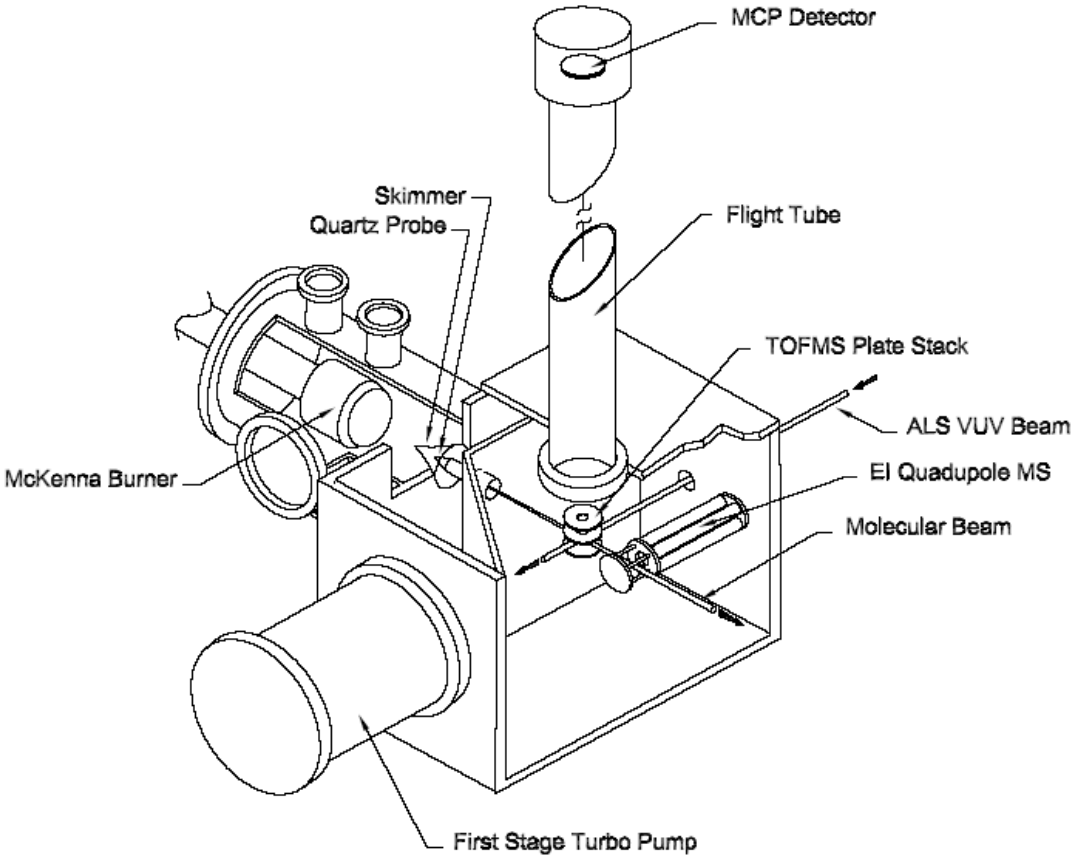

Figure 2.3. Schematic of the ALS system.

A sketch of the ALS system is given in Fig. 2.3; details are reported in Cool et al. (2005) and summarized here. At the ALS, photon beams are generated within a narrow energy distribution. The photon energy can be tuned and the sampled molecular beam can be ionized at a desired energy ranging from 7.5 to 24 eV. The photon beam is passed through a gas filter to remove higher harmonics of the photons. Argon is used in the gas

filter when using photon energies below the ionization energy of argon (15.76 eV). Argon is replaced by helium when higher energy is required. The photon beam then passes through a slit filter that adjusts the flux of photons sent to the MBMS system. A silicon photodiode is used to measure the variation in photon flux with photon energy for photon energies from 8 to 15 eV.

2.2.1 Equipment description

The reaction chamber is an axially horizontal, cylindrical, stainless-steel chamber. A 6-cm diameter, internally water-cooled, McKenna-type flat-flame burner is located inside the chamber. The burner is translatable along the horizontal direction of flow with a computer-controlled stepper motor. A mechanical pump pumps the exhaust from the chamber, and an automated MKS control valve on the exhaust line with feedback control can maintain constant pressure ranging from 20 to 60 Torr. A tungsten-wire flame-ignition source is used to ignite the fuel. Two circular windows are there for viewing and maintenance-access purposes.

The molecular-beam sampling train is similar to the UMass equipment. The sample is collected by a quartz cone and the beam goes through a skimmer. A turbomolecular pump maintains low pressure of the order of 1.0×10^{-4} Torr or lower in the skimmer chamber.

Several turbomolecular pumps maintain low pressure in the mass-spectrometer chamber. The photon beam enters the main test chamber through a differentially pumped aperture, designed to ensure that the pressure at the exit slit does not exceed 2.0×10^{-8} Torr. Three plates are at the bottom of the time-of-flight mass spectrometer (TOFMS).

The bottom plate is called as the repeller, the middle one is the extractor, and the top one is called an accelerator. The photon beam intersects the molecular beam at the ionization source region between the repeller and extraction plates of the TOFMS. Cool et al. (2005) found optimal plate voltages to be 2997, 3005, and 0 V respectively for the repeller, extractor, and accelerator. They justified the 8-V potential difference between extractor and the repeller plates as a discriminator to reduce a small random background signal caused by ions escaping the source region. A pulsed voltage is applied to the repeller plate to propel ions up the 1.3-m flight tube to a multichannel plate (MCP) detector. Because of their differences in mass, different species hit the MCP at different times and are separated. The pulsed gating voltage applied to the repeller has 300 V amplitude and 15 kHz frequency. A multiscaler (FAST Comtec P7886) is used to record the TOFMS mass spectra. One pulse of mass spectrum is one sweep. Depending upon the signal strength of the species of interest, 2^{18} to 2^{21} sweeps are added together to form one data point of the mass spectrum (Law, 2005). Signals are sent to a desktop computer, and a custom LabVIEW code processes the data.

2.3 Experimental procedures

The experimental procedures can be broadly categorized into two classes, (1) species identification and measurement and (2) temperature measurement. The species identification and measurement of burner scan profiles were done with the ALS equipment, and the temperature measurement were done with the UMass equipment. The details of these experimental procedures are illustrated below.

2.3.1 Species measurements and identifications

A full characterization of a flame includes identifying the different species present in the flame and measuring their profiles along the flame axis. Species identification is done by analyzing photoionization efficiency (PIE) scans, and mole fraction profiles are obtained from burner scans. Detailed descriptions of both processes are described below.

2.3.1.2 Photoionization efficiency (PIE) scan

Photoexcitation is a process where an atom can absorb radiation and rise from a normal, ground state to an excited state. The Bohr relation connects the energy difference and the frequency of the radiation absorbed.

$$h\nu_{ul} = (V_u - V_l)e = V_c e \tag{2.1}$$

where ν_{ul} is the frequency of the radiation absorbed in a transition from a state of energy eV_l to eV_u . The absorption lines corresponding to transitions from a particular initial state form a spectral series. As the wavelengths become shorter, the wavelength difference between successive transitions decreases and the series converges on a series limit. Beyond this limit, there is region of continuous absorption, which is called photoionization (Marr, 1967).

The ionization energies (the minimum energy required to remove an electron from the outermost orbital of a neutral species) for different species are different. In the PIE scan, the burner is positioned at a fixed distance from the quartz sampling probe and the photon energy is changed from a low to a higher energy. Different species appear at different energies, and based on the appearance potential and mass, we can identify a particular species. It has been found that most of the hydrocarbon and C/H/O species in a

given flame appear in the energy range between 8.0 to 10.8 eV. At high photon energies, there is significant fragmentation of ions, therefore a scan at very high energies is not useful for these species. The flame species H_2O, O, O_2 , CO, CO_2, H_2, H, OH appear at higher energies.

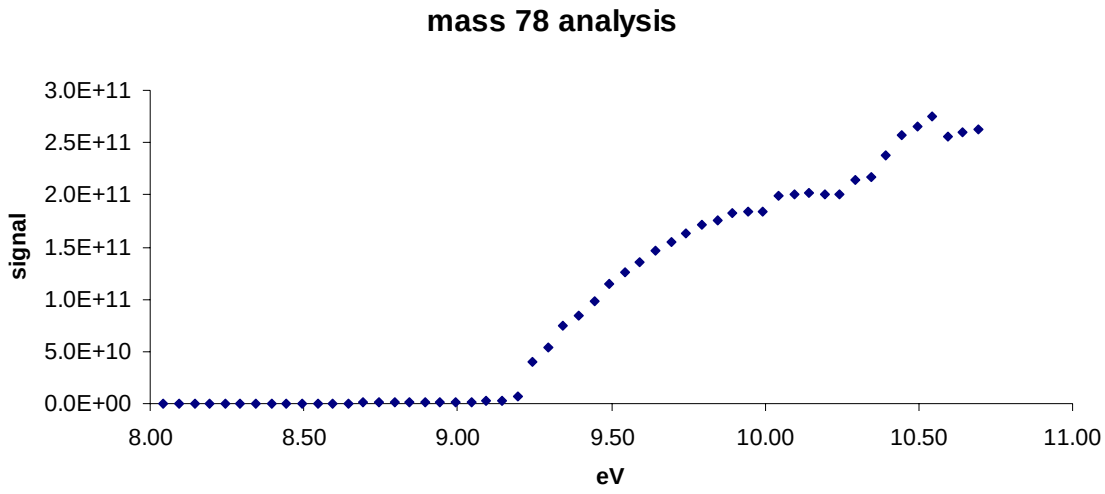

Figure 2.4. PIE scan analysis of mass 78 in the fuel-rich cyclohexane flame.

Figure 2.4 shows the PIE scan diagram for the mass 78 signal in a fuel-rich cyclohexane flame ($\Phi = 2$). It shows that the signal ionization energy threshold for the respective signal is about 9.24 eV. The NIST Webbook (webbook.nist.gov) gives the ionization energy of benzene (mass 78) as 9.24378 ± 0.00007 eV. Hence, this mass 78 species was identified as benzene. The PIE scans were also compared to the available photoionization cross section data for the probable species. The similarity in shape often indicates the presence of that particular species. This insight will be discussed in detail in Chapter 3 where the data analysis will be covered.

Isomers (different compounds having the same molecular weight) are common in hydrocarbon flames. However, each isomer may appear at a detectably different ionization energy, allowing. If an isomer at a higher energy has a weaker signal, determination of its appearance potential (onset) and thus identification become ambiguous. However, applying a linear extrapolation from the point of deviation can often allow the ionization potential of the higher-I.E. isomer to be detected.

2.3.1.2 Burner scan

Mole fraction profiles of the identified species are achieved through burner scans. In order to obtain the mole fraction profile along the axis perpendicular to the burner, the burner is moved towards the quartz cone and brought to the origin (the closest point the burner can reach towards the quartz cone tip). The origin is typically set at 1.02 mm away from the quartz cone tip for the ALS equipment. This is a safety measure so that the burner does not hit the cone.

A photon energy is chosen that is higher than the ionization energy (IE) of the species whose profiles are intended but lower than the IE of any isomer of the target species that may be present in the flame. The burner is moved stepwise slowly away from the sampling probe. Samples are collected at different steps along this axis, and the data is interpreted using a LabVIEW code. The signals thus obtained can then be transformed to mole fraction profiles as discussed later. The 10-eV burner scan profile at mass 78 in the fuel-rich cyclohexane flame is shown in Figure 2.5.

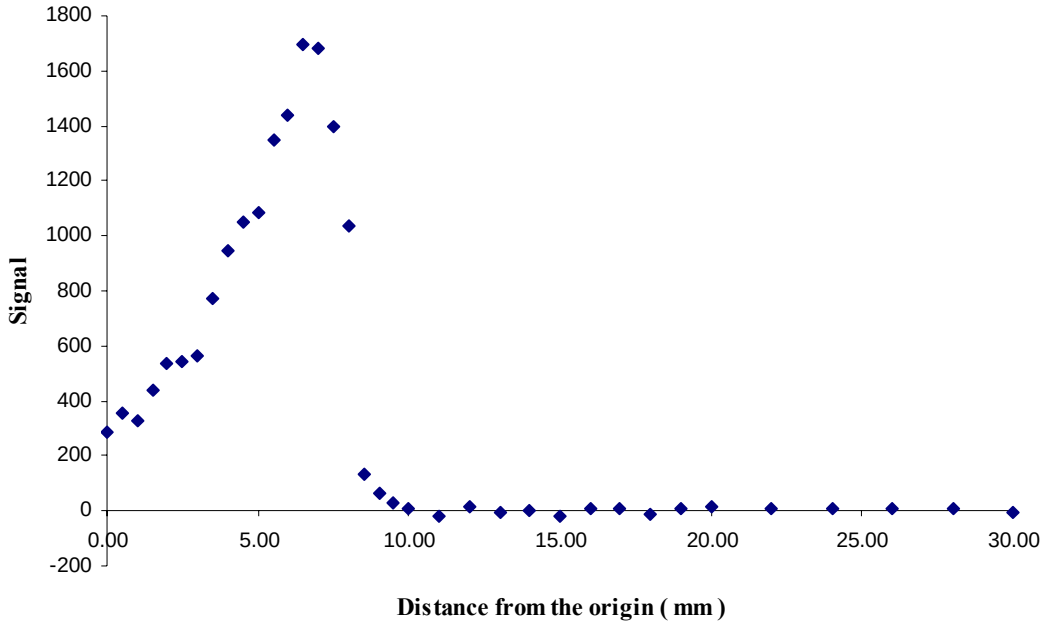

Figure 2.5. Burner-scan profile of mass 78 at 10 eV in the fuel-rich cyclohexane flame.

2.3.1.3 Energy calibration

The energy calibration factor is a correction for the photon energy, which is required to determine the actual ionization energy of a species. The photon energy is calibrated by doing an energy scan at a range of 12.0 to 13.2 eV, which is the autoionization region of molecular oxygen.

When an inner electron of an atom gets excited and the atom reaches superexcited state, it can undergo a radiationless transition from the discrete superexcited state over into the state of an ion plus an electron. This process is called autoionization (Marr, 1967).

The peaks that are observed at this energy range are compared with the literature values (Nicholson, 1963). The difference between the energies at which these peaks are observed are taken into account, and an average of the differences is made. This average gives the energy calibration factor. Figure 2.6 shows the typical autoionization peaks of O_2 as observed in the ALS.

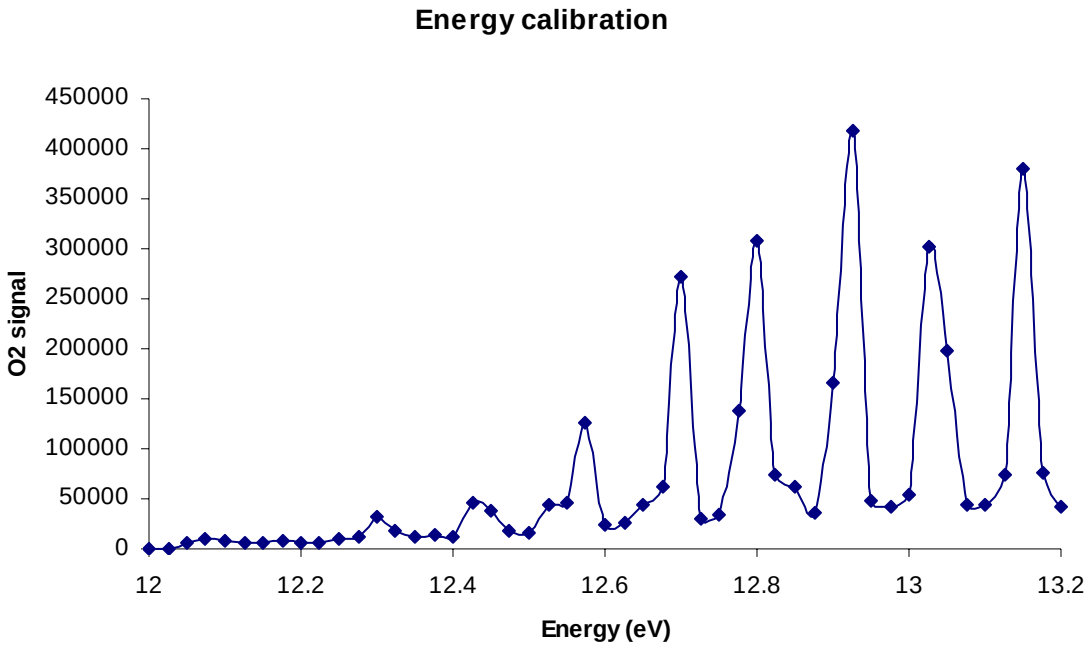

Figure 2.6. Typical autoionization-peak measurement of oxygen in ALS system.

2.3.2 Temperature measurement

The flame temperatures for a fuel-rich cyclohexane flame (Φ =2.0), two fuel-rich toluene flames (Φ = 2.03, and Φ = 3.95), and a lean methane flame (Φ = 0.451) were measured using a R-type (Platinum / Platinum 13% Rhodium) thermocouple. A detailed description of the measurement technique is presented here.

2.3.2.1 Basic principles of temperature measurement with a thermocouple

A thermocouple is a temperature sensor, which consists of two dissimilar metals joined together. When one junction of the thermocouple is held at a different temperature from the other, an electromotive force (voltage) is generated. Generally the reference temperature is selected as 0˚C. The voltage is a function of the temperature and can be read using an analog-to-digital converter or a voltmeter. The corresponding temperature can be inferred from standard tables available for the particular thermocouple materials.

For high-temperature applications. type R, S (Platinum/ Platinum 10% Rhodium), C (Tungsten 5% Rhenium/ Tungsten 26% Rhenium) and B (Platinum 30% Rhodium/ Platinum 6% Rhodium) type thermocouples are typically used.

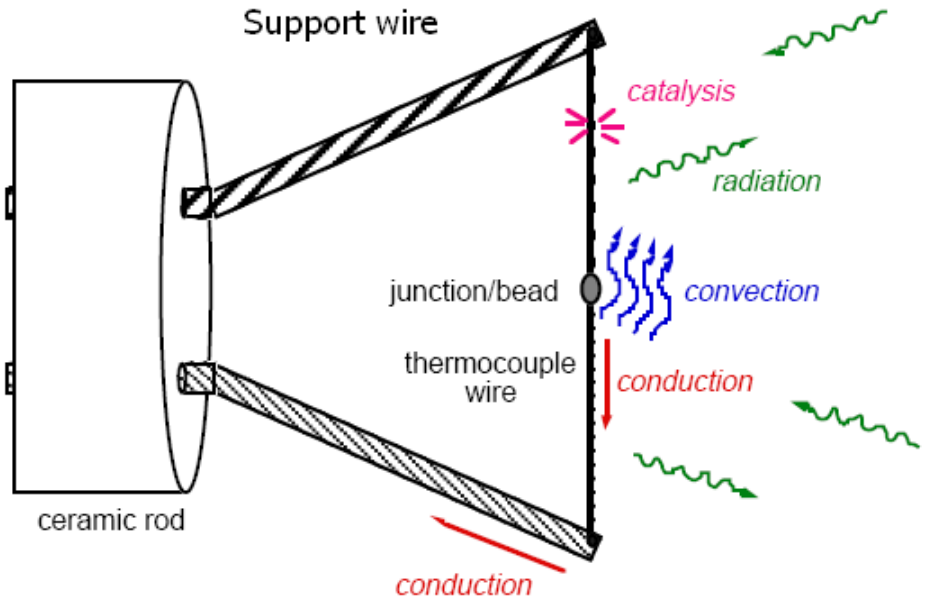

Figure 2.7. Heat transfer modes from thermocouple (Shaddix, 1999).

A schematic of typical laboratory thermocouple assembly is shown in Fig. 2.7. The major modes of heat transfer are indicated in the figure. A general energy balance

on the thermocouple is given in equation 2.2 (Shaddix, 1999). The left-side terms of the equation are heat transfer associated with surface-induced catalytic reactions, convection between the gases and the thermocouple, conduction along the thermocouple wires, and radiant heat transfer between the gases and the thermocouple and its surroundings respectively. The right-side term refers to the transient heating or cooling of the thermocouple.

$$\dot{Q}_{cat} + \dot{Q}_{conv} + \dot{Q}_{cond} + \dot{Q}_{rad} = \rho c_p V \frac{dT_{tc}}{dt} \tag{2.2}$$

As the catalytic and conductive heat transfer effects are hard to quantify, attempts are made to minimize these terms. A 4.5% BeO / Y_2O_3 coating was applied on the thermocouple to minimize potential catalytic reactions, which will be discussed in detail later. The diameter of the Pt and Pt 13% Rh wires were chosen as 0/003-in. (0.076 mm), and the length of the thermocouple wire was taken approximately as 4 cm. The length and the narrow diameter minimized the conductive heat transfer effect.

The radiation term can be expressed as the expression in equation 2.3

$$\dot{Q}_{rad} = \varepsilon_{tc}\sigma(T_{tc}^4 - T_w^4) \tag{2.3}$$

Combining Eqs. 2.2 and 2.3, we get

$$h(T_g - T_{tc}) = \varepsilon_{tc}\sigma(T_{tc}^4 - T_w^4) \tag{2.4}$$

T_{tc}, T_g and T_w refers to the thermocouple temperature, the gas temperature, and the chamber-wall temperature respectively. The emissivity, Stefan-Boltzmann constant, and heat transfer coefficient are denoted as ε_{tc}, σ and h respectively. Therefore the heat transfer coefficient and the emissivity for the thermocouple should be known to rectify

the radiation loss effect theoretically. This problem can be avoided by the electrical compensation technique, which will be discussed later.

2.3.2.2 Thermocouple construction

A schematic of the thermocouple probe is shown in Fig. 2.8. The support wires (one platinum and the other platinum 13% rhodium) were bigger in diameter than the thermocouple element (0.76 mm vs. 0.076 mm). The support wires were threaded through a ceramic support, which was then put inside a stainless-steel protection tube, which was in turn filled with Apiezon W100 wax. This sealing was necessary to prevent air leakage when the thermocouple was inserted into the reaction chamber. The protection tube was then capped at both ends.

The support wires were shaped as shown in Fig. 2.8. To ensure stability and toughness in the support wires, they were clamped together using a pair of ceramic washers, a nut and a bolt. Care was taken so that the support wires could not touch each other, as any short circuit would lead to error in the thermocouple voltage.

The thermocouple element was built by butt-welding a 2-cm-long platinum wire (Omega Engineering, SPPL-003) with a diameter of 0.076 and a platinum 13% rhodium wire (Omega Engineering, SP13RH) of the same size. Prior to welding, care was taken to align the two wires such that the ends of both wires precisely touched each other. One end of the platinum wire was held with an adjustable clip. One end of the platinum 13% rhodium wire was held onto a micromanipulator. The micromanipulator enabled full X-Y-Z movement of the platinum 13% rhodium wire. A binocular microscope (Reichert-Jung) was used to look at the two wire tips, while the micromanipulator was used to

align the platinum 13% rhodium wire properly against the stationary end of platinum wire held by the adjustable clip. After the alignment was finished, the tips of the two wires were welded using a micro torch (Smith Equipment, 23-1001B). A propane/oxygen flame was used to weld the wires.

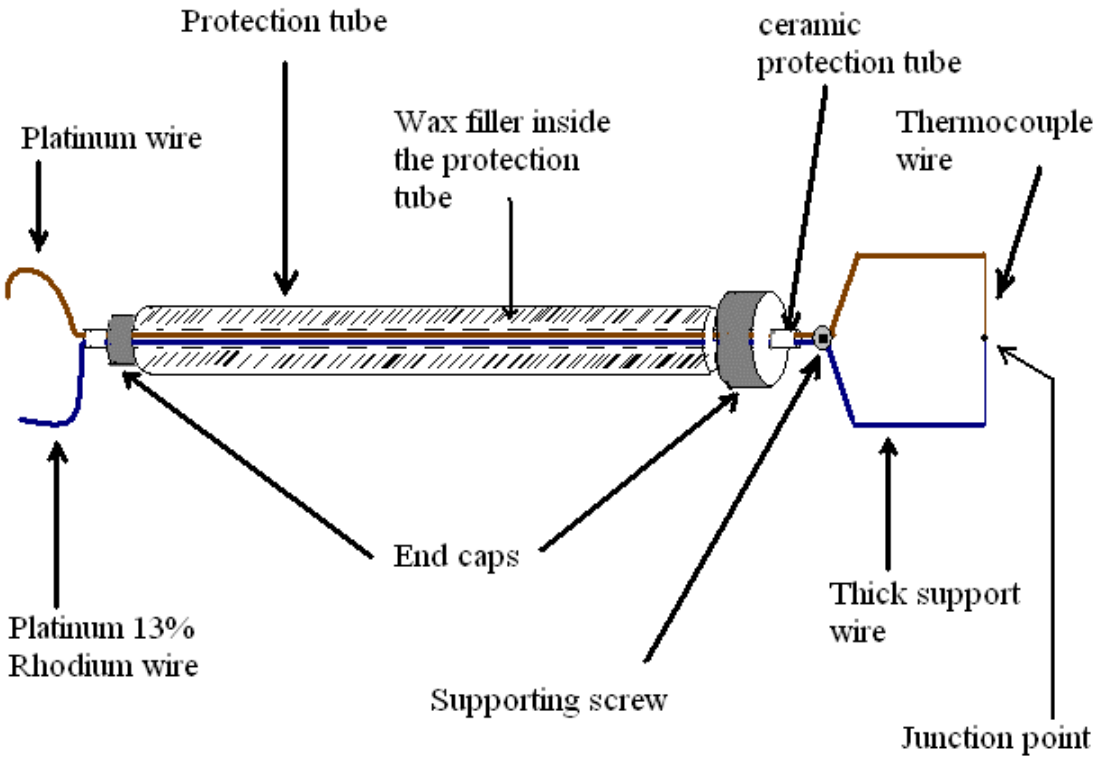

Figure 2.8. Schematic of the thermocouple probe.

Once the thermocouple element was built, it was welded to the thick support wire. Care was taken to weld the platinum end of the thermocouple element onto the platinum support wire.

2.3.2.3 Applying noncatalytic ceramic coating

The procedures followed by Bhargava (1997) and Law (2005) were followed to put the ceramic coating onto the thermocouple. After the thermocouple element was

welded onto the support wire, the element was cleaned by repeating a rinsing cycle of 1 N HCl, distilled water, and CH_2Cl_2. The thermocouple was immersed into the HCl, water, and CH_2Cl_2 for thirty seconds each. The procedure was repeated three times before applying the ceramic coating.

To prevent catalysis of radical recombination reactions on the bare thermocouple wire, a 4.5 wt% BeO-Y_2O_3 ceramic coating was applied to the wire by the procedure of Kent (1970). Pure ceramic powders were weighed first and then mixed well with a spatula. Then HCl was added in drops until the powder formed a milky solution. Ethylene glycol was added to the solution to get an enhanced wettability that would help the solution stick well onto the thermocouple element.

The thermocouple was coated with the ceramic solution by taking the solution onto a spatula and holding it close to the thermocouple so that the thermocouple was immersed into the ceramic solution pool. Then the spatula was moved along the thermocouple element so that all of the element could be coated with the ceramic coating.

The thermocouple was then inserted into the reaction chamber of the UMass system, and the chamber pressure was reduced to approximately 2 torr. Reduced pressure densified the coating, and then the coating was fired by resistively heating the thermocouple. The element was heated for 1 minute to 373 K (0.647 mV vs. an ice-point reference thermocouple) and then for 1 minute to 471 K (1.451 mV) to volatilize HCl and ethylene glycol, respectively. Then the element was heated over 5 minutes to 1715 K (16.633 mV) to sinter the ceramic. The coating was sintered at that temperature for 5 to 8 minutes. Temperature was then slowly reduced to 450 K (1.268 mV), where the Pt was annealed for 2 minutes. Finally, system pressure and the thermocouple temperature were

restored to ambient conditions. The procedure was repeated for ten times. The resulting coating was grayish white and opaque. To expose the coating to the highest temperature the sintering of ceramic might face, the thermocouple was coated four additional times with the ceramic coating and the firing process as mentioned was repeated with the addition of one last step. In the final step, after the thermocouple was heated to 1715 K for 5 to 8 minutes, it was further heated to 1923 K (19.540 mV) over a period of 5 minutes and sintered for 5 minutes. The thermocouple was then restored to initial temperature and pressure. The coating underwent a glass transition at that temperature and the final coating looked glassy and transparent.

A first-order test was performed to test the catalytic activity of the coating (Kent, 1970). The thermocouple probe was placed into the flame. The support and the element glowed red hot. The flame was extinguished by momentarily shutting off the fuel flow, and then the fuel flow was resumed. The support wire continued to glow due to catalytic oxidation on the bare wire; however, the element did not glow further. This observation suggested that the coating prevented catalytic activity of the thermocouple element.

2.3.2.4. Thermocouple circuit

The circuit that was used to measure the temperature and provide the resistive heating was the same as used by Law (2005). A JDR Instruments DFG-600 sweep function generator was used to create a 3 kHz AC current and was then amplified by a Radio Shack MPA-101 100 watt amplifier. A 1-kΩ variable potentiometer between the main potentiometer and the function generator was used to adjust the current flow through the thermocouple. A high-pass RC filter was placed by combining a 10-μF

capacitor on the amplifier output and an effective 8-Ω resistance, which removed any DC current from the circuit. An ammeter (Keithley 168 DMM) with 0-2 amp range was used to read the heating current, and a digital voltmeter was used to read the voltage produced by the thermocouple. Two low-pass filters placed in conjunction with the voltmeter filtered out the AC voltage. A reference thermocouple junction point was placed in ice water. A schematic of the circuit diagram is given in Figure 2.9.

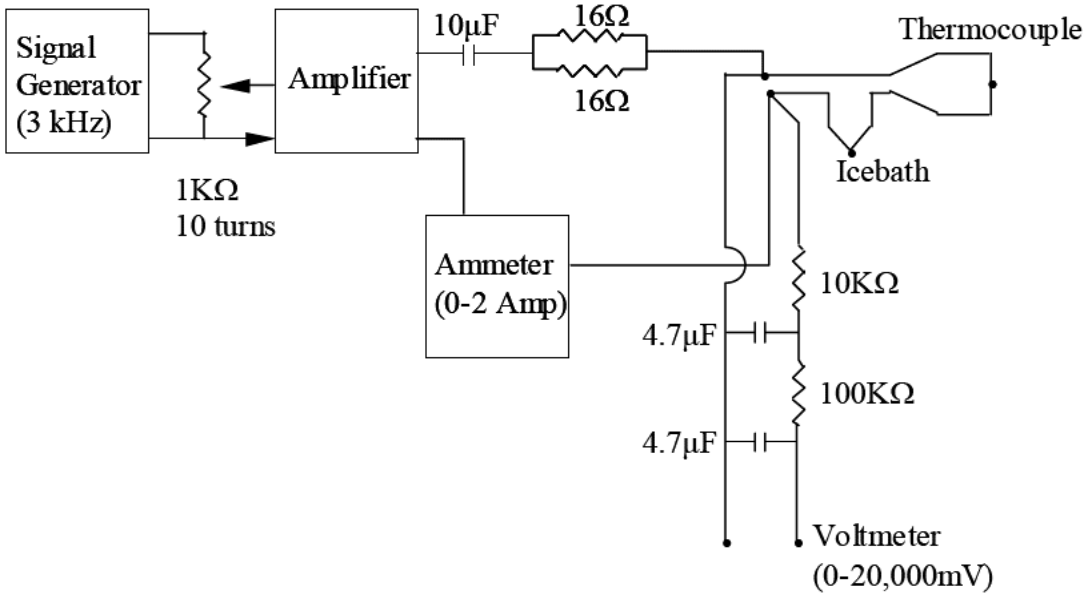

Figure 2.9. Schematic of thermocouple circuit (Law, 2005).

2.3.2.5 Resistive heating technique to eliminate radiation loss

A resistive heating technique used by Bittner (1981) was used here to compensate for the radiation loss. When the thermocouple is resistively heated, the energy balance equation described in Eq. 2.4 becomes

$$h(T_g - T_{tc}) - \varepsilon_{tc}\sigma(T_{tc}^4 - T_w^4) + \frac{4\rho_e I^2}{D\pi^2 d^2} = 0 \qquad (2.5)$$

where ρ_e , I, D, and d refer to electrical resistivity per unit length, heating current, thermocouple wire diameter, and coated-thermocouple diameter, respectively. At low pressures, the heat transfer coefficient can be neglected and the expression becomes.

$$\frac{4\rho_e I^2}{D\pi^2 d^2} - \varepsilon_{tc}\sigma(T_{tc}^4 - T_w^4) = 0 \qquad (2.6)$$

The thermocouple is calibrated at fairly low pressure to get the convection-free relationship of T_{tc} and I. To get the thermocouple in this low-pressure range, it was sealed in a vacuum chamber (a decommissioned turbopump housing), and the vacuum was applied in the range of 2 to 15 mTorr with a diffusion pump and a roughing pump in series (Duo Seal Model 1400, Welch). Current flowing through the thermocouple was varied and the voltage-current relationship was recorded from the voltmeter and the ammeter.

The voltage-current relationship was likewise measured for the thermocouple in the flame. When the voltage-current relationship measured in the flame intersects the calibration curve, the point of intersection gives the actual voltage that corresponds to the temperature corrected for the radiation loss. At that point T_{tc} becomes T_g, convective heat transfer is eliminated, and Eq. 2.5 becomes Eq. 2.6.

For the temperatures measured in the flames with the UMass equipment, care was taken not to exceed 20 mV to avoid melting the thermocouple.

The emissivity of the thermocouple changes as it is exposed to different flames (Shaddix, 1999). This change in emissivity is also reflected in the calibration curve for the thermocouple. Figure 2.10 shows the shift in the calibration curve for a post-flame thermocouple calibration of the fuel-lean methane flame and the preflame calibration for the fuel-rich cyclohexane flame. For this particular case, the thermocouple was used to

measure the methane flame temperature. Then a post-flame calibration was done on it. After that and prior to measuring the temperature for the cyclohexane flame, the thermocouple was put in the post-flame zone of the fuel-rich cyclohexane flame for an hour and then a preflame calibration was performed.

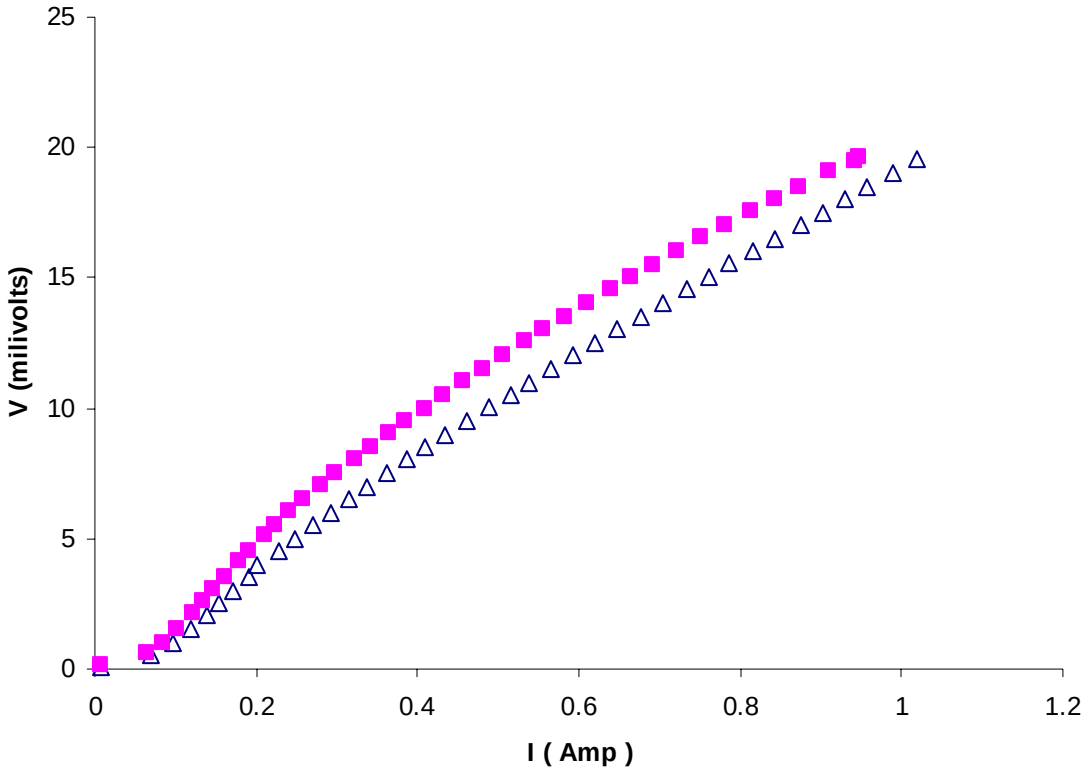

Figure 2.10. Calibration comparison of thermocouple wire exposed to different flames (■ refers to postflame calibration of methane flame, Δ refers to preflame calibration of cyclohexane flame).

At high temperatures, it would not be possible to get an intersection of the calibration curve and the measured data points. In that case, T_g could be calculated from

Eq. 2.4. The heat transfer coefficient can be calculated from the widely used Kramers (1946) correlation given in Eq. 2.7.

$$Nu_d = 0.42\,\mathrm{Pr}^{0.2} + 0.57\,\mathrm{Pr}^{1/3}\,\mathrm{Re}_d^{1/2} \qquad (2.7)$$

where the Nusselt number *Nu* refers to hd/k, the Prandtl number Pr refers to $\mu c_p/k$ and the Reynolds number *Re* refers to $dv\rho/\mu$. The gas velocity v can be computed from hot-wire anemometry experiments. The specific heat (c_p) of the gas mixture, viscosity (μ), thermal conductivity (k) and density (ρ) of the gas can be calculated at a film temperature $T_f = (T_g + T_{tc})/2$ using gas phase kinetics and transport codes developed at Sandia National Labs (Kee et al., 1986, 1987). Emissivity must be inferred from the radiation-compensated measurements made at lower temperatures.

2.3.2.6 Temperature measurement procedure

The thermocouple was calibrated prior to measuring the flame temperature. The thermocouple was placed inside the reaction chamber with the thermocouple element oriented parallel to the burner surface. Next, the burner distance from the thermocouple was calibrated using the LabView code developed by (Law, 2005). In order to do the calibration with respect to the burner, a 13-mm machinist's block was placed on top of the burner and the burner was moved toward the thick support wire of the thermocouple. When the block barely touched the lower side of the thick wire support, the distance was set in the LabView code. Thereafter, the burner can be moved by specified step sizes with respect to the thick wire. After the calibration was done, the flame was lit. The thermocouple glowed red. At that point using a cathetometer, the positions were noted of the thermocouple junction and the lower end of the thick support wire (with which the

burner was calibrated against). The difference in the two positions was used to find the exact distance of the burner from the thermocouple junction. Thereafter the burner was taken away from the thermocouple and the heated and unheated voltages were noted.

Once the readings were taken at a particular point, the burner was moved towards the thermocouple and five minutes was allowed to get the flame stabilized. After that, another set of data points were taken and the burner was moved on to the next desired point. The position of the thermocouple junction point was observed using the cathetometer to account for sagging of the thermocouple. After the data were obtained at all the points, the flame was extinguished and the thermocouple was calibrated again in the low-pressure chamber. The preflame and post-flame calibrations were compared. If they were within a few percent of each other, the measurement was considered good.

2.3.2.7 Analysis of temperature measurement data

As mentioned earlier, the experimental data points did not intersect the calibration curve in the high-temperature region of the flame. Close to the burner surface where the temperature was sufficiently low, an intersection was observed. For other points where the intersection point would have been too hot, a polynomial fit of the data points that could be safely measured was obtained using Origin software. Then, extrapolating the calibration curve and the polynomial fit, the intersection point was achieved. The intersection gave the thermocouple voltage corresponding to the flame temperature. The heated and unheated voltages were converted to temperature using the ITS-90 thermocouple inverse polynomials for R-type thermocouples reported by Omega Engineering, Inc. (2000).

CHAPTER 3

EXPERIMENTAL DATA AND ANALYSIS

3.1 Procedure of acquiring mole-fraction profile from the MBMS experiment

The intensity of a required species is measured from its burner-scan profile as discussed in Chapter 2. The signal of a species can be presented as.

$$I_i(V) = m_i(M_i)\sigma_i(V)N_iN_pVol \tag{3.1}$$

where I_i is the species signal intensity at a given photon energy (V); m_i is the mass discrimination factor (takes into account the difference in translation velocity of a species from other species present at a particular point in the flame due to mass difference), which is a function of species molecular weight (M_i) only; $\sigma_i(V)$ is the photoionization cross section of the species (which is a function of photon energy, V) at same V; N_i is the molar concentration of species i; N_p is the concentration of photons; and Vol is the ionization volume (a function of the slit width). Now as mole fraction X_i is proportional to N_i , the ratio of mole fraction of species i to that of a reference species measured at the same slit width can be represented as

$$\frac{X_i}{X_r} = \left(\frac{m_r\sigma_r}{m_i\sigma_i}\right)\frac{I_i}{I_r} \tag{3.2}$$

When all the mole fraction ratios are obtained, the mole fraction of the reference species can be found by taking an overall mole-fraction balance of all the species for each distance from the burner.

$$\sum_i X_i = 1 \tag{3.3}$$

$$X_r = \frac{1}{1 + \sum_{i;i \neq r} \frac{X_i}{X_r}} \tag{3.4}$$

Hence, the mole fraction of species *i* can be obtained from the mole-fraction ratio of species *i* to that of reference species and the mole fraction of the reference species.

Sometimes the signal of a species needs to be extrapolated from a lower energy (V_1) to a higher energy (V_2) for separating different species of same mass number. If the species signal is I_1 at V_1 then the signal of that particular species at V_2 is given by

$$I_2(V_2) = \frac{\sigma_2(V_2)}{\sigma_1(V_1)} \times I_1(V_1) \tag{3.5}$$

A few corrections are required for the mole-fraction profile generation. First, the intensity signal for each species should be normalized by the photodiode signal because the photon flux and thus the photon concentration varies with time. Second, a sweep correction of the intensity signal should be incorporated; i.e. all the species whose mole fractions are compared should be adjusted to the same number of sweeps because I_i is proportional to the number of sweeps. Third, the signal should be corrected for the isotopic contribution of ^{13}C. Generally for each ^{12}C atom present in a particular species, the relative natural abundance of ^{13}C would be approximately 1.1% (Brosi and Hankins,

1937). Fourth, if the reference species signal is taken at a different slit width, a volume correction factor should be incorporated to take into account the change in ionization volume of the reference species. Suppose I_1 and I_2 are signals for species i at two different slit widths w_1 and w_2 and at two voltages V_1 and V_2, respectively and the reference species signal is measured at slit width w_2 and at voltage V_2.

$$I_1(V_1) = m_i(M_i)\sigma_1(V_1)N_i N_p Vol_1 \tag{3.6}$$

$$I_2(V_2) = m_i(M_i)\sigma_2(V_2)N_i N_p Vol_2 \tag{3.7}$$

Now the correction factor with which the reference species should be multiplied is $C = Vol_1/Vol_2$ (Law, 2005), which is given by

$$\frac{Vol_1}{Vol_2} = \left(\frac{I_1 \times \sigma_2}{I_2 \times \sigma_1}\right) \tag{3.8}$$

3.2 Cyclohexane data analysis

The fuel-rich cyclohexane flame feed conditions are tabulated in Table 3.1.

Table 3.1 Condition for the fuel-rich cyclohexane flame.

	Flow Rates	Pressure in the Reaction Chamber	Fuel Equivalence Ratio (Φ)
Cyclohexane	1.133 ml/min (liquid, 25 ^{o}C)	30 Torr	2.003
Oxygen	1.058 SLM		
Argon	0.564 SLM		

The species identified in the fuel-rich cyclohexane flame are reported in Table 3.2. The description of the mole-fraction profiles of these species follows below. An energy scan from 8 to 10.7 eV was used to identify the species in the cyclohexane flame.

Table 3.2 List of species measured in the fuel-rich cyclohexane flame, ionization energies of the species as reported in the NIST Chemistry WebBook (NIST, 2005), ionization energy observed, and ionization energy used to measure the profile.

AMU	Species Identified	Ionization energy from literature (eV)	Ionization energy observed (eV)	Burner scan Energy (eV)
2	H_2	15.42593±0.00005	-	16.2
15	Methyl (CH_3)radical	9.84±0.01	9.765	10.00
16	Methane (CH_4)	12.61±0.01	-	13.20
18	Water (H_2O)	12.621 ±0.002	-	13.20
26	Acetylene (C_2H_2)	11.4±0.002	-	12.30
27	Vinyl (C_2H_3) radical	8.25	8.37	12.30
28	Ethylene (C_2H_4)	10.5138±0.0006	10.469	12.30
29	Formyl (HCO) radical	8.12±0.04	8.365	10.00
30	Formaldehyde	10.88±0.01	-	11.50
39	Propargyl (C_3H_3) radical	8.67±0.02	8.697	10.00
40	Allene (C_3H_4)	9.692±0.004	9.769	10.00
40	Propyne (C_3H_4)	10.36±0.01	10.319	10.50
41	Allyl radical(C_3H_5)	8.18±0.07	8.119	10.00
42	Ketene (C_2H_2O)	9.617±0.003	9.602	
42	Propene (C_3H_6)	9.73±0.01	9.719	10.00
44	Carbon dioxide (CO_2)	13.797±0.001	-	14.35
50	1-3 Butadiyne (C_4H_2)	10.17	10.119	10.50
52	1-Buten-3-yne (C_4H_4)	9.58±0.02	9.515	10.50
54	1,3-Butadiene (C_4H_6)	9.072±0.007	9.069	10.00
55	1-Buten-3-yl (C_4H_7) radical	7.49±0.02	Below 7.5	10.00
56	2-Butene (C_4H_8) and its stereoisomers (E and Z)	9.13	8.915	-
56	1-Butene (C_4H_8)	9.55±0.06	9.565	10.00
64	1,3-Pentadiyne (C_5H_4)	9.5 ± 0.02	9.465	10.00
65	Cyclopentadienyl (C_5H_5) radical	8.41	8.415	10.00
66	1,3-Cyclopentadiene (C_5H_6)	8.57 ± 0.01	8.515	10.00
67	Cyclopentenyl (C_5H_7) radical	7	Below 8	
68	1,3-Pentadiene (C_5H_8)	8.6	8.615	10.00

AMU	Species Identified	Ionization energy from literature (eV)	Ionization energy observed (eV)	Burner scan Energy (eV)
70	2-Pentene (C_5H_{10}) stereoisomers (Z and E)	9.01±0.03 9.04±0.01	9.015	10.00
74	1,3,5-Hexatriyne (C_6H_2)	9.5±0.02	9.492	10.00
76	Benzyne (C_6H_4)	9.03±0.05	8.965	10.00
78	Fulvene (C_6H_6)	8.36	8.365	10.00
78	Benzene (C_6H_6)	9.24378±0.00007	9.215	10.00
80	1,3-Cyclohexadiene (C_6H_8)	8.25	8.215	10.00
82	Cyclohexene (C_6H_{10})	8.95±0.01	8.915	10.00
83	Cyclohexyl (C_6H_{11}) radical	7.66±0.05	Below 8	10.00
84	Cyclohexane (C_6H_{12})	9.88±0.03	9.915	10.00
92	Toluene (C_7H_8)	8.828±0.001	8.815	10.00
92	5-Methylene-1,3-Cyclohexadiene (C_7H_8)	8.1	8.115	10.00
94	Phenol (C_6H_6O)	8.49±0.02	8.515	10.00
98	Cyclohexanone ($C_6H_{10}O$)	9.16±0.02	9.165	10.00
102	Phenylacetylene (C_8H_6)	8.82±0.02	8.79	10.00
104	Styrene (C_8H_8)	8.464±0.001	8.465	10.00
106	Para-xylene (C_8H_{10})	8.44±0.05	8.365	10.00
116	Indene (C_9H_8)	8.14±0.01	8.115	10.00
128	Naphthalene ($C_{10}H_8$)	8.144±0.001	8.117	10.00

3.2.1 Mole-fraction profiles

The mole-fraction profiles of the species identified follow in an ascending mass number order. The photoionization cross-sections and mass discrimination factors used are given in Appendix A.

Mass 2. The mass 2 species was not detected in the energy scan range of 8 to 10.7 eV. The species showed up at 16.2 eV burner scan. It was identified as hydrogen molecule. The hydrogen mole-fraction profile is depicted in Figure 3.2. It shows a linear increase in hydrogen mole fraction away from the burner (up to about 10 mm) and then

the mole fraction increases very gradually towards the end of the post flame zone. At the post-flame zone, the mole fraction reaches 8.17 % of the post-flame gases.

Mass 15. The mass 15 species was identified as methyl (CH_3) radical, based on its mass and threshold ionization energy reported in Table 3.1. The mole-fraction profile was reported in figure 3.3. It shows a peak in methyl radical mole fraction at 9.02 mm from the burner, and then it decreased away from the burner.

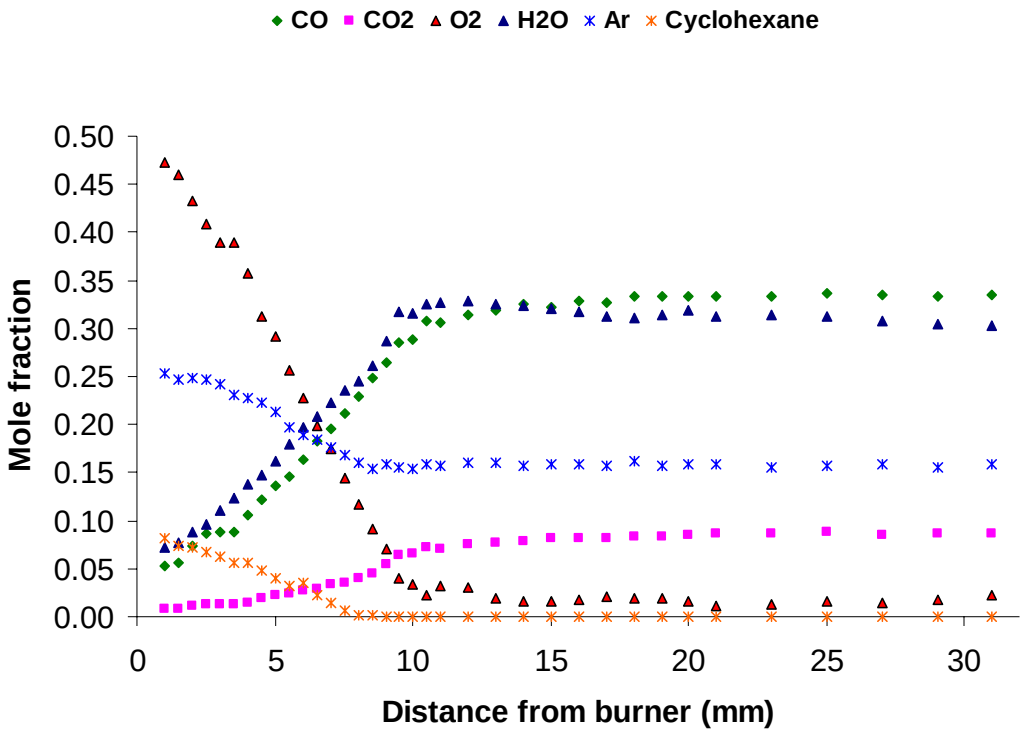

Figure 3.1. Mole-fraction profile of major species cyclohexane, CO, CO_2, O_2, H_2O, Ar.

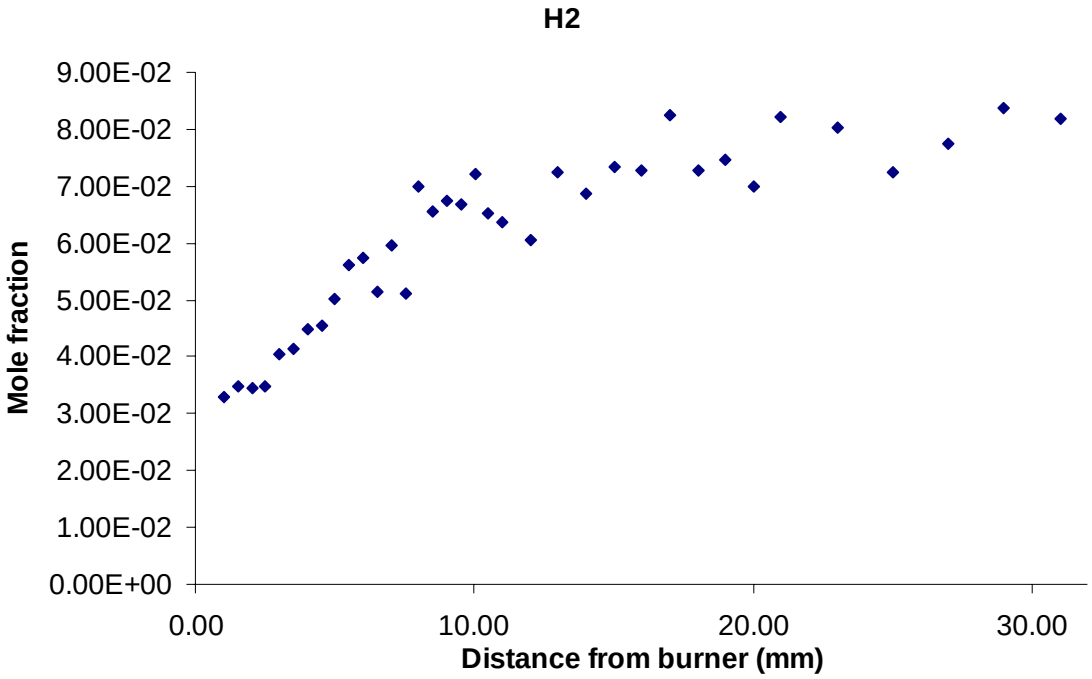

Figure 3.2. Mole-fraction profile of hydrogen.

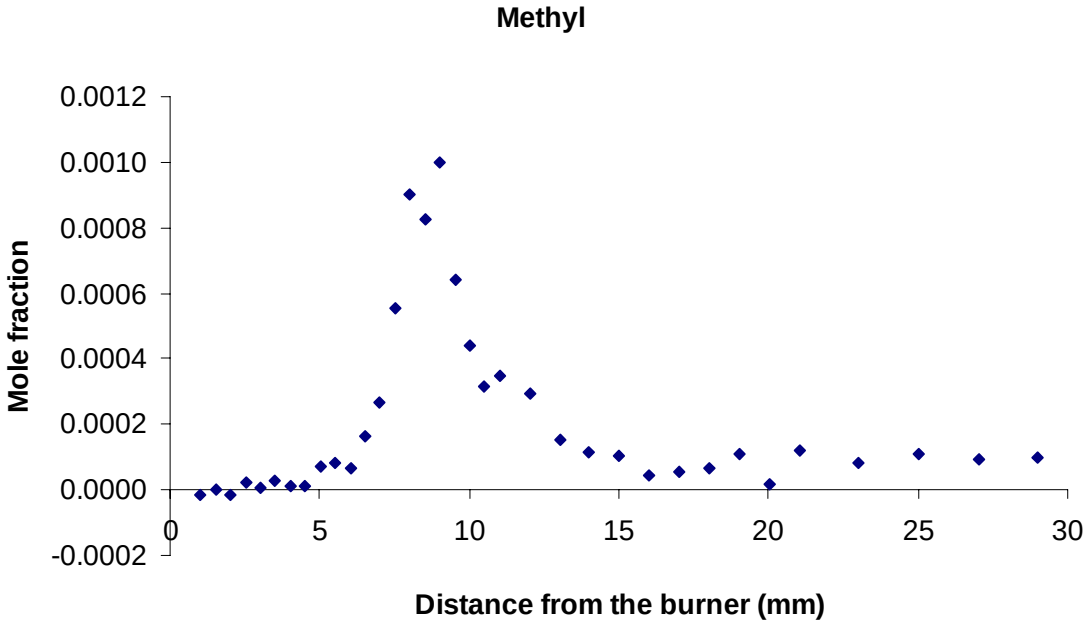

Figure 3.3. Mole-fraction profile of methyl radical.

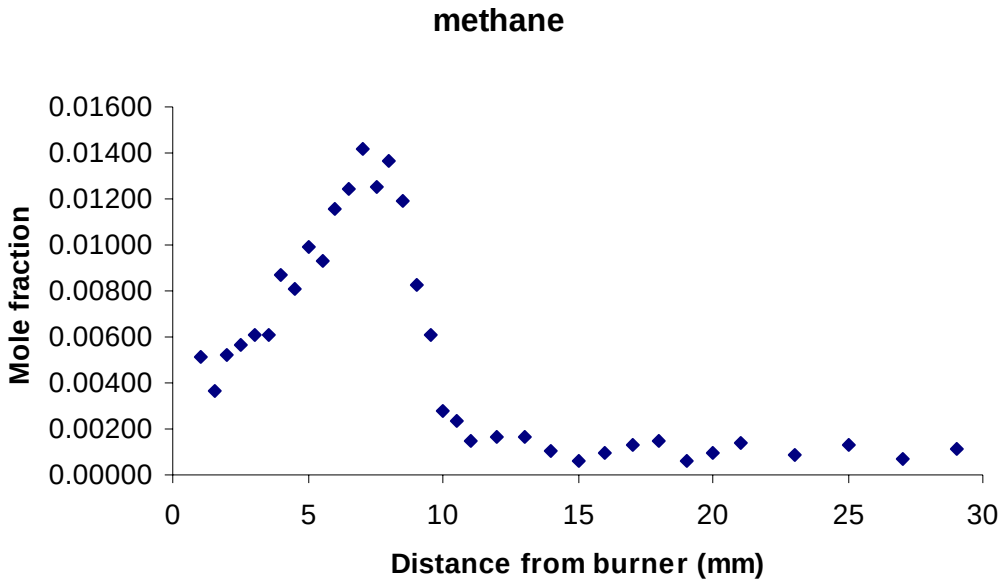

Figure 3.4. Mole-fraction profile of methane.

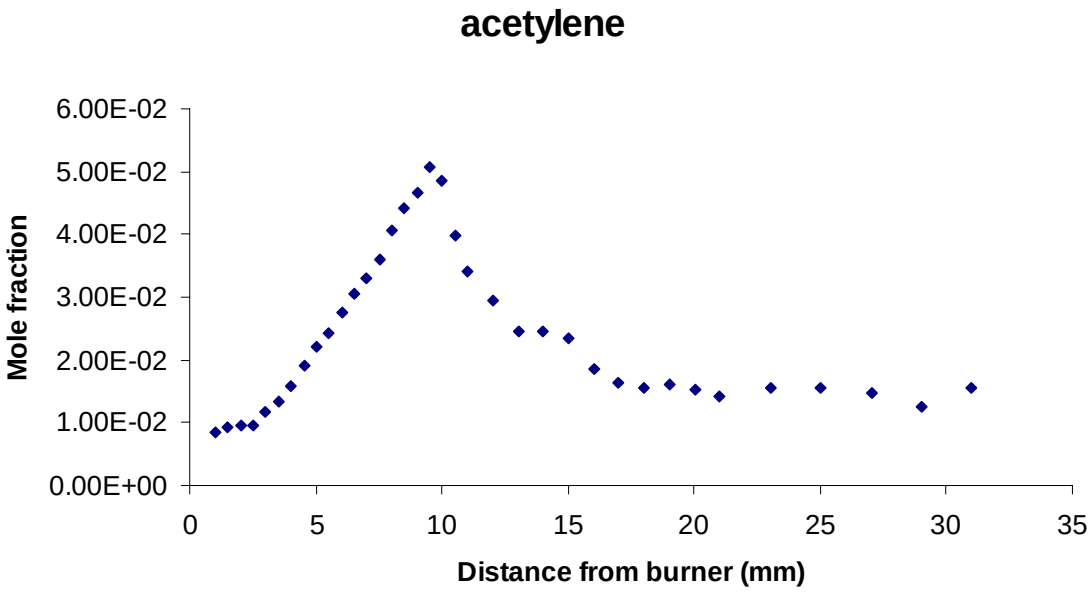

Figure 3.5. Mole-fraction profile of acetylene.

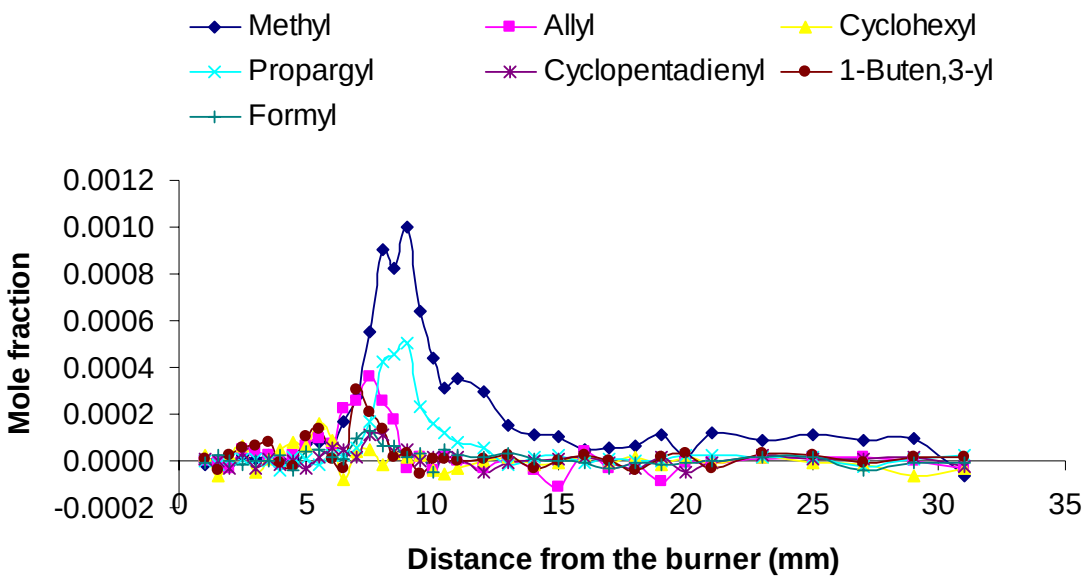

Figure 3.6. Mole-fraction profile of major radicals. methyl, propargyl, formyl, allyl, cyclopentadienyl, cyclohexyl, 1-Buten-3-yl.

C2H4

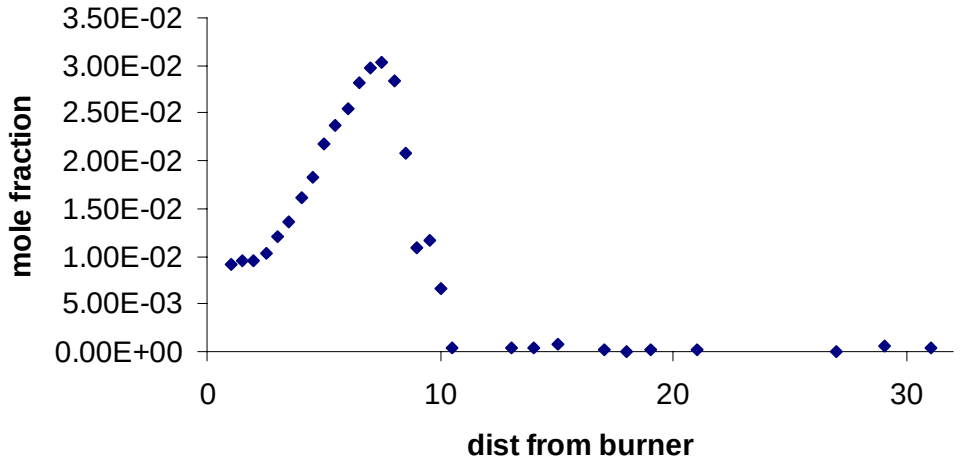

Figure 3.7. Mole-fraction profile of ethylene.

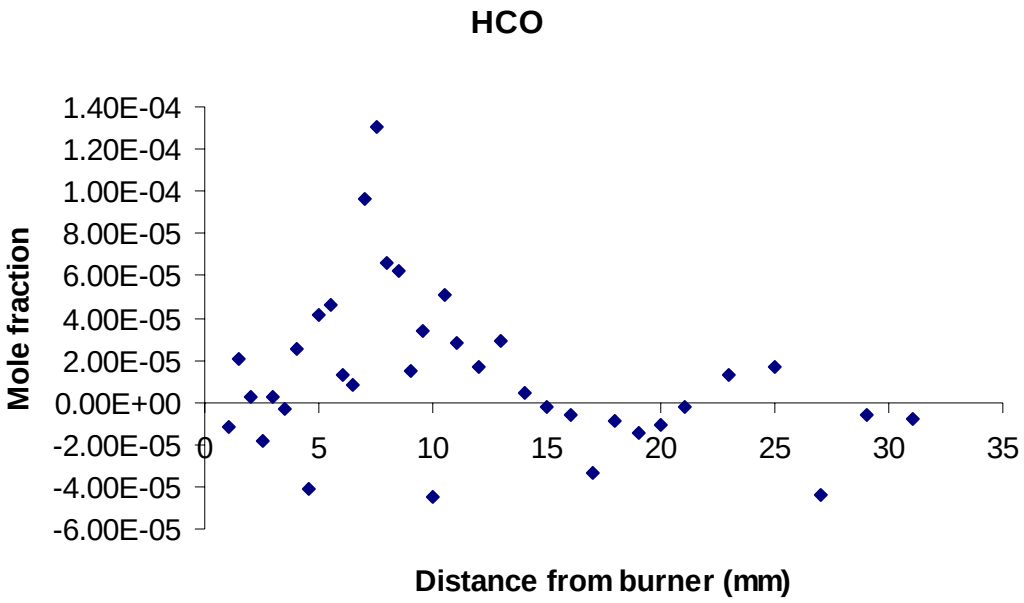

Figure 3.8. Mole-fraction profile of HCO.

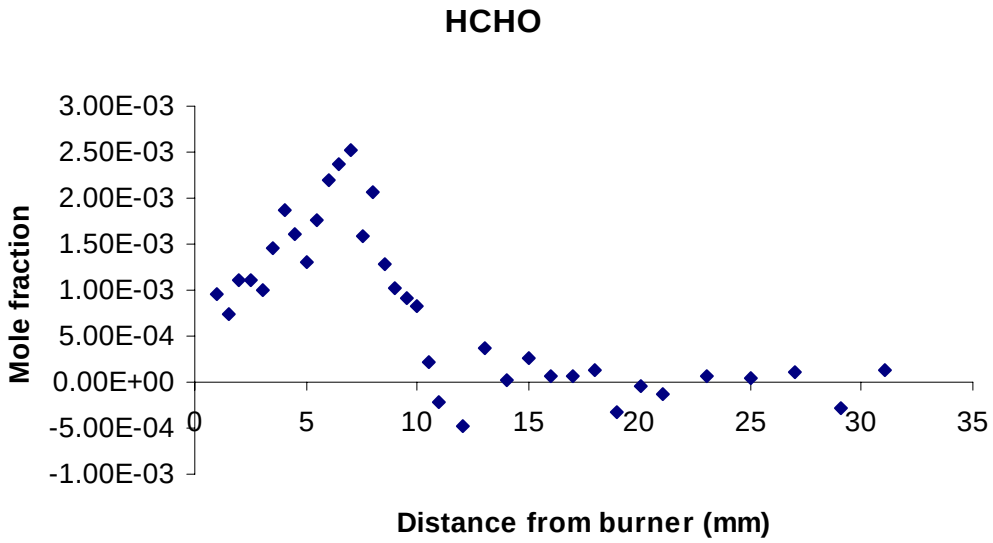

Figure 3.9. Mole-fraction profile of HCHO.

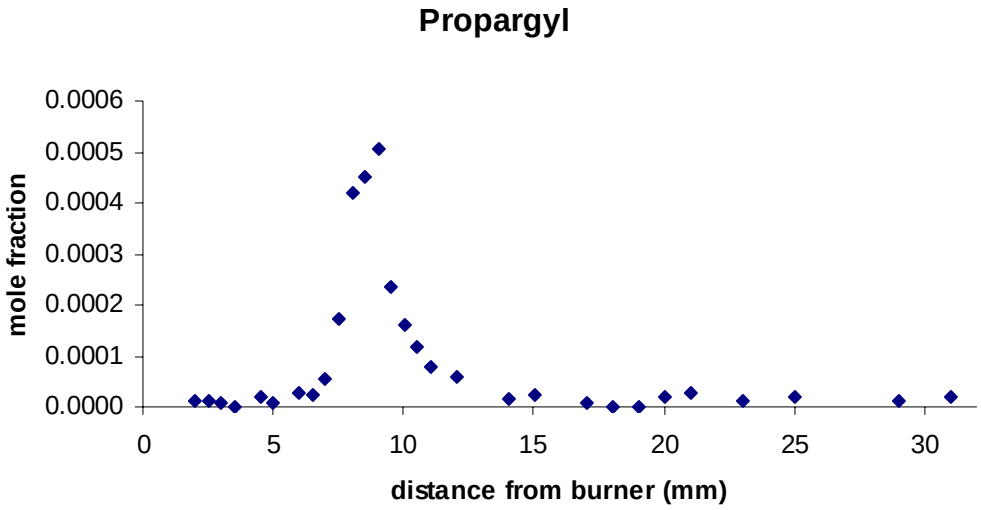

Figure 3.10. Mole-fraction profile of propargyl.

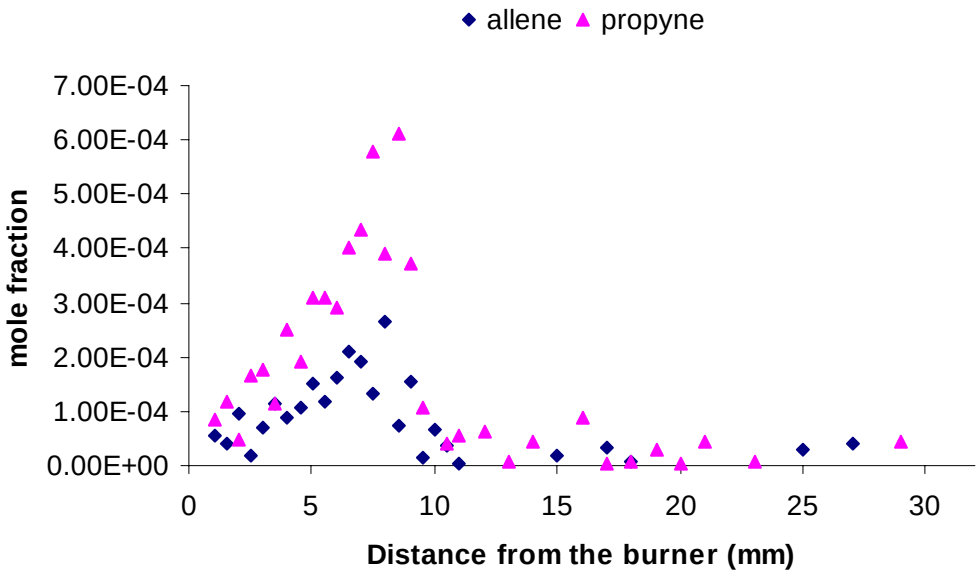

Figure 3.11. Mole-fraction profile of allene and propyne.

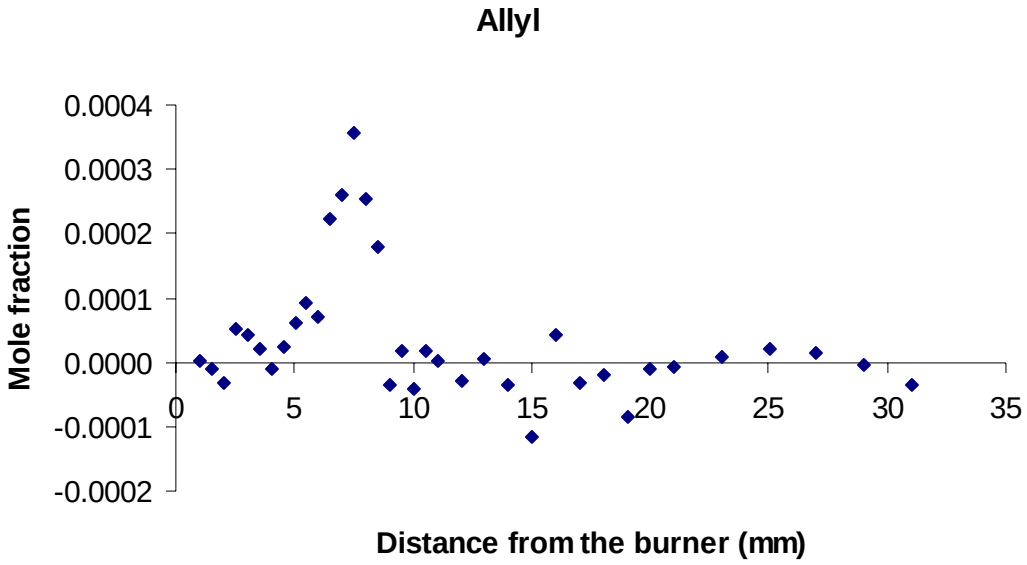

Figure 3.12. Mole-fraction profile of allyl.

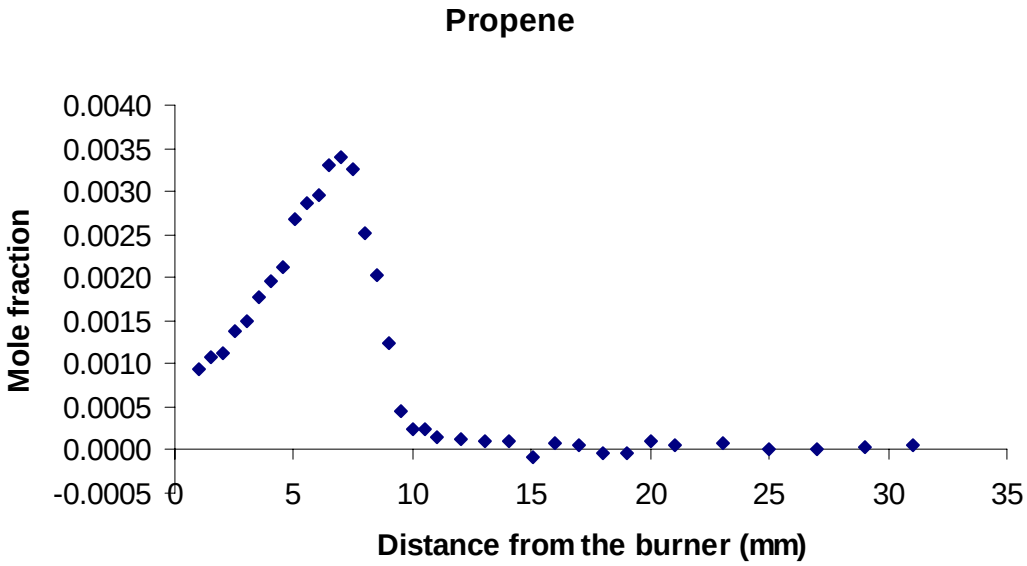

Figure 3.13. Mole-fraction profile of propene.

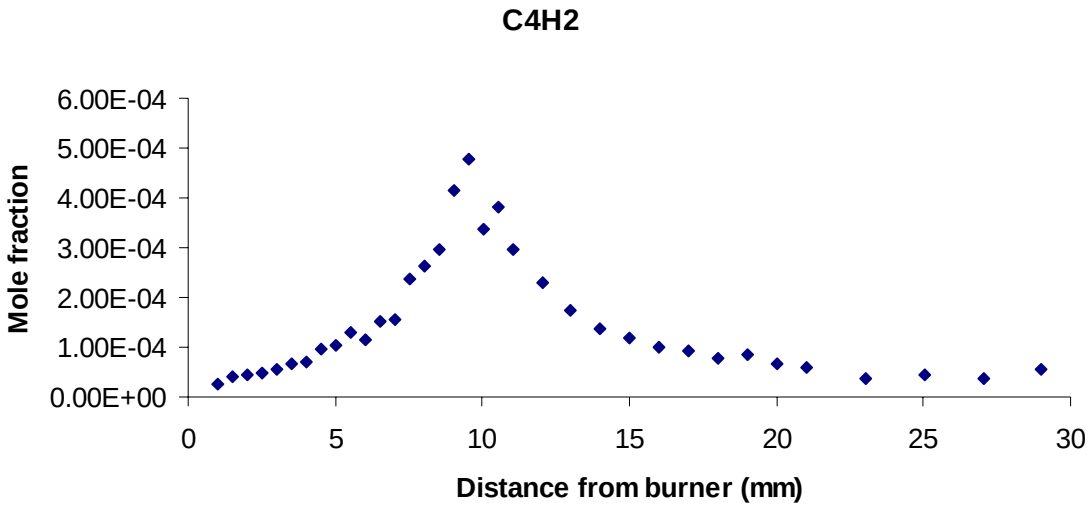

Figure 3.14. Mole-fraction profile of diacetylene (C_4H_2).

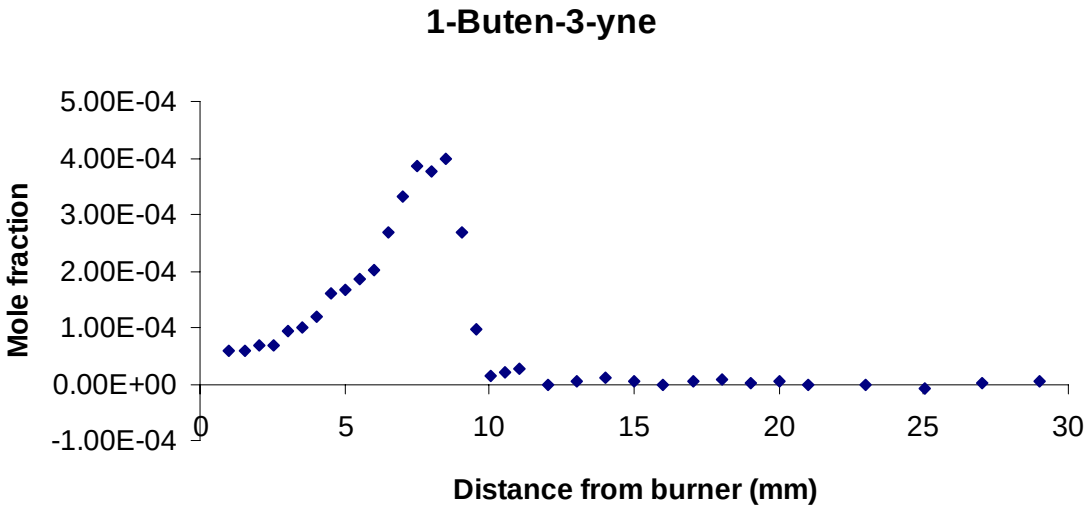

Figure 3.15. Mole-fraction profile of 1-buten-3-yne.

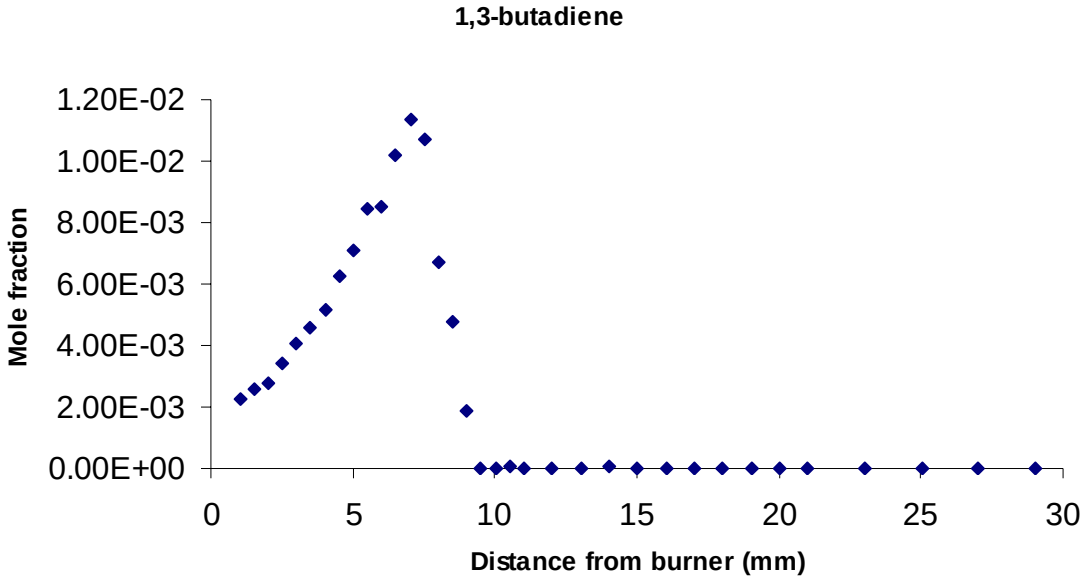

Figure 3.16. Mole-fraction profile of 1,3-butadiene.

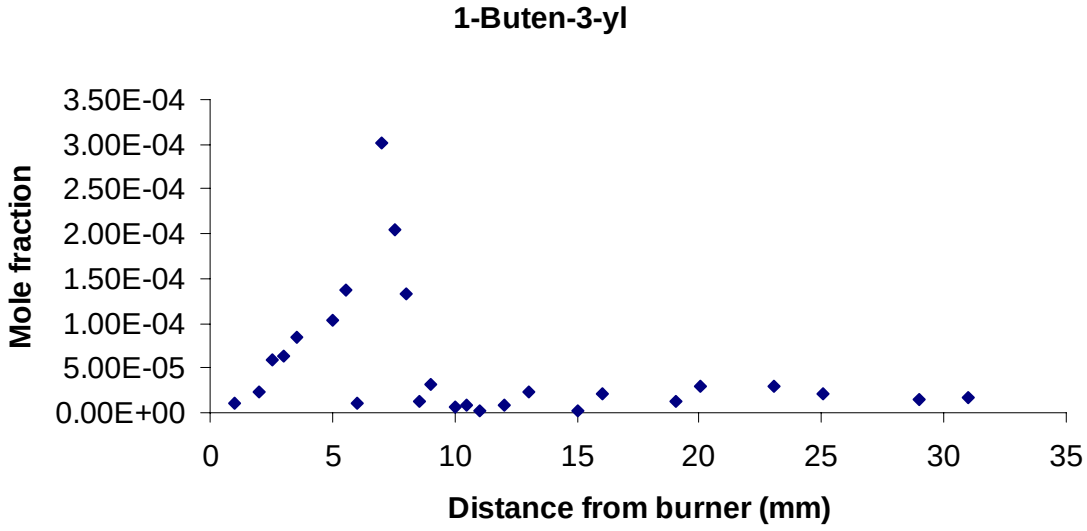

Figure 3.17. Mole-fraction profile of 1-Buten-3-yl radical.

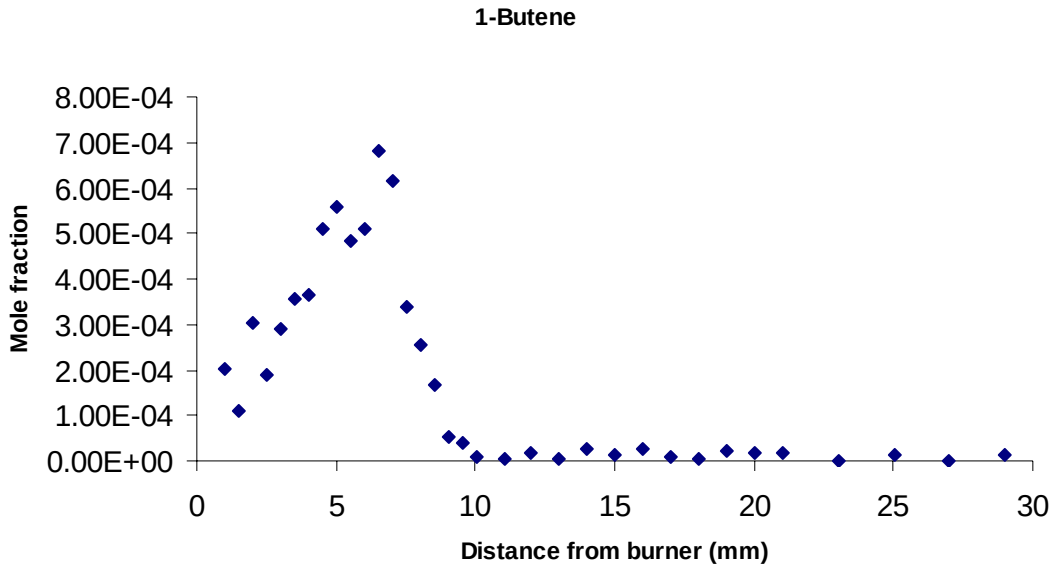

Figure 3.18. Mole-fraction profile of 1-Butene.

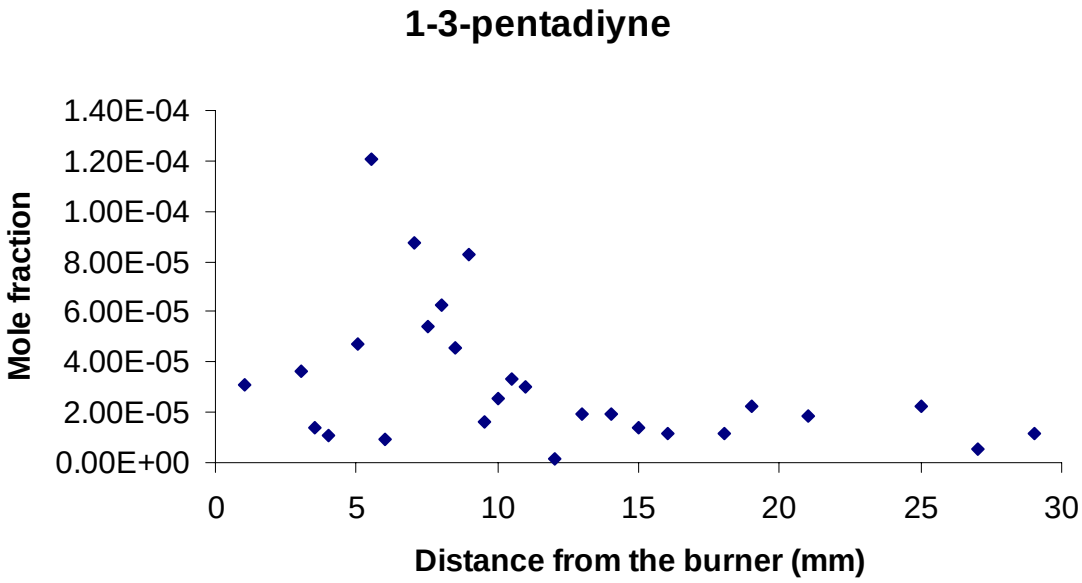

Figure 3.19. Mole-fraction profile of 1,3-pentadiyne.

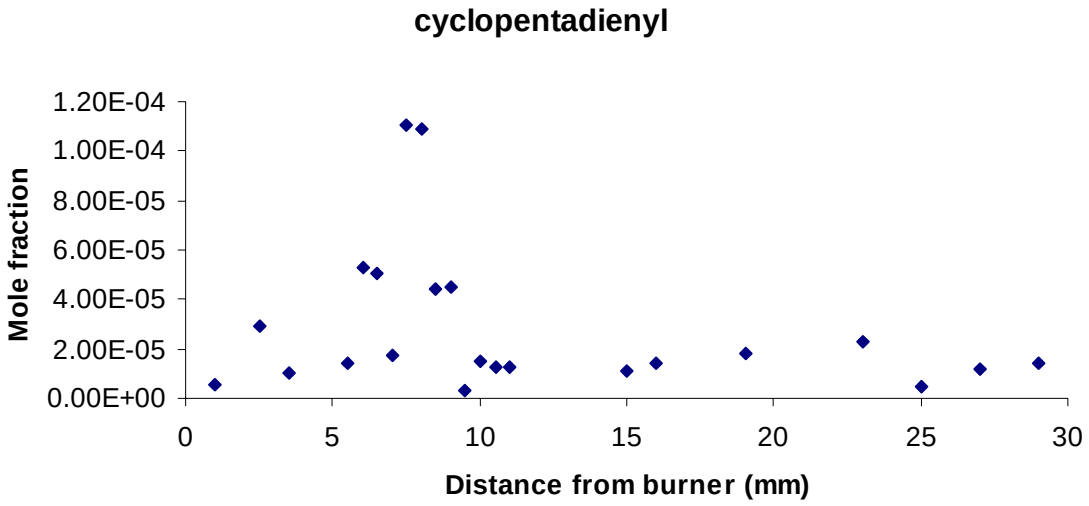

Figure 3.20. Mole-fraction profile of cyclopentadienyl radical.

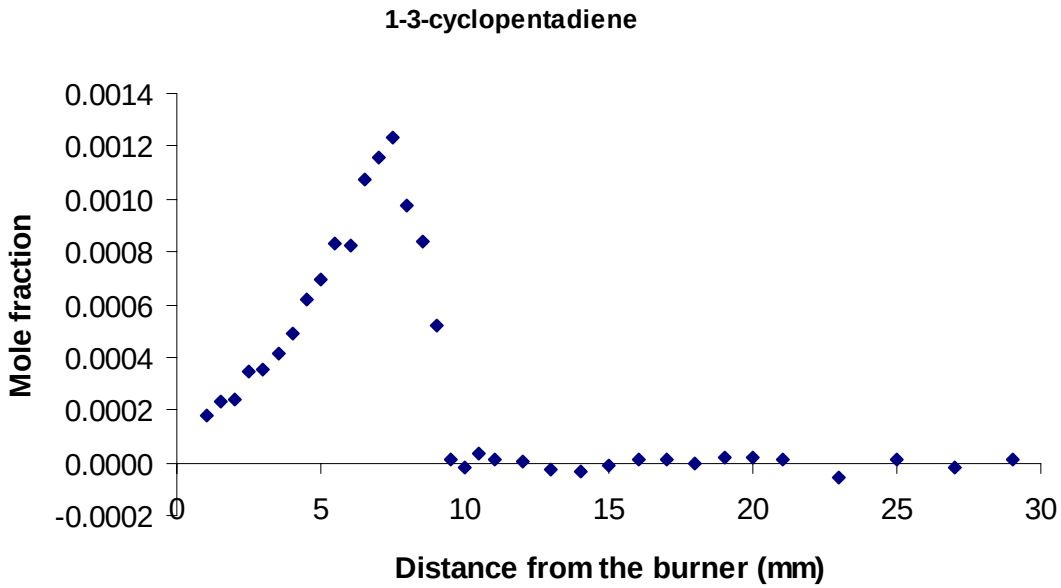

Figure 3.21. Mole-fraction profile of 1,3-cyclopentadiene.

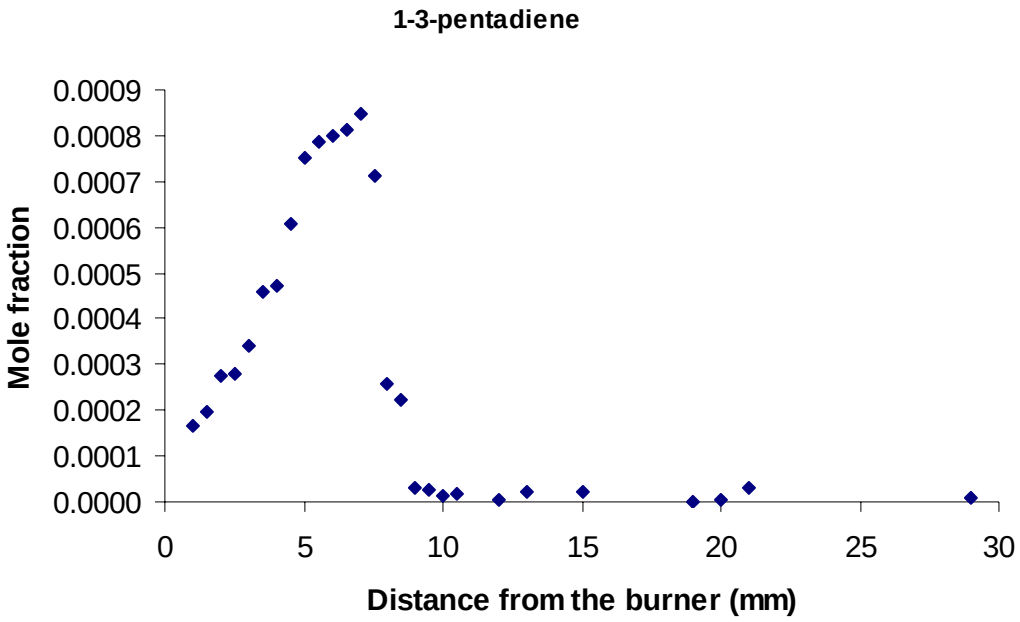

Figure 3.22 Mole-fraction profile of 1,3-pentadiene.

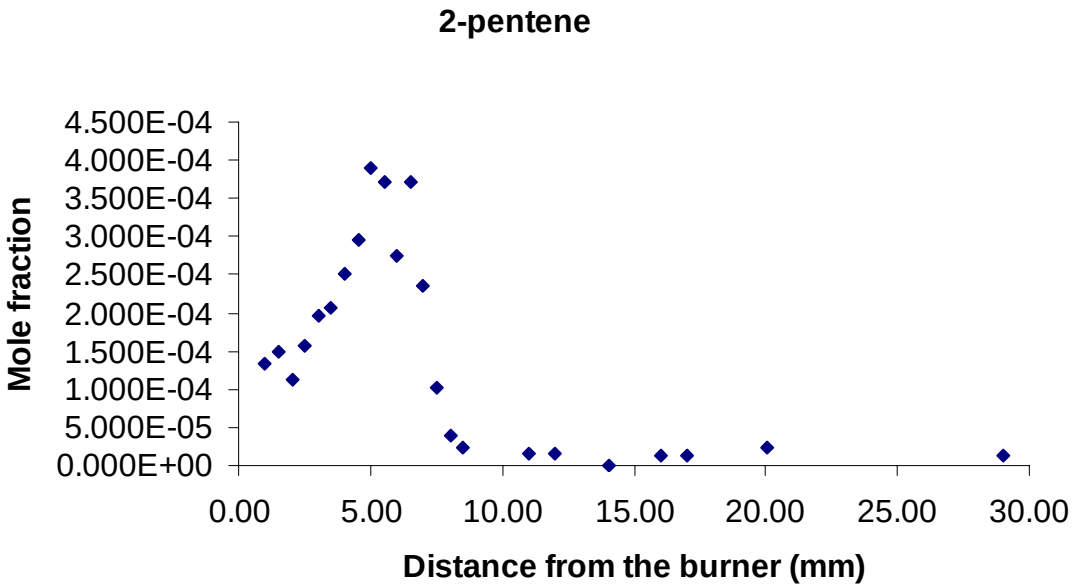

Figure 3.23. Mole-fraction profile of 2-pentene.

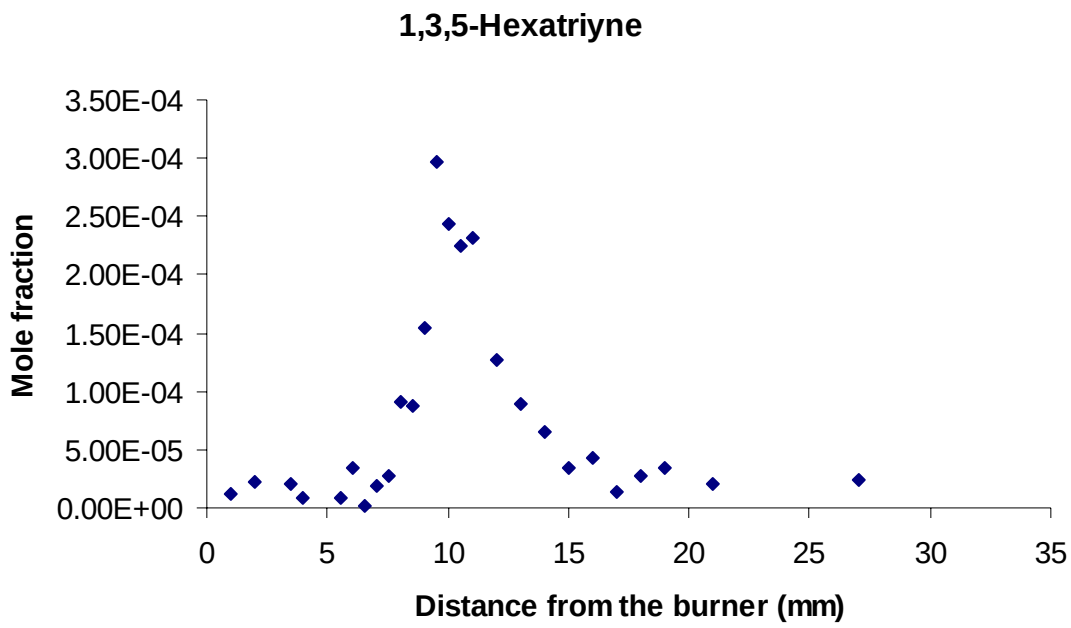

Figure 3.24. Mole-fraction profile of 1,3,5-hexatriyne (triacetylene).

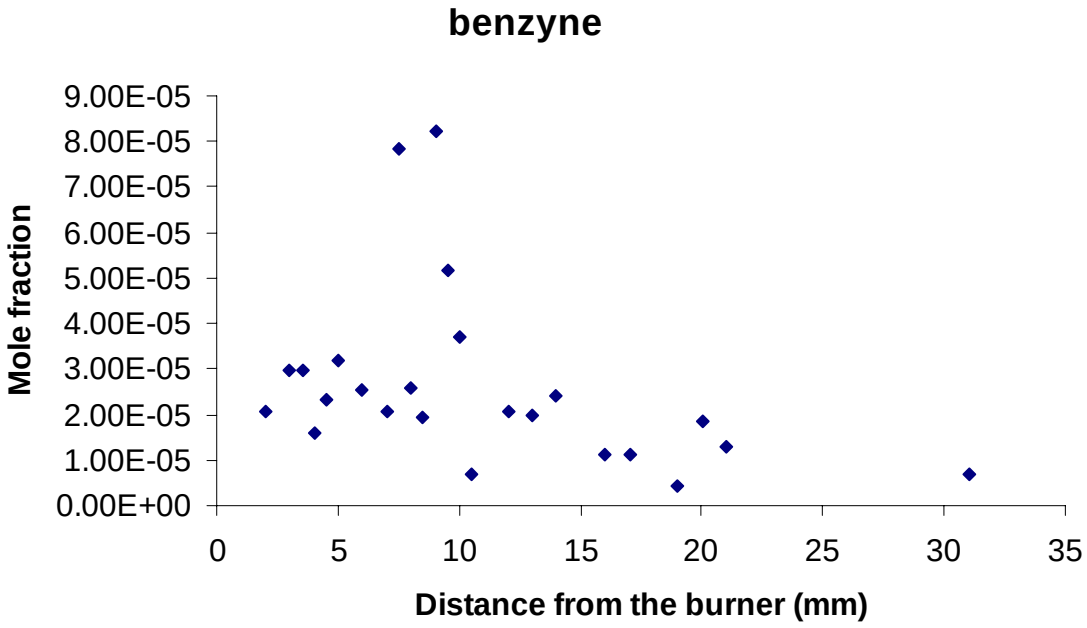

Figure 3.25. Mole-fraction profile of benzyne.

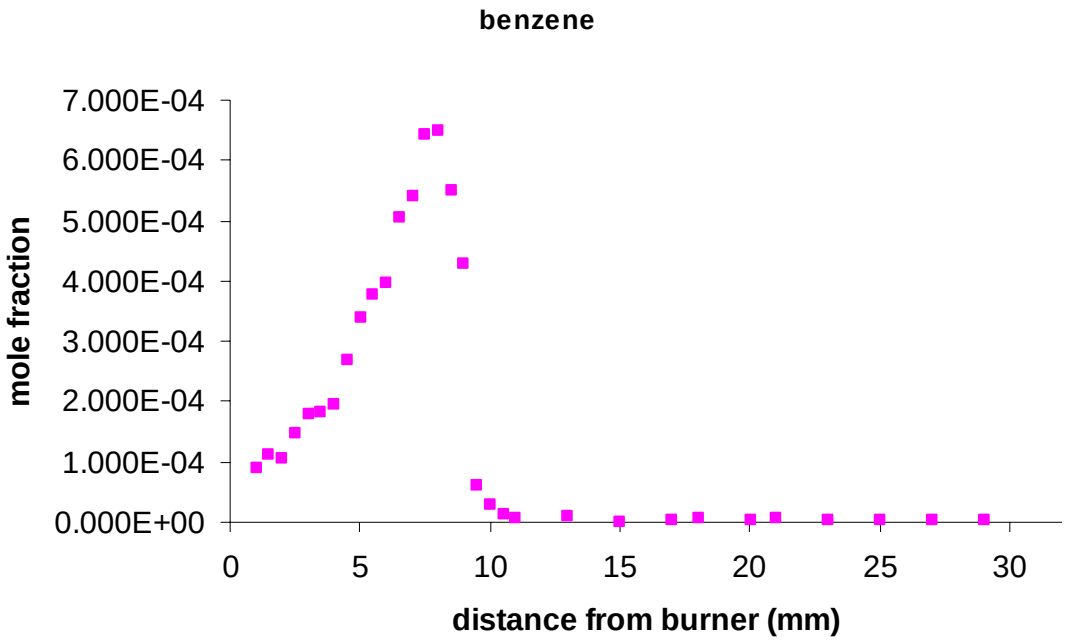

Figure 3.26. Mole-fraction profile of benzene.

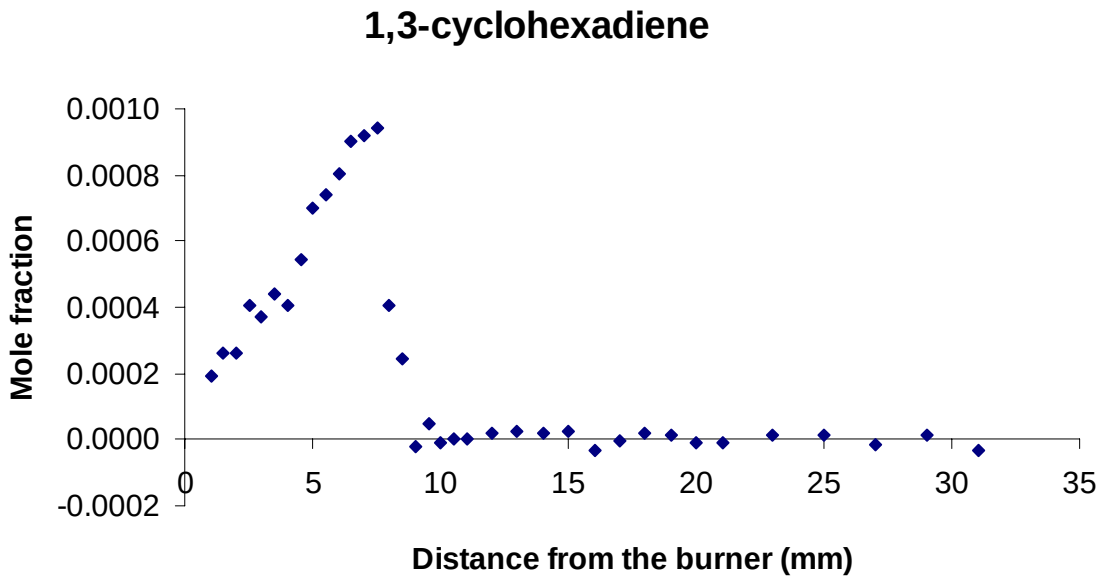

Figure 3.27. Mole-fraction profile of 1,3-cyclohexadiene.

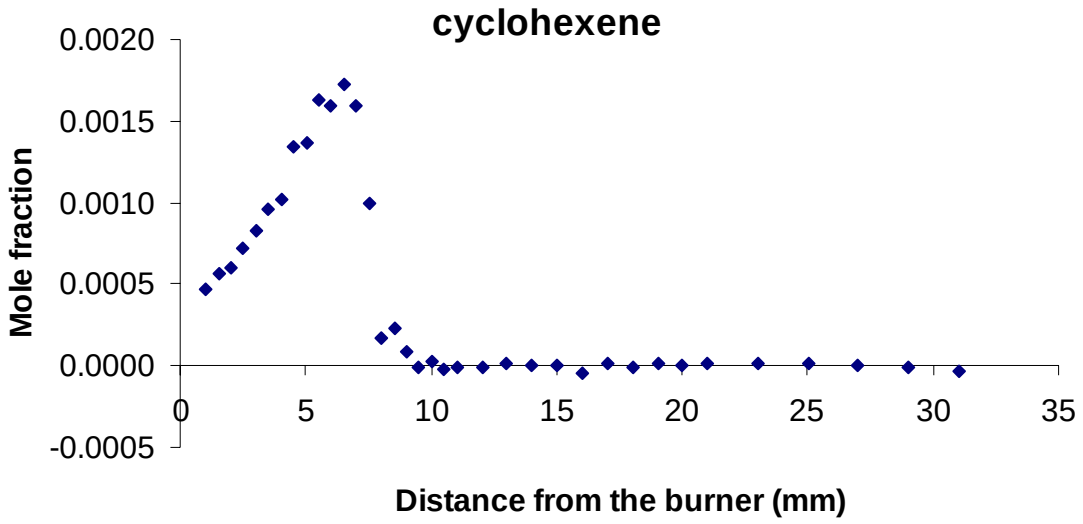

Figure 3.28. Mole-fraction profile of cyclohexene.

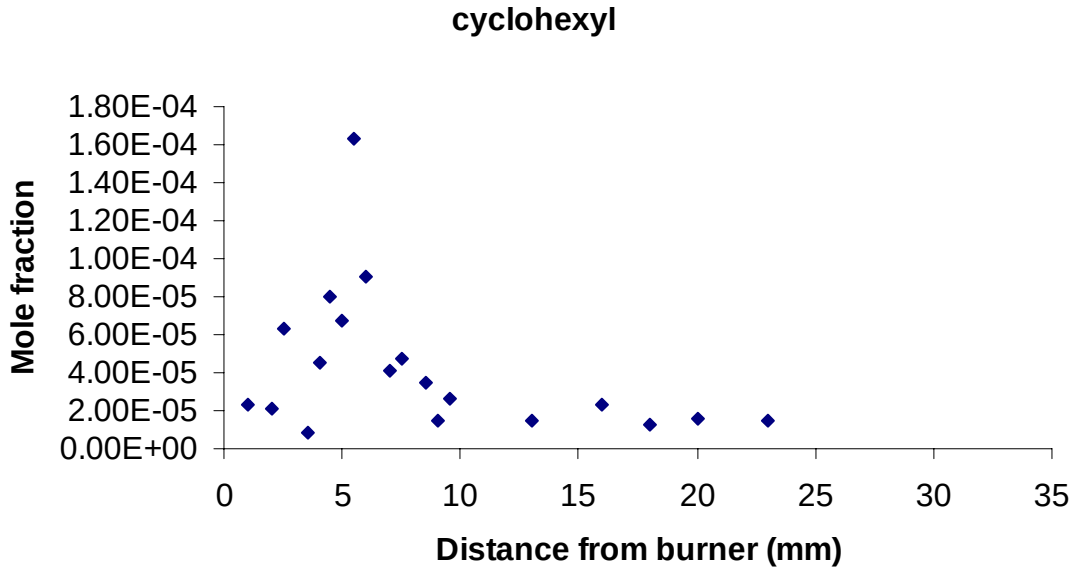

Figure 3.29. Mole-fraction profile of cyclohexyl radical.

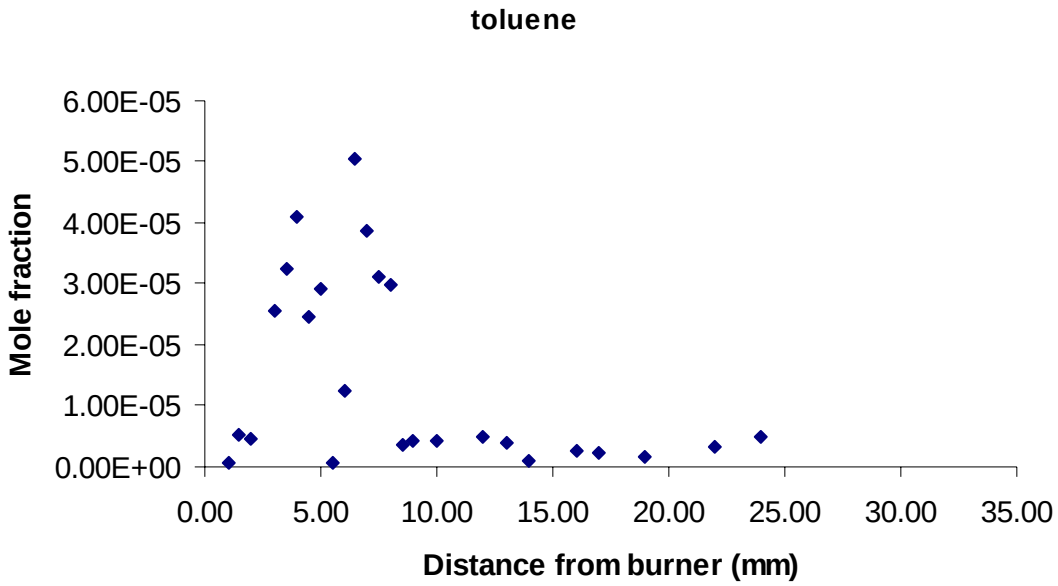

Figure 3.30. Mole-fraction profile of toluene.

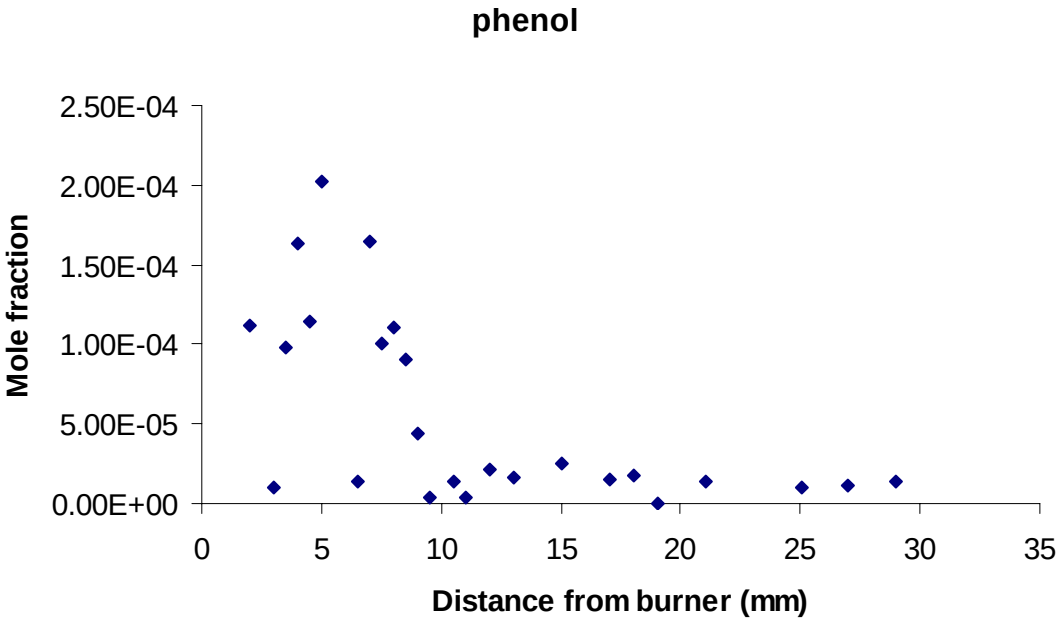

Figure 3.31. Mole-fraction profile of phenol.

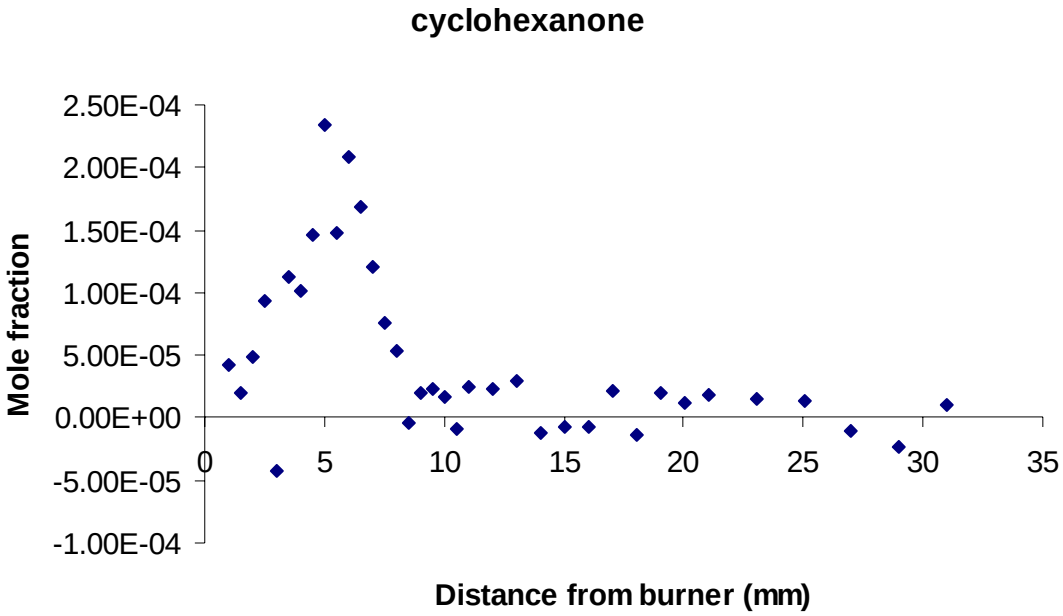

Figure 3.32. Mole-fraction profile of cyclohexanone.

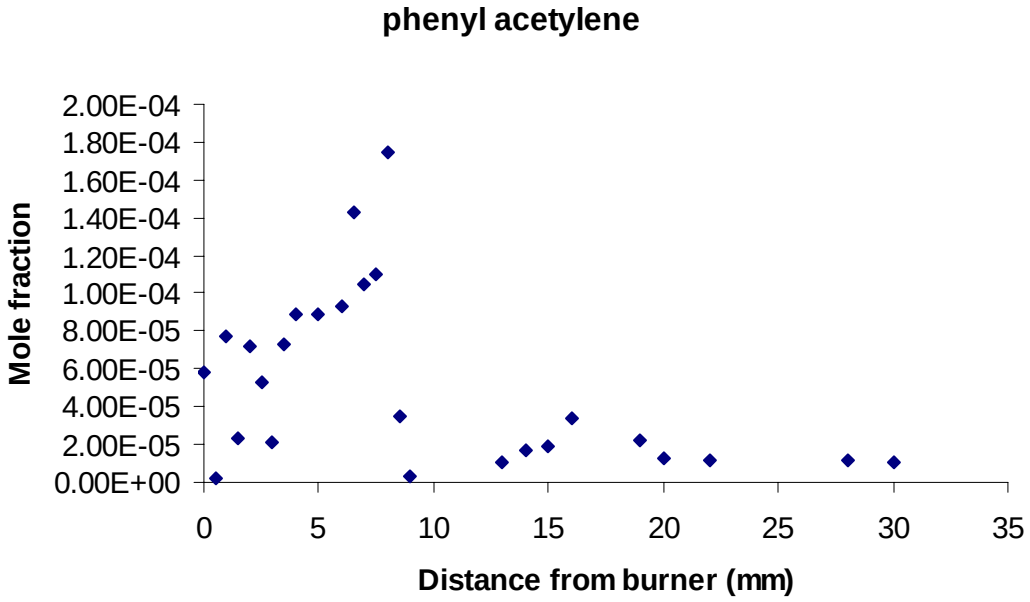

Figure 3.33. Mole-fraction profile of phenylacetylene.

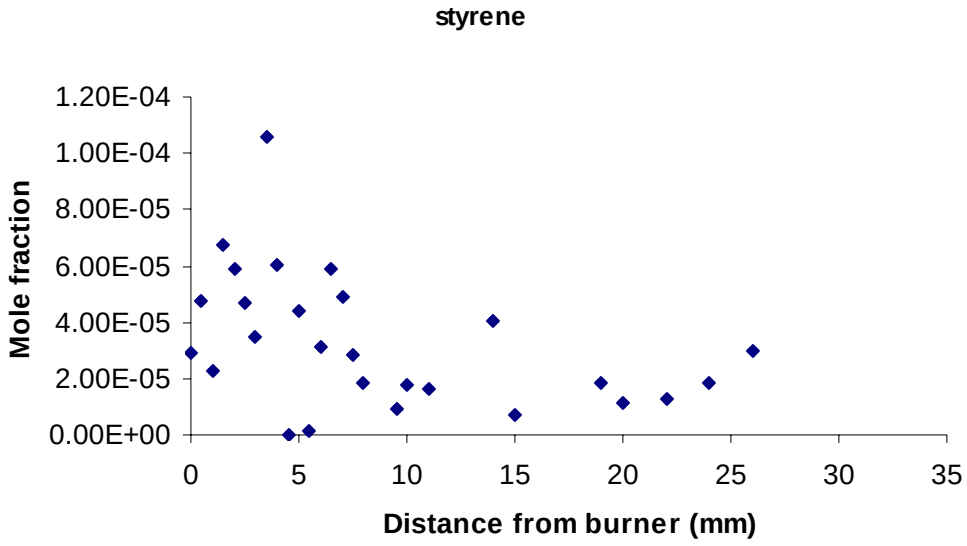

Figure 3.34. Mole-fraction profile of styrene.

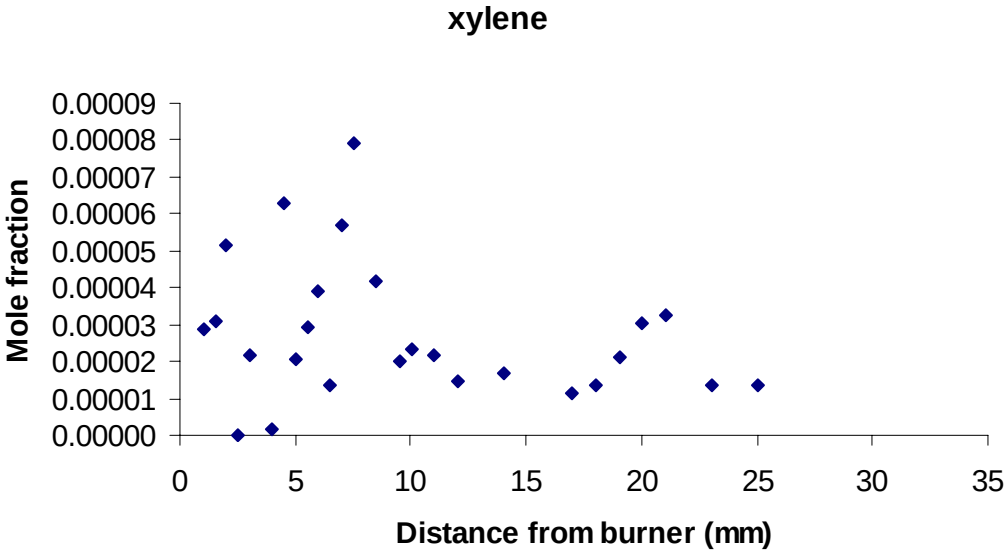

Figure 3.35. Mole-fraction profile of xylene.

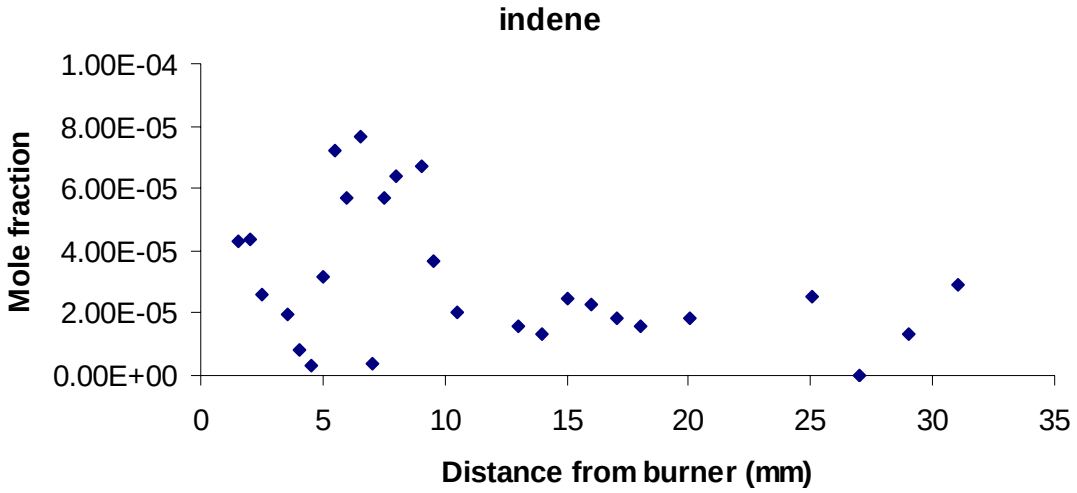

Figure 3.36. Mole-fraction profile of indene.

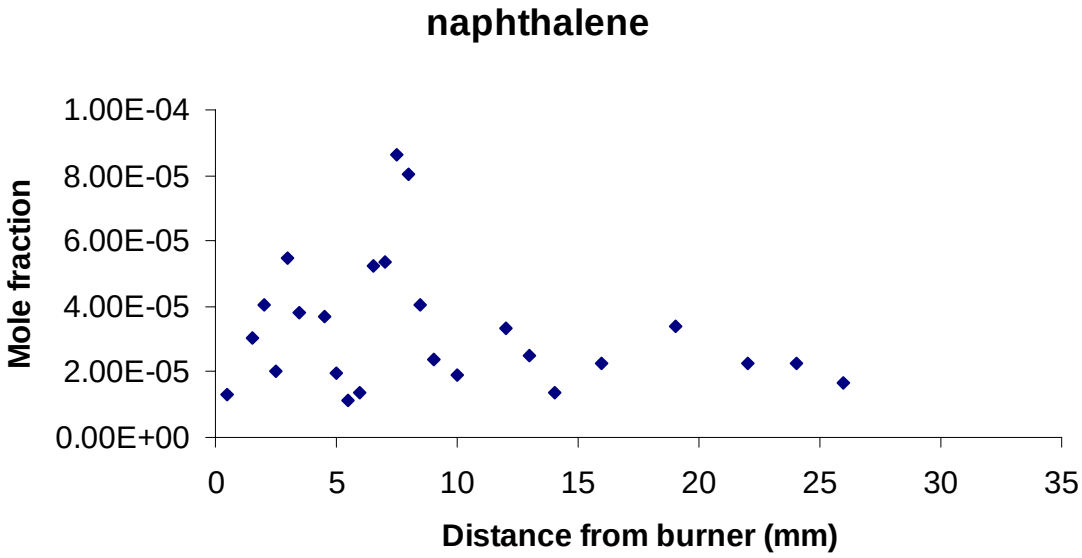

Figure 3.37. Mole-fraction profile of naphthalene.

Mass 16. The mass 16 signal was identified as methane (CH_4). The CH_4 was not detected in the low-energy scan as it has an ionization energy of 12.61 eV. A 13.2 eV burner scan was used to obtain the methane mole-fraction profile. The methane mole-

fraction profile is reported in Figure 3.4. The mole-fraction profile showed a peak at 7.02 mm from the burner.

Mass 18. The mass 18 signal was identified as water. Like methane, water has an ionization energy (12.621 eV) which is higher than the energy range used for the energy scan. The mass 18 signal observed at 13.2 eV burner scan showed a gradual increase of the species away from the burner and then it remained steady throughout the post-flame zone. The mole-fraction profile of water is given in Figure 3.1.

Mass 26. The mass 26 species was not detected in the low-energy scan range of 8 to 10.7 eV. In a 12.3 eV burner scan, the species showing up at mass 26 was identified as acetylene (C_2H_2) based on the mass number and the shape of the profile. Acetylene has a literature ionization energy of 11.4 ±0.002 eV. The mass 26 species did not show up at 10 and 10.5 eV burner scans but was found in an 11.5 eV burner scan. Furthermore, acetylene is a common species found in hydrocarbon flames. Hence the mass 26 species was considered as acetylene. The mole-fraction profile is depicted in Figure 3.5. The profile shows a peak at 9.52 mm from the burner.

Mass 28. Two mass 28 species were reported in the cyclohexane flame. Ethylene (C_2H_4) showed up at 10.469 eV in the energy scan. The second mass species was identified as carbon monoxide (CO). The mass 28 signal showed a peak at 12.3 eV, but at 14.35 eV it showed a strong signal that gradually increased and then stayed almost constant towards the post-flame zone. The species that showed up above 12.3 eV was identified as CO, a species found in all hydrocarbon flames. C_2H_4 signal was extrapolated from 12.3 eV to 14.35 eV signal using the photoionization cross section of C_2H_4 at those two energies. The extrapolated signal of C_2H_4 was then subtracted from total mass 28

signal at 14.35 eV. This subtracted signal was considered to be the signal due to CO and was converted to mole fraction of CO. The peak for the C_2H_4 signal was observed at 8.02 mm from the burner. The CO mole fraction showed a gradual increase up to 11.02 mm and then did not change much.

Mass 29. The mass 29 species was identified as formyl radical (HCO). Figure 3.8 depicts its mole-fraction profile. A burner scan at 10.00 eV was used to get its mole-fraction profile. The profile shows a peak at 7.52 mm from the burner.

Mass 30. The mass 30 species was identified as formaldehyde (HCHO). Figure 3.9 depicts its mole-fraction profile. The profile shows a peak at 7.02 mm from the burner.

Mass 32. The mass 32 species was identified as molecular oxygen (O_2). Figure 3.1 depicts its mole-fraction profile along with other major species. The oxygen profile shows a decrease until 11 mm away from the burner, and then it remains close to zero.

Mass 39. The mass 39 species was identified as propargyl (C_3H_3). Figure 3.10 depicts its mole-fraction profile. The propargyl profile shows a peak at 9.02 mm away from the burner.

Mass 40. Three different species are present as mass 40 in the flame. They are argon, allene, and propyne. Allene showed up at approximately 9.7 eV and propyne showed up at approximately 10.3 eV. A burner scan at 10.0 eV was used to get the allene signal, while a burner scan at 10.5 eV had contributions from both the hydrocarbons. Using the cross photoionization cross sections of allene at 10 and 10.5 eV, allene signal was extrapolated to 10.5 eV, and the extrapolated allene was then subtracted from the combined signal to get the propyne signal. Argon did not show up at these energies as its

ionization energy is 15.759 eV. A burner scan at 16.2 eV was used to get the argon signal. As argon is fed into the burner and it is an inert gas, the argon signal is very high compared to allene and propyne. Hence the mass 40 signal at 16.2 eV burner scan was treated as pure argon to extract the mole-fraction profile. Figure 3.1 shows the mole-fraction profile for argon along with other major species in the flame. The argon mole-fraction profile showed a decrease from the burner to 9.52 mm, and then it remained steady. Argon is an inert gas that should not react in the flame, but this decrease is not due to reaction. Rather, as more and more CO, CO_2, and H_2O are produced, the total number of moles of exhaust gases increases, which decreases the mole fraction of argon although the number of moles of argon remains the same as it was in the inlet stream. Figure 3.11 shows the mole-fraction profiles for allene and propyne.

Mass 41. The mass 41 species was identified as allyl radical (C_3H_5). Figure 3.12 depicts its mole-fraction profile. A burner scan at 10.00 eV was used to get its mole-fraction profile. The profile shows a peak at 7.52 mm from the burner.

Mass 42. The mass 42 species was identified as propene (C_3H_6) and ketene (CH_2CO). Because these species have ionization-energy thresholds very close to each other (propene I.E. 9.73 and ketene 9.617), the signal of mass 42 could not be resolved into profiles for these separate identities. From the energy scan, it appears that the signal intensity for propene is much higher than ketene. Moreover, as this is a fuel-rich flame, it would be justified to consider that the oxygenate (ketene) would be lower in signal compared to the propene. Hence the mass 42 signal was treated as propene and its mole-fraction profile is depicted in Figure 3.12. A burner scan at 10.00 eV was used to measure its mole-fraction profile. The profile shows a peak at 7.02 mm from the burner.

Mass 44. The mass 44 species was identified as carbon dioxide (CO_2). CO_2 did not show up in the low-energy scan (8 to 10.7 eV) because it has higher ionization energy, but the mass 44 signal that was detected in 14.3 eV signal was considered to be CO_2. Its profile is shown in Figure 3.1 along with other major species.

Mass 50. The mass 50 species was identified as 1,3-butadiyne or diacetylene. Figure 3.13 depicts its mole-fraction profile. The profile shows a peak at 9.52 mm from the burner.

Mass 52. The mass 52 species was identified as 1-buten-3-yne. Figure 3.15 depicts its mole-fraction profile. The profile shows a peak at 8.52 mm from the burner.

Mass 54. The mass 54 species was identified as 1,3-butadiene. Figure 3.17 depicts its mole-fraction profile. The profile shows a peak at 7.02 mm from the burner.

Mass 55. The mass 55 species was identified as 1-buten-3-yl radical. Figure 3.16 depicts its mole-fraction profile. A burner scan at 10.00 eV was used to get its mole-fraction profile. The profile shows a peak at 9.02 mm from the burner.

Mass 56. The mass 56 species was identified as a mixture of 1-butene (C_4H_8) and 2-butene (C_4H_8). As both of these species have ionization energy thresholds very close to each other (1-butene at 9.55 and 2-butene at 9.13 eV), the signal of mass 56 could not be resolved into profiles for separate identities. From the energy scan, it seems that the signal intensity for 1-butene is much higher than 2-butene. Hence the mass 56 signal was treated as 1-butene, and its mole-fraction profile is depicted in Figure 3.19. A burner scan at 10.00 eV was used to get its mole-fraction profile. The profile shows a peak at 6.52 mm from the burner.

Mass 64. The mass 64 species was identified as 1,3-pentadiyne (C_5H_4). Figure 3.20 depicts its mole-fraction profile. A burner scan at 10.00 eV was used to get its mole-fraction profile. The profile shows a peak at 5.52 mm from the burner.

Mass 65. The mass 65 species was identified as cyclopentadienyl radical (C_5H_5). Figure 3.21 depicts its mole-fraction profile. A burner scan at 10.00 eV was used to get its mole-fraction profile. The profile shows a peak at 7.52 mm from the burner.

Mass 66. The mass 66 species was identified as 1,3-cyclopentadiene (C_5H_6). Figure 3.22 depicts its mole-fraction profile. A burner scan at 10.00 eV was used to get its mole-fraction profile. The profile shows a peak at 7.52 mm from the burner.

Mass 68. This species was identified as 1,3-pentadiene (C_5H_8). Figure 3.23 depicts its mole-fraction profile. A burner scan at 10.00 eV was used to get its mole-fraction profile. The profile shows a peak at 7.02 mm from the burner.

Mass 70. The mass 70 species was identified as 2-pentene (C_5H_{10}). Figure 3.24 depicts its mole-fraction profile. A burner scan at 10.00 eV was used to get its mole-fraction profile. The profile shows a peak at 5.52 mm from the burner.

Mass 74. The mass 74 species was identified as 1,3,5-hexatriyne or triacetylene(C_6H_2). Figure 3.25 depicts its mole-fraction profile. A burner scan at 10.00 eV was used to get its mole-fraction profile. The profile shows a peak at 9.52 mm from the burner.

Mass 76. The mass 76 species was identified as benzyne (C_6H_4). Figure 3.26 depicts its mole-fraction profile. The profile shows a peak at 9.02 mm from the burner.

Mass 78. The PIE scan of mass 78 signal showed two different species, fulvene (C_6H_6, I.E. 8.36 eV) and benzene (C_6H_6, I.E. 9.243 eV). From the PIE scan it was evident

that benzene was the dominant species at mass 78. Hence the total mass 78 signal was considered to be benzene, and its mole fraction was obtained. Figure 3.27 depicts the benzene mole-fraction profile. It shows a peak at 8.02 mm from the burner.

Mass 80. The mass 80 species was identified as 1,3-cyclohexadiene (C_6H_8). Figure 3.26 depicts its mole-fraction profile. The profile shows a peak at 7.52 mm from the burner.

Mass 82. The mass 82 species was identified as cyclohexene (C_6H_{10}). Figure 3.27 depicts its mole-fraction profile. A burner scan at 10.00 eV was used to get its mole-fraction profile. The profile shows a peak at 6.52 mm from the burner.

Mass 83. The mass 83 species was identified as cyclohexyl radical (C_6H_{11}). Figure 3.27 depicts its mole-fraction profile. The profile shows a peak at 5.52 mm away from the burner.

Mass 84. The mass 84 species was identified as cyclohexane (C_6H_{12}). Figure 3.28 depicts its mole-fraction profile. As cyclohexane is the fuel, it is oxidized until after 7.5 mm from the burner, it is barely detectable.

Mass 92. The mass 92 species was identified as toluene (C_7H_8). Figure 3.29 depicts its mole-fraction profile. It shows a peak at 6.5 mm from the burner.

Mass 94. The mass 94 species was identified as phenol (C_6H_6O). Figure 3.30 depicts its mole-fraction profile. It shows a peak at 5.02 mm from the burner.

Mass 98. The mass 96 species was identified as cyclohexanone ($C_6H_{10}O$). Figure 3.31 depicts its mole-fraction profile. It shows a peak at 5.52 mm from the burner.

Mass 102. The mass 102 species was identified as phenylacetylene (C_8H_6). Figure 3.31 depicts its mole-fraction profile. It shows a peak at 8 mm from the burner.

Mass 104. The mass 104 species was identified as styrene (C_8H_8). Figure 3.32 depicts its mole-fraction profile. It is a scattered signal and the peak cannot be identified from it.

Mass 106. The mass 106 species was identified as para-xylene (C_8H_{10}). Figure 3.33 depicts its mole-fraction profile. It had a weak and scattered signal as well, and at 7.52 mm it seemed there was a peak.

Mass 116. The mass 116 species was identified as indene (C_9H_8). Figure 3.34 depicts its mole-fraction profile. It a weak and scattered signal as well and at 6.52 mm it seems there is a peak.

Mass 128. The mass 128 species was identified as naphthalene ($C_{10}H_8$). Figure 3.35 depicts its mole-fraction profile. It was a weak and scattered signal as well, and at 7.52 mm away from the burner it seemed there was a peak.

3.2.2. Checks of mole-fraction-profile analysis

The mole-fraction profile obtained from the flame data was checked with the initial feed composition, and a mole balance was performed with hydrogen and carbon atom balance in the feed and the post-flame zone of the flame.

The initial mole fractions of the feed gases going into the burner were obtained from the feed conditions of the cyclohexane flame. These values were then compared against the mole-fraction data achieved for the first data point away from the burner. The comparison is tabulated in Table 3.3.

Table 3.3. Comparison of mole fraction of the feed and to the first data point away from the burner.

	Mole fraction in the feed gas	Mole fraction at 1.02 mm from the burner
Cyclohexane	0.127	0.0891
Oxygen	0.570	0.502
Argon	0.303	0.278

The mole fractions of cyclohexane, oxygen, and argon obtained at 1.02 mm away from the burner are lower than their respective values in the feed. This result was expected because at 1.02 mm away from the burner, the oxidation reactions have already started. As a result, the mole fractions of cyclohexane and oxygen should be slightly lower than their respective values in the feed. The argon mole fraction should be slightly decreased as well, as explained previously.

The mole balances for hydrogen and carbon atom are described below. Initially 100 moles of feed gas was assumed. This gave 12.7 mole of cyclohexane in the feed, which further gave 76.2 moles of C and 152.4 moles of hydrogen in the inlet gas.

In the post-flame zone, the dominant gases are Ar (15.9%), CO (33.4%), H_2O (30.3%), CO_2 (8.65%), C_2H_2 (1.55%), H_2 (8.17%) and O_2 (2.25%). The carbon balance accounting for CO, CO_2 and C_2H_2 is only 86.04 %. Hence, the carbon mole balance in the post-flame zone overshoots the inlet carbon moles.

The hydrogen (H atom) mole balance in the post-flame zone accounting for post-flame H_2O, H_2, C_2H_2 was 152.9 mole. This value slightly overpredicts the initial number of moles of hydrogen atom in the feed gas.

The overprediction of carbon was estimated in this case as there is no detection of O, H and OH in the flame. In the post-flame zone, these species represent significant amounts (1 to 4 percent) and thus should lower the Ar, CO and CO_2 mole fraction. The

mole balance depends on the Ar mole fraction in the post flame zone (we consider Ar as an inert species and the total number of moles of exhaust gas generated from 100 mole of feed gas is calculated from the Ar mole fractions). This would moderate the C overprediction.

3.2.3 Temperature profile of the cyclohexane flame

The temperature profile of the cyclohexane flame was measured as discussed in Chapter 2. Figure 3.38 represents the temperature profile for the cyclohexane flame. The heated and unheated temperature profile is depicted in the figure. The experimental data points were fitted through a polynomial to get the smoothed temperature profile.

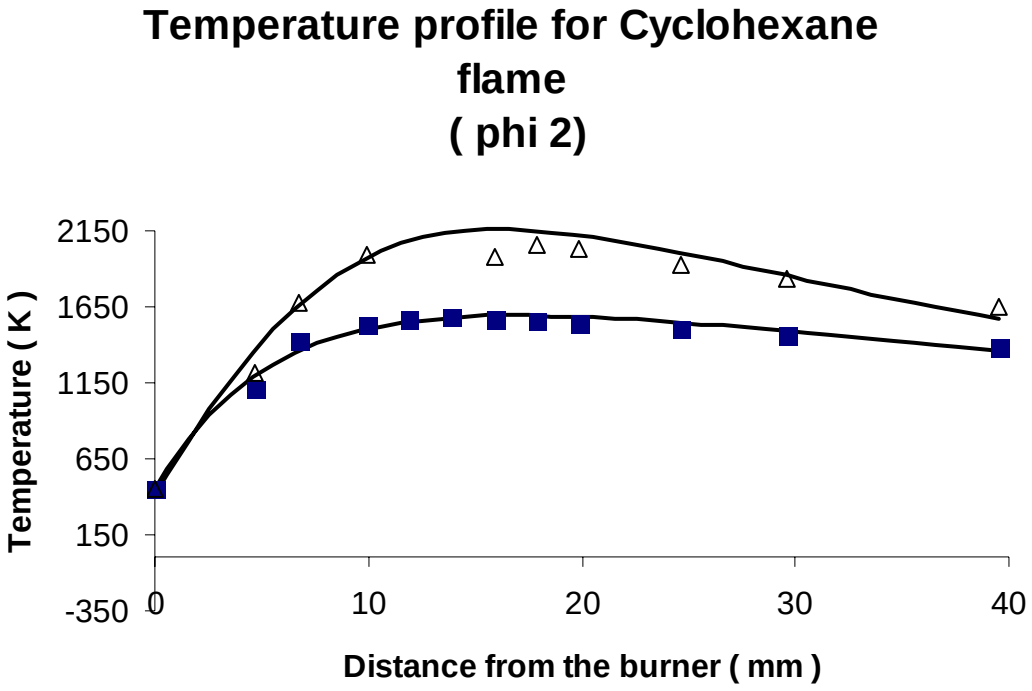

Figure 3.38. Temperature profile for the fuel-rich cyclohexane flame (Δ refers to heated temperature profile, ■ refers to unheated temperature profile).

3.3 Toluene flame (Φ = 0.895) data analysis

The fuel-lean toluene flame feed conditions are tabulated in Table 3.4.

Table 3.4 Condition for the fuel-lean toluene flame.

	Flow Rates	Pressure in the reaction chamber	Fuel equivalence ratio (Φ)
Toluene	0.8 ml/min	15 Torr	0.895
Oxygen	1.69 SLM		
Argon	1.858 SLM		

The species identified in the toluene flame are reported in Table 3.4. The description of the mole-fraction profiles of these species follows below. An 8.00 to 11.155 eV energy scan is used to identify the species in the toluene flame.

Table 3.5. List of species measured in the fuel-lean toluene flame, ionization energies of the species as reported in (NIST Chemistry WebBook), ionization energy observed, and ionization energy used to measure the profile.

AMU	Species Identified	Ionization energy from literature (eV)	Ionization energy observed (eV)	Burner scan Energy (eV)
1	H	13.59844	-	14.37
2	H_2	15.42593±0.00005	-	16.22
15	Methyl (CH_3) radical	9.84±0.01	9.83	10.06
16	Methane (CH_4)	12.61±0.01	-	13.22
16	Oxygen atom (O)	13.61806	-	14.37
17	Hydroxyl radical (OH)	13.017±0.002	-	13.22
18	Water (H_2O)	12.621 ±0.002	-	13.22
26	Acetylene (C_2H_2)	11.4±0.002	-	12.32
28	Ethylene (C_2H_4)	10.5138±0.0006	10.53	12.32
30	Formaldehyde	10.88±0.01	10.88	11.52
32	Oxygen (O_2)	12.0697±0.0002		12.32
39	Propargyl (C_3H_3) radical	8.67±0.02	8.73	10.06
40	Allene (C_3H_4)	9.692±0.004	9.675	10.06
40	Propyne (C_3H_4)	10.36±0.01	10.319	10.52
40	Argon (Ar)	15.759±0.001		16.22
42	Ketene(C_2H_2O)	9.617±0.003	9.625	11.52
44	Carbon dioxide (CO_2)	13.797±0.001		14.37
50	1,3-Butadiyne (C_4H_2)	10.17	10.119	10.52

AMU	Species Identified	Ionization energy from literature (eV)	Ionization energy observed (eV)	Burner scan Energy (eV)
52	1-Buten-3-yne (C_4H_4)	9.58±0.02	9.575	10.06
54	1,3-Butadiene (C_4H_6)	9.072±0.007	9.075	10.06
56	Methoxyacetylene (C_3H_4O)	9.48	9.525	10.06
64	1,3-Pentadiyne (C_5H_4)	9.5 ± 0.02	9.505	10.06
65	Cyclopentadienyl (C_5H_5) radical	8.41/8.56	8.505	10.06
66	1,3-Cyclopentadiene (C_5H_6)	8.57 ± 0.01	8.58	10.06
68	1,2-Butadienone (C_4H_4O)	8.68±0.05	8.68	10.06
74	1,3,5-Hexatriyne (C_6H_2)	9.5±0.02	9.48	10.06
76	Benzyne (C_6H_4)	9.03±0.05	9.03	10.06
78	Fulvene (C_6H_6)	8.36	8.365	-
78	1,5-Hexadien-3-yne (C_6H_6)	8.5	8.43	-
78	Benzene (C_6H_6)	9.24378±0.00007	9.215	10.06
80	Methylcyclopentadiene (C_6H_8)	8.28±0.05	8.3	10.06
82	1,2 Butadienone 3 methyl (C_5H_6O)	8.65	8.63	10.06
90	1,3-Cyclopentadiene,5-ethenylidene (C_7H_6)	8.29	8.275	10.06
91	Benzyl radical (C_7H_7)	7.242±0.006	Below 8	10.06
92	Toluene (C_7H_8)	8.828±0.001	8.825	10.06
94	Phenol (C_6H_6O)	8.49±0.02	8.525	10.06
102	Phenylacetylene (C_8H_6)	8.82±0.02	8.825	10.06
104	Styrene (C_8H_8)	8.464±0.001	8.43	10.06
106	Paraxylene (C_8H_{10})	8.44±0.05	8.375	10.06
106	Benzaldehyde (C_7H_6O)	9.5±0.08	9.48	10.06
108	Benzyl alcohol (C_7H_8O)	8.26±0.05	8.28	10.06
116	Indene (C_9H_8)	8.14±0.01	8.13	10.06

3.3.1 Mole-fraction profiles

The mole-fraction profiles of the species identified follows in an ascending mass number order. The photoionization cross sections used, their references, and the mass discrimination factors are given in Appendix A.

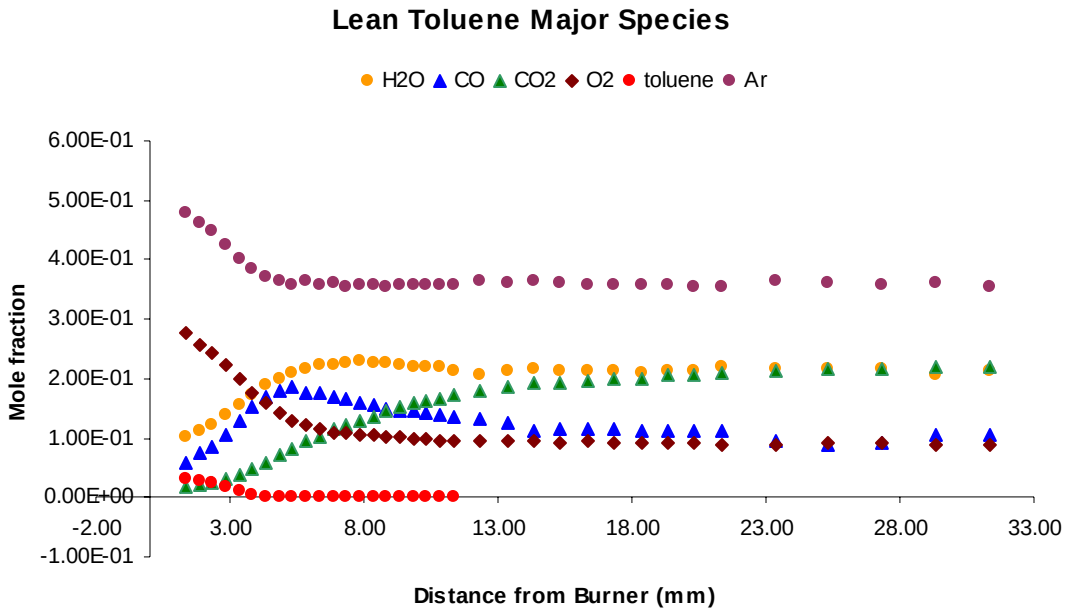

Figure 3.39. Mole fraction profiles of major species in the fuel-lean toluene flame.

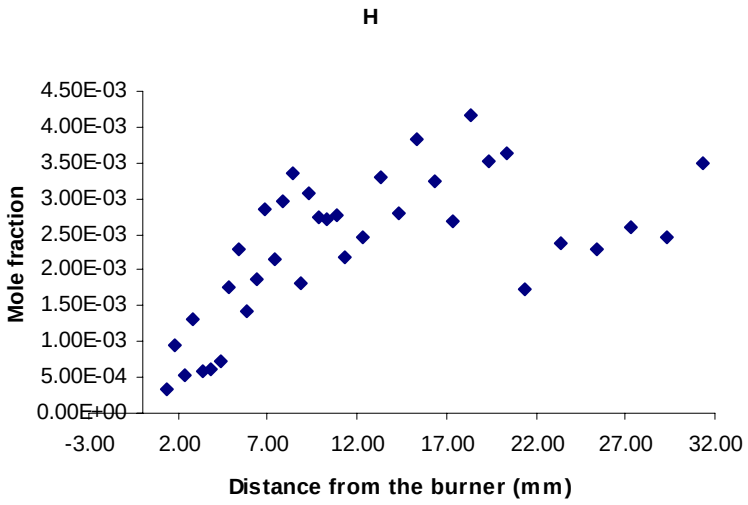

Figure 3.40. Mole fraction profile of H in the fuel-lean toluene flame.

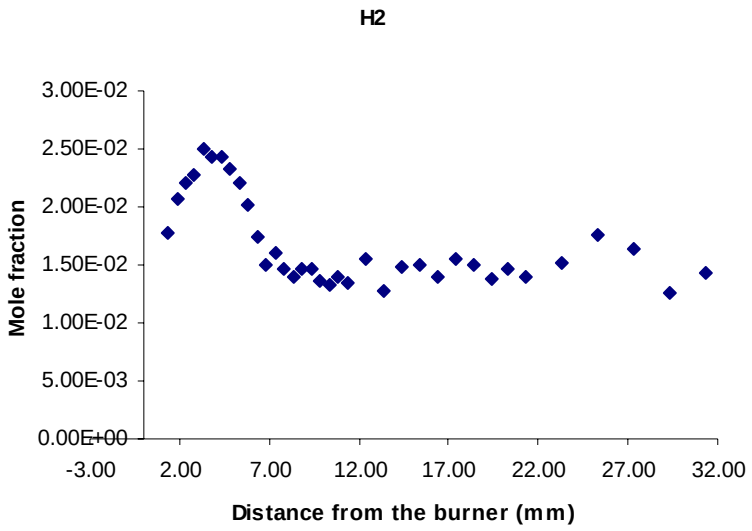

Figure 3.41. Mole fraction profile of H_2 in the fuel-lean toluene flame.

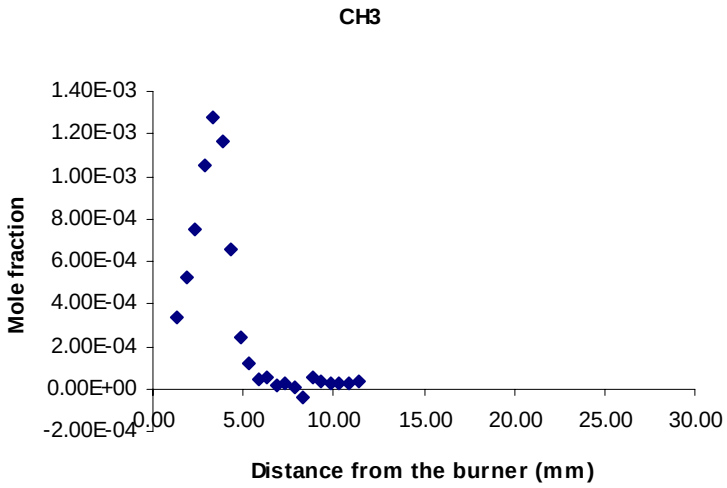

Figure 3.42. Mole fraction profile of CH_3 in the fuel-lean toluene flame.

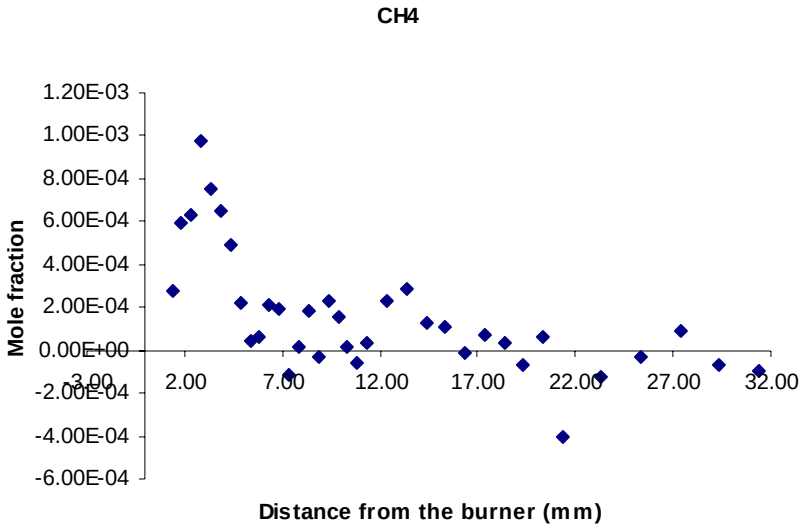

Figure 3.43. Mole fraction profile of CH_4 in the fuel-lean toluene flame.

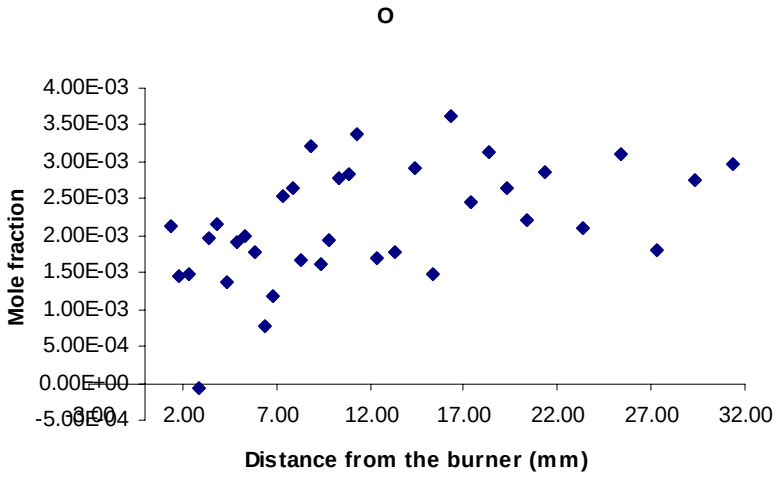

Figure 3.44. Mole fraction profile of O in the fuel-lean toluene flame.

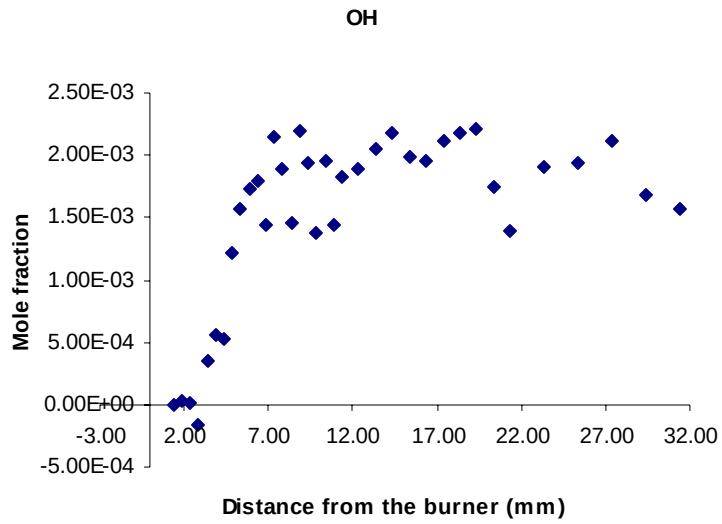

Figure 3.45. Mole fraction profile of OH in the fuel-lean toluene flame.

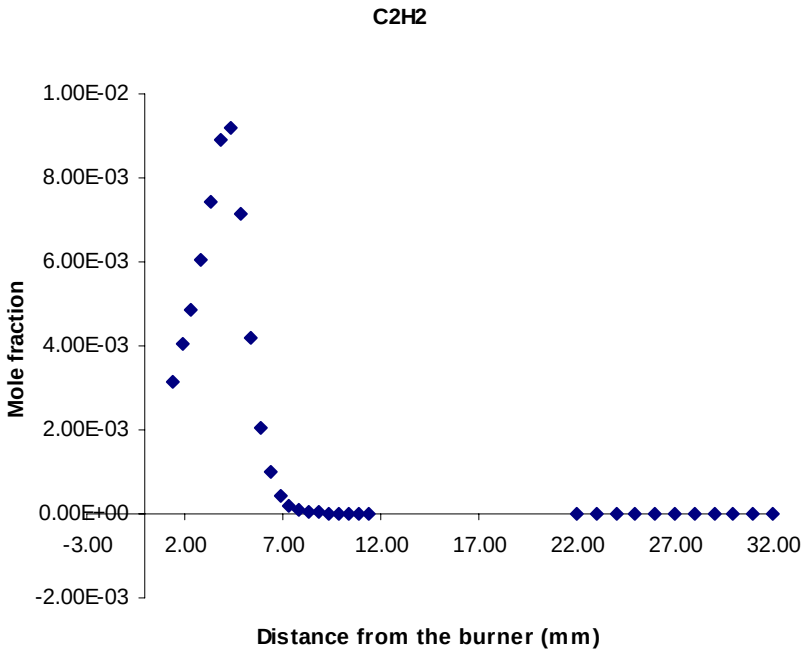

Figure 3.46. Mole fraction profile of C_2H_2 in the fuel-lean toluene flame.

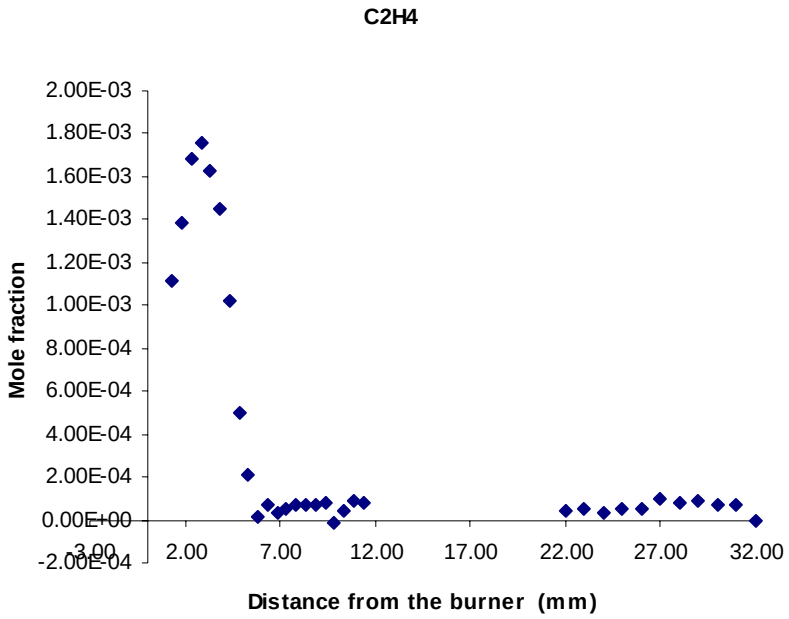

Figure 3.47. Mole fraction profile of C_2H_4 in the fuel-lean toluene flame.

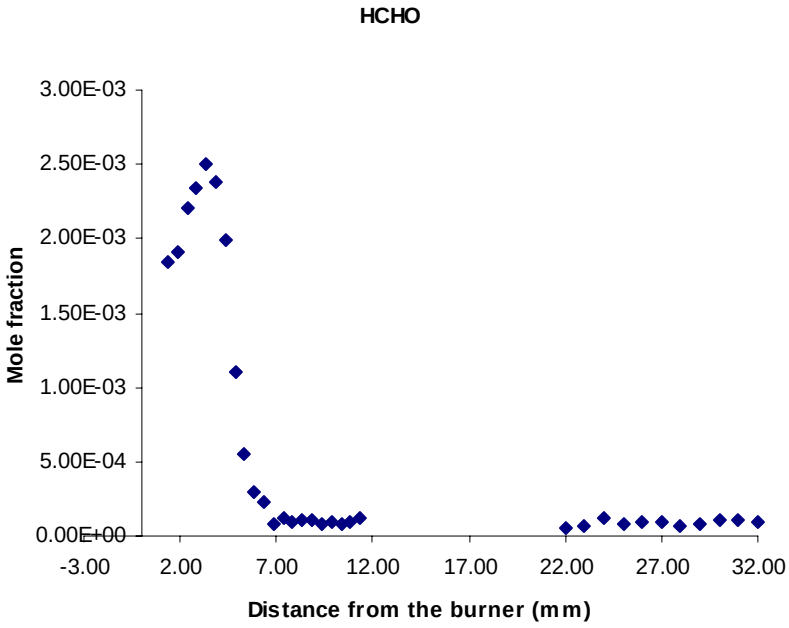

Figure 3.48. Mole fraction profile of HCHO in the fuel-lean toluene flame.

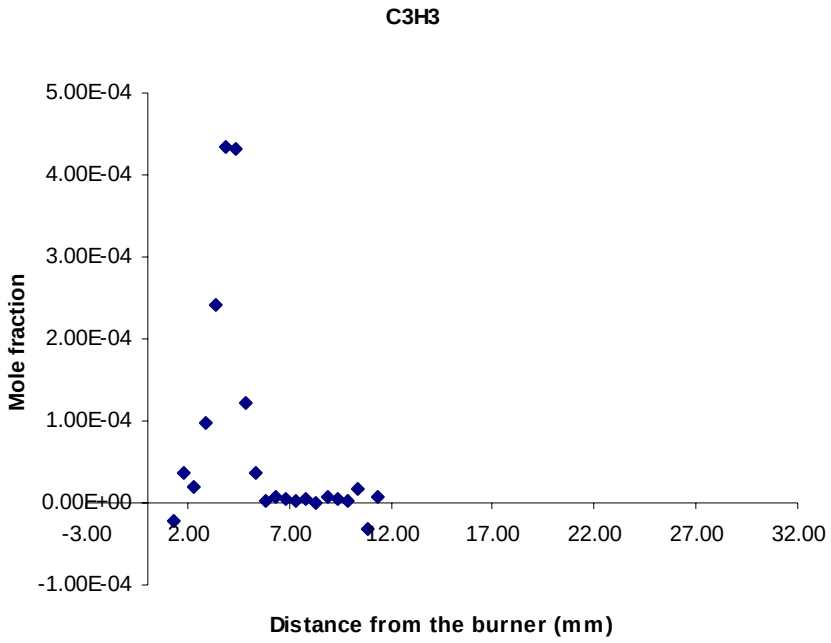

Figure 3.49. Mole fraction profile of C_3H_3 in the fuel-lean toluene flame.

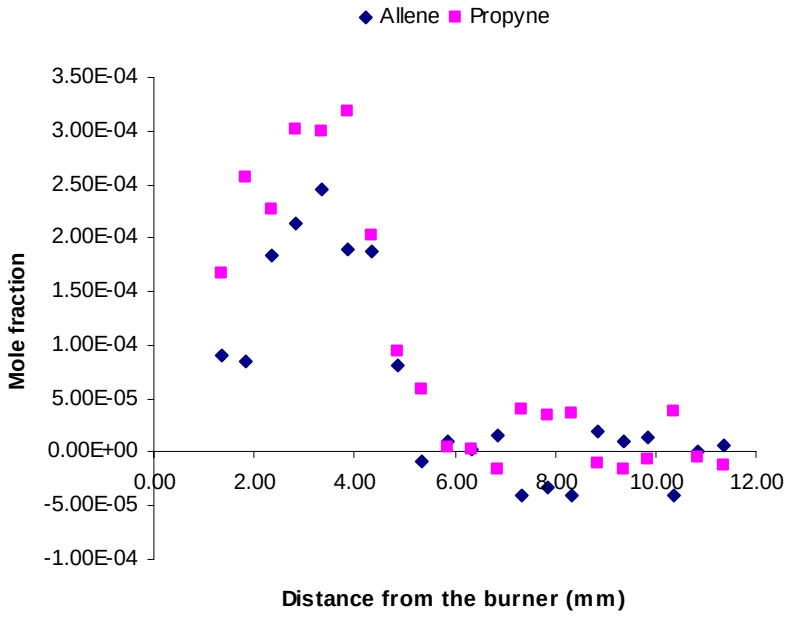

Figure 3.50. Mole fraction profile of allene and propyne in the fuel-lean toluene flame.

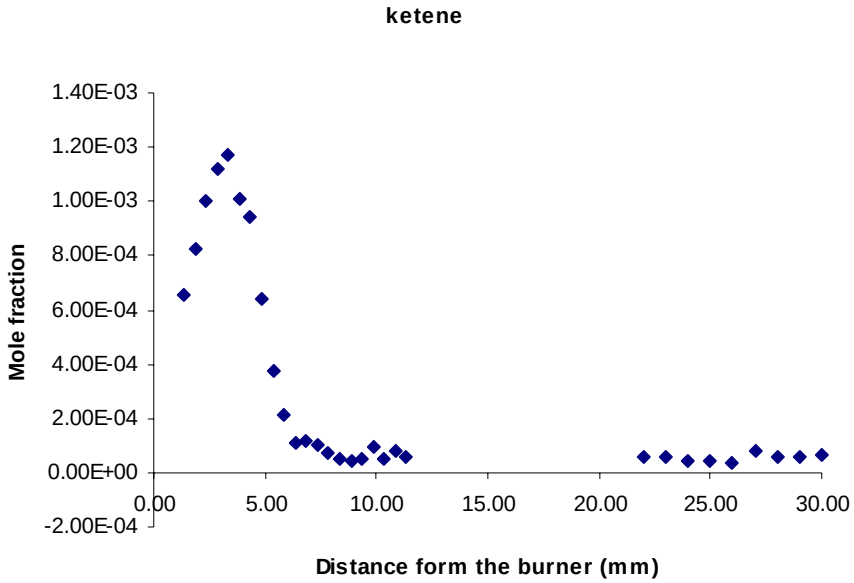

Figure 3.51. Mole fraction profile of ketene in the fuel-lean toluene flame.

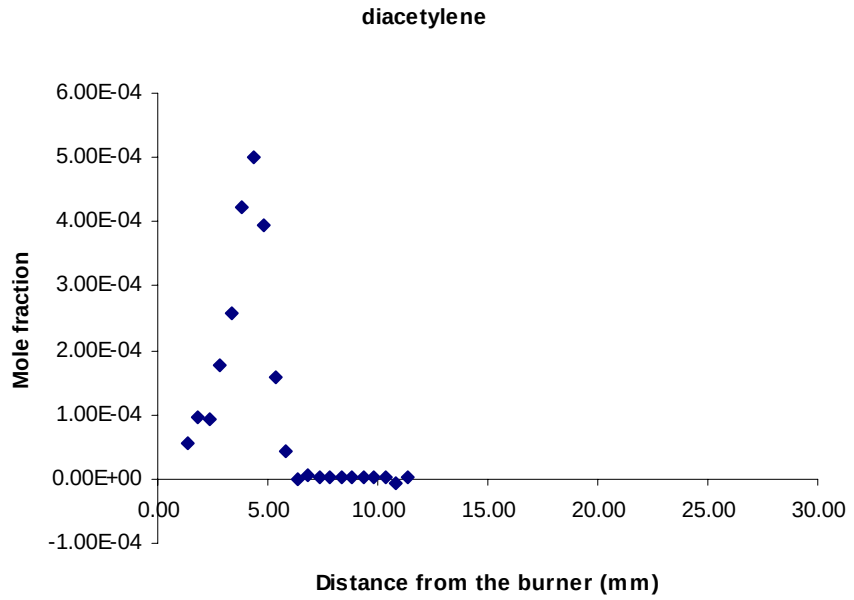

Figure 3.52. Mole fraction profile of diacetylene in the fuel-lean toluene flame.

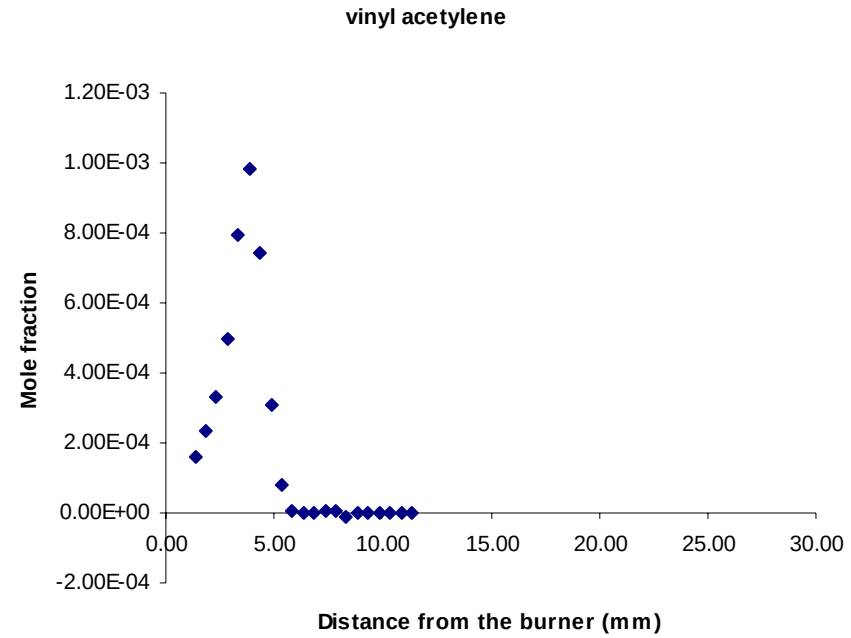

Figure 3.53. Mole fraction profile of vinylacetylene in the fuel-lean toluene flame.

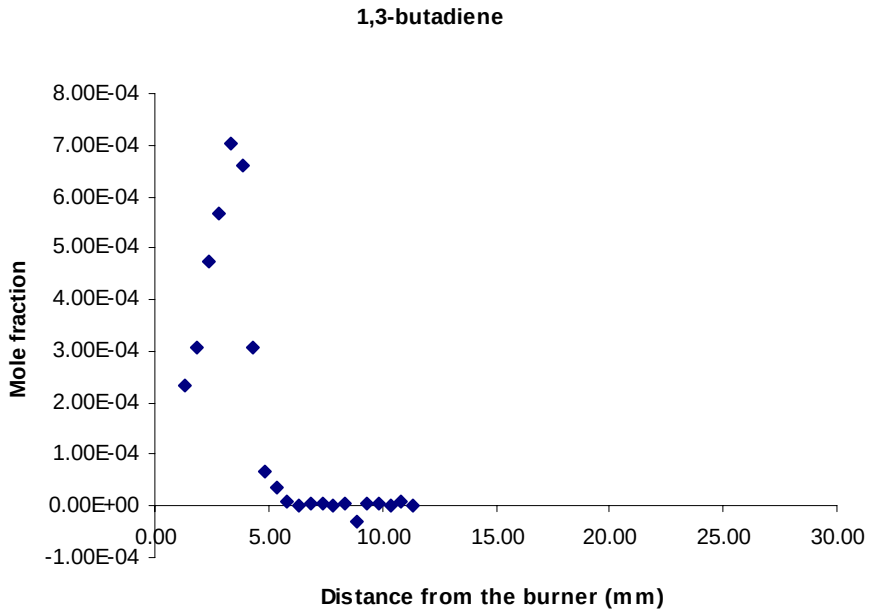

Figure 3.54. Mole fraction profile of 1,3-butadiene in the fuel-lean toluene flame.

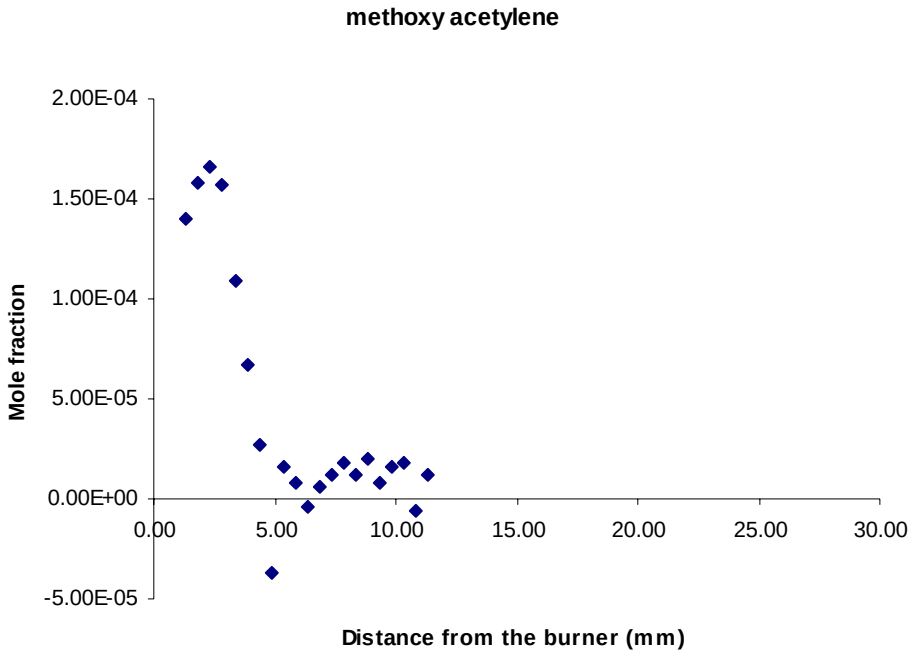

Figure 3.55. Mole fraction profile of methoxyacetylene in the fuel-lean toluene flame.

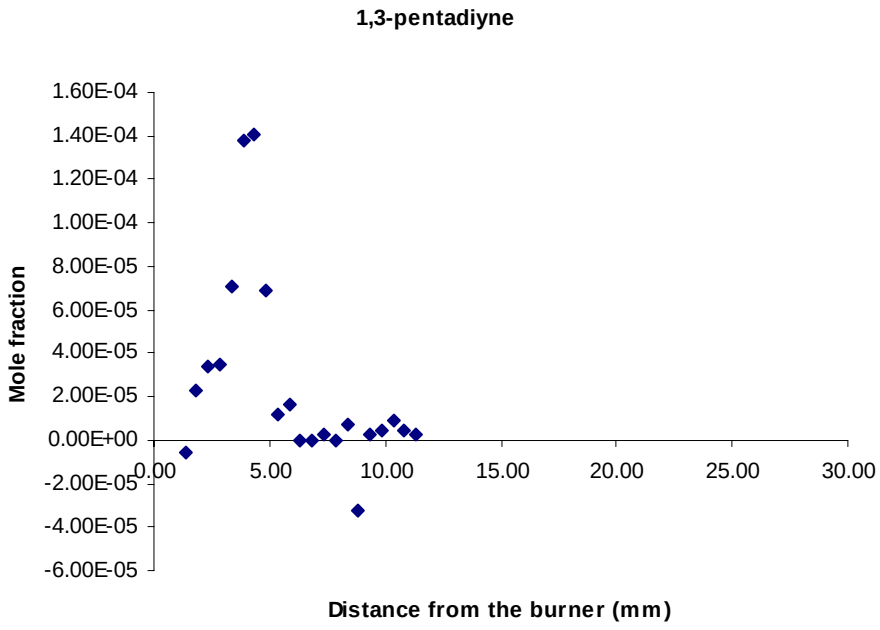

Figure 3.56. Mole fraction profile of 1,3-pentadiyne in the fuel-lean toluene flame.

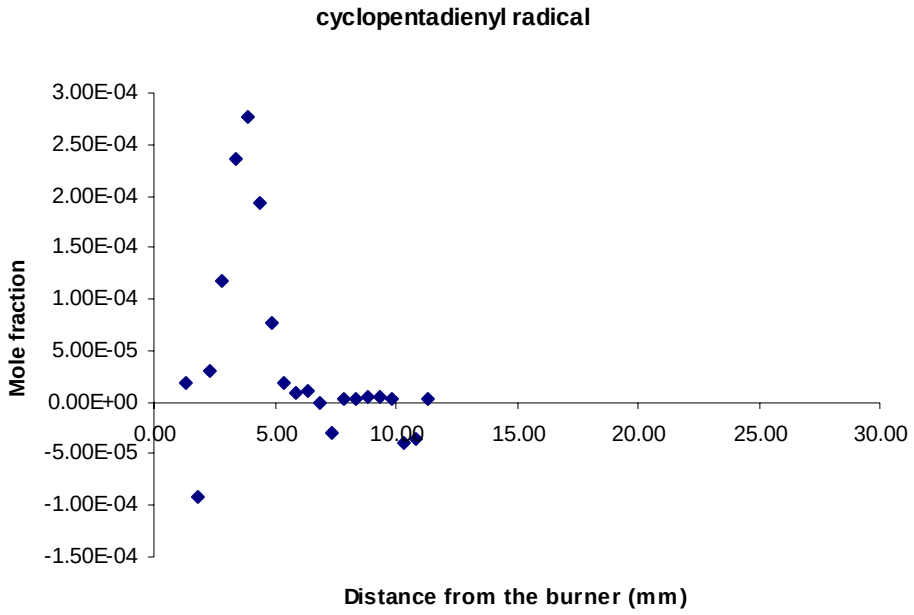

Figure 3.57. Mole fraction profile of cyclopentadienyl radical in the fuel-lean toluene flame.

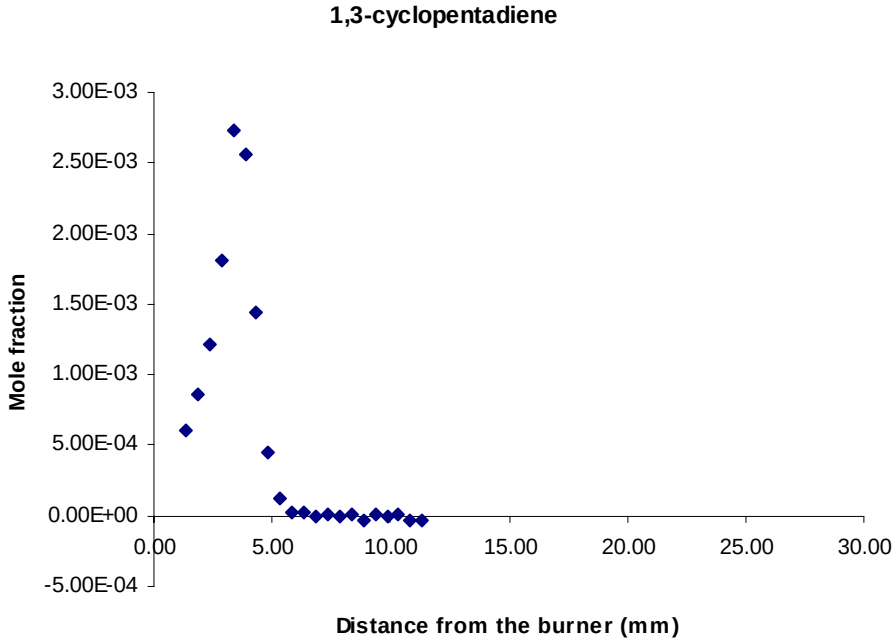

Figure 3.58. Mole fraction profile of 1,3-cyclopentadiene in the fuel-lean toluene flame.

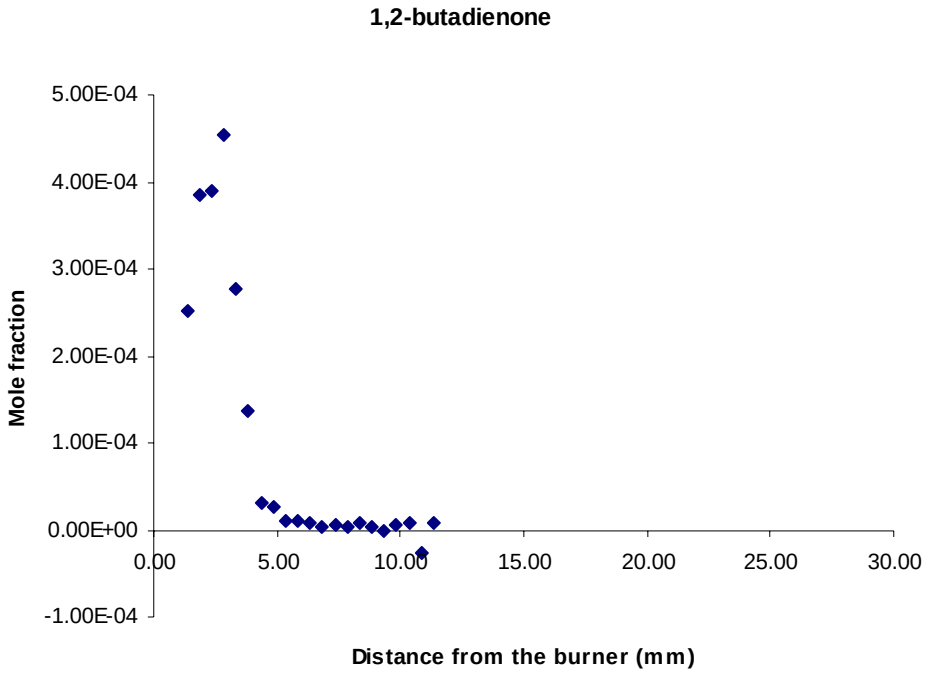

Figure 3.59. Mole fraction profile of 1,2-butadienone in the fuel-lean toluene flame.

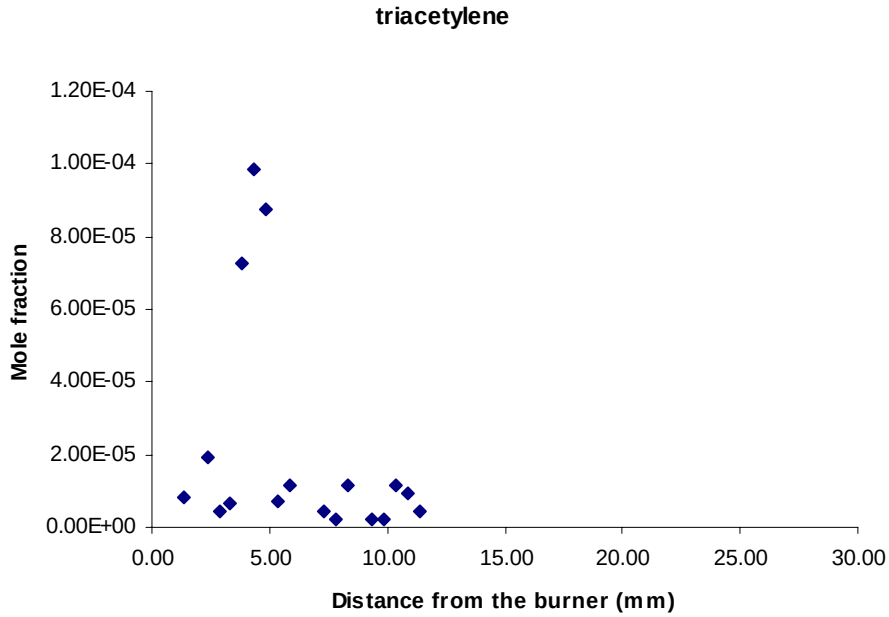

Figure 3.60. Mole fraction profile of triacetylene in the fuel-lean toluene flame.

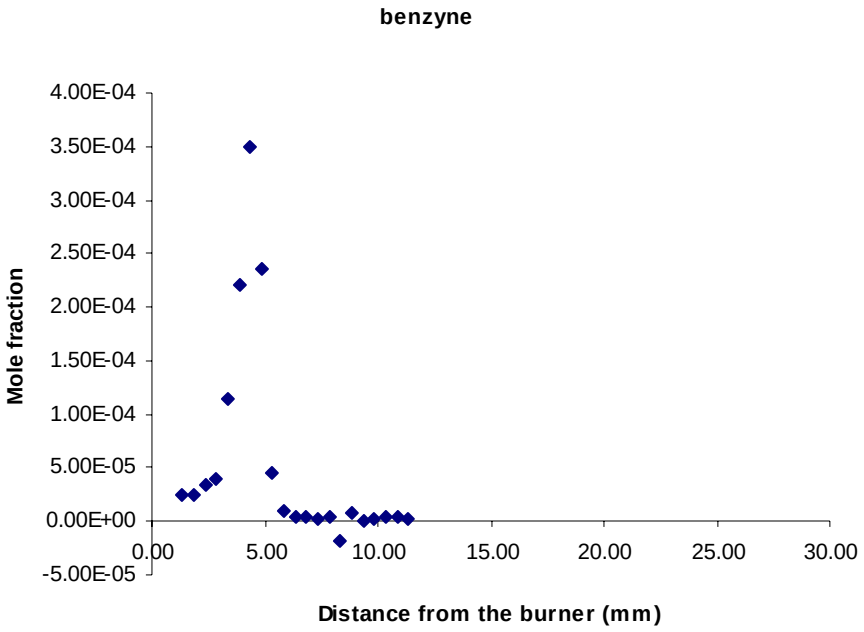

Figure 3.61. Mole fraction profile of benzyne in the fuel-lean toluene flame.

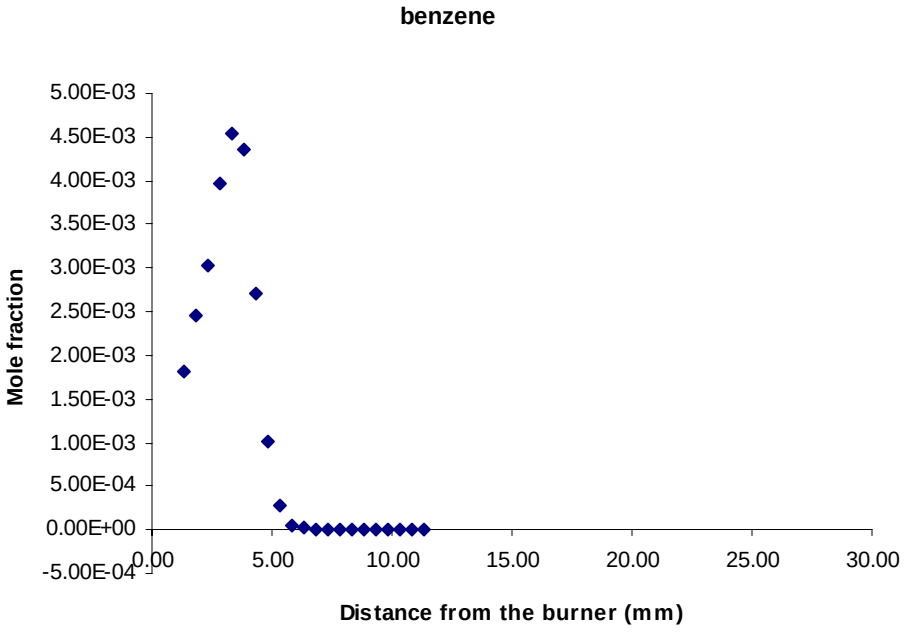

Figure 3.62. Mole fraction profile of benzene in the fuel-lean toluene flame.

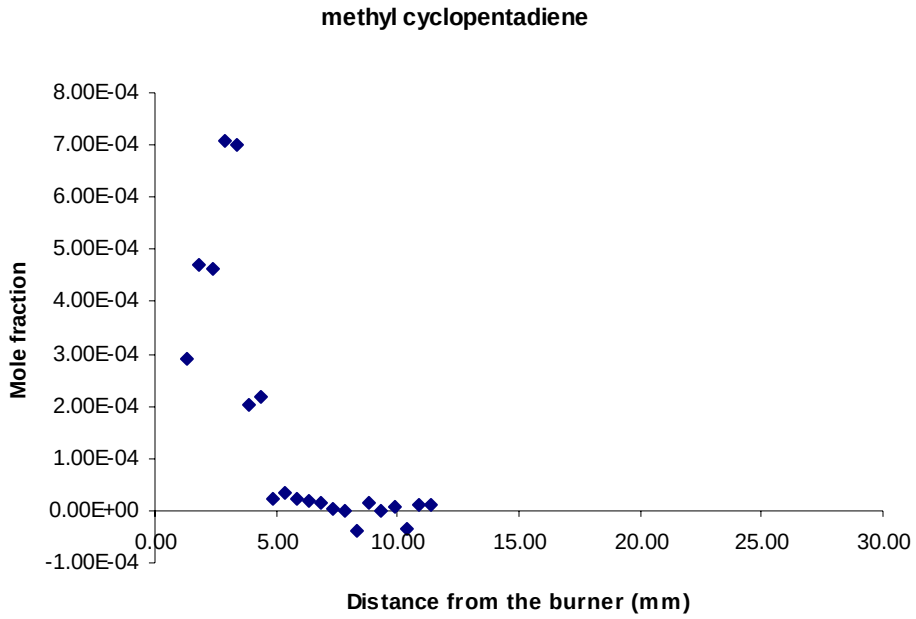

Figure 3.63. Mole fraction profile of methyl cyclopentadiene in the fuel-lean toluene flame.

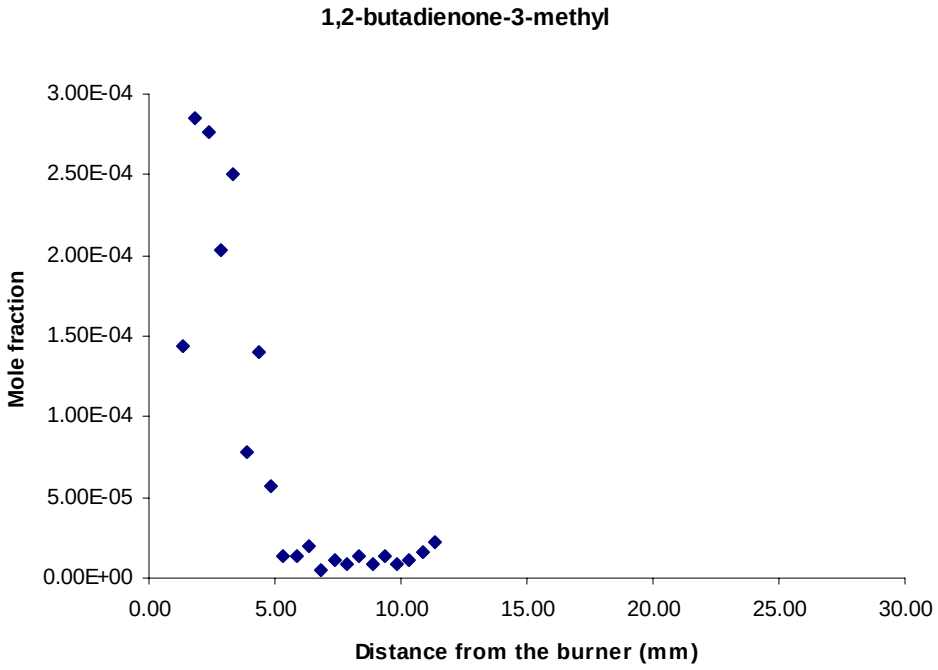

Figure 3.64. Mole fraction profile of 1,2-butadienone-3-methyl in the fuel-lean toluene flame.

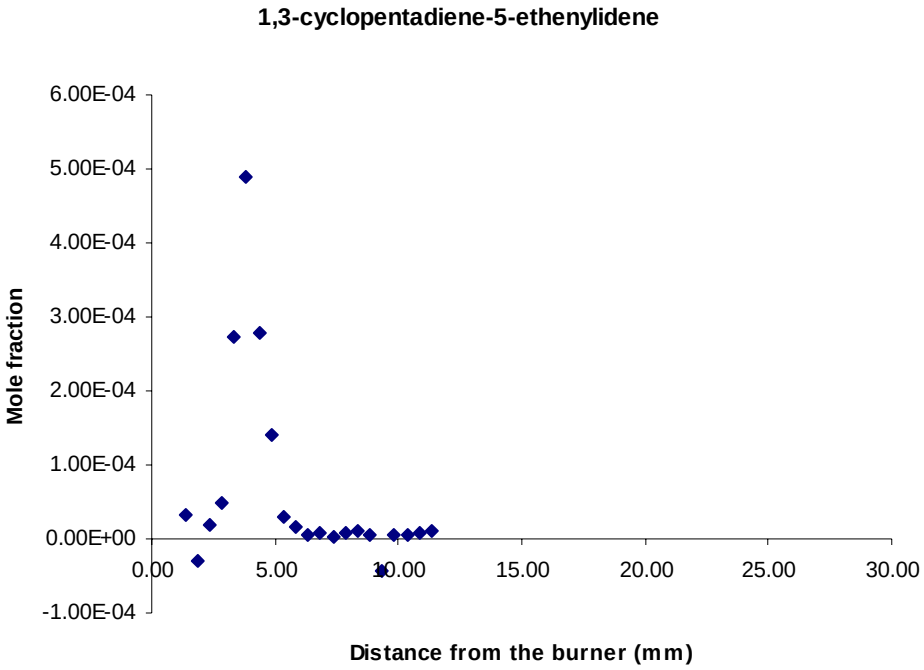

Figure 3.65. Mole fraction profile of 1,3-cyclopentadiene-5-ethenylidene in the fuel-lean toluene flame.

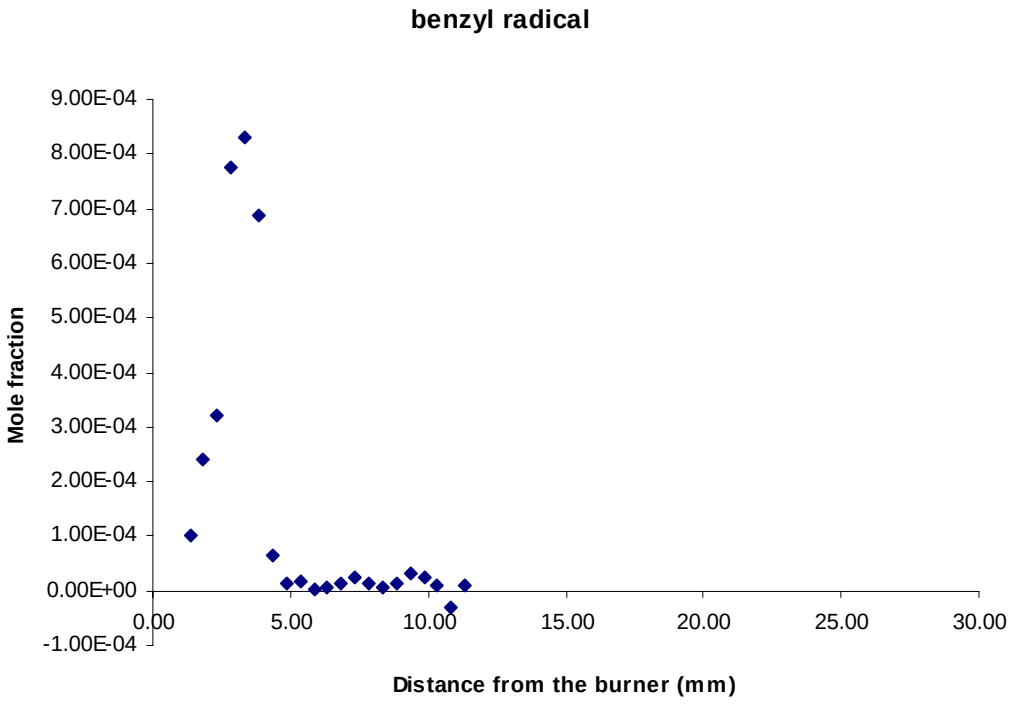

Figure 3.66. Mole fraction profile of benzyl radical in the fuel-lean toluene flame.

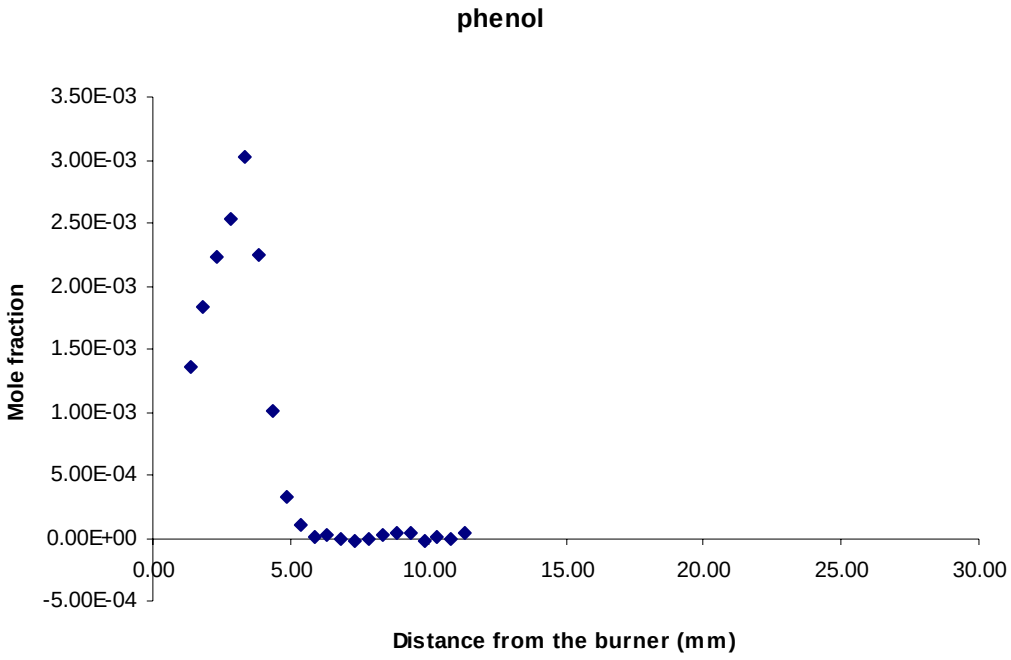

Figure 3.67. Mole fraction profile of phenol in the fuel-lean toluene flame.

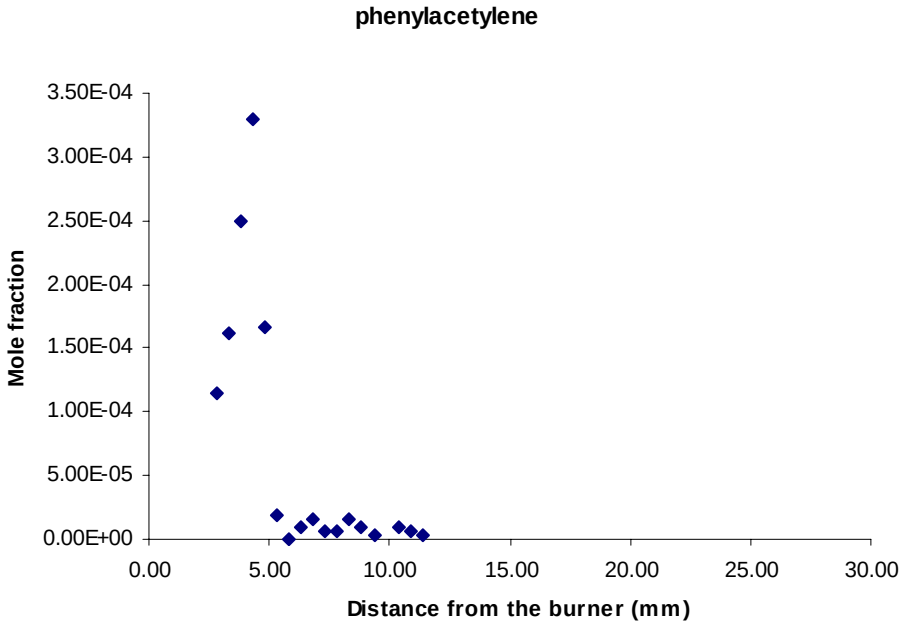

Figure 3.68. Mole fraction profile of phenylacetylene in the fuel-lean toluene flame.

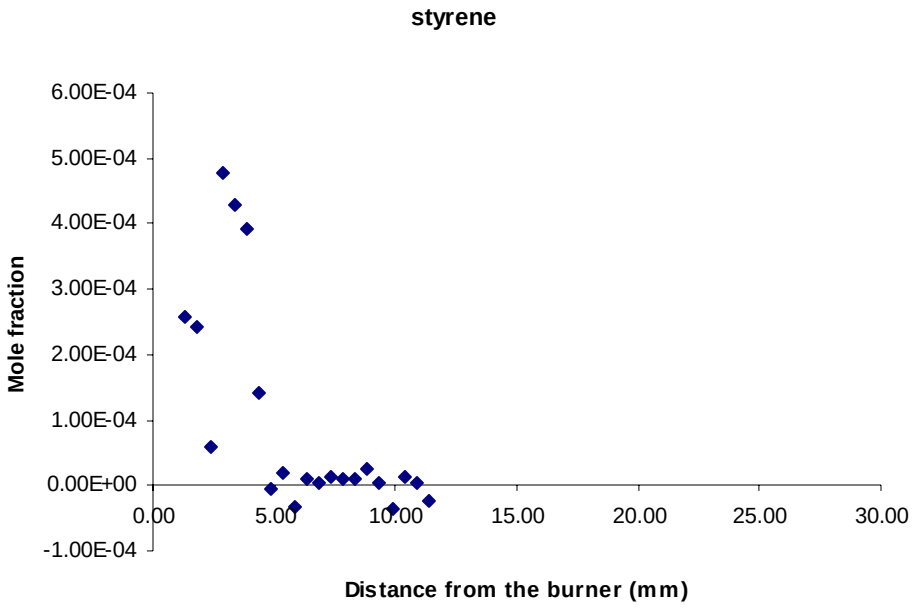

Figure 3.69. Mole fraction profile of styrene in the fuel-lean toluene flame.

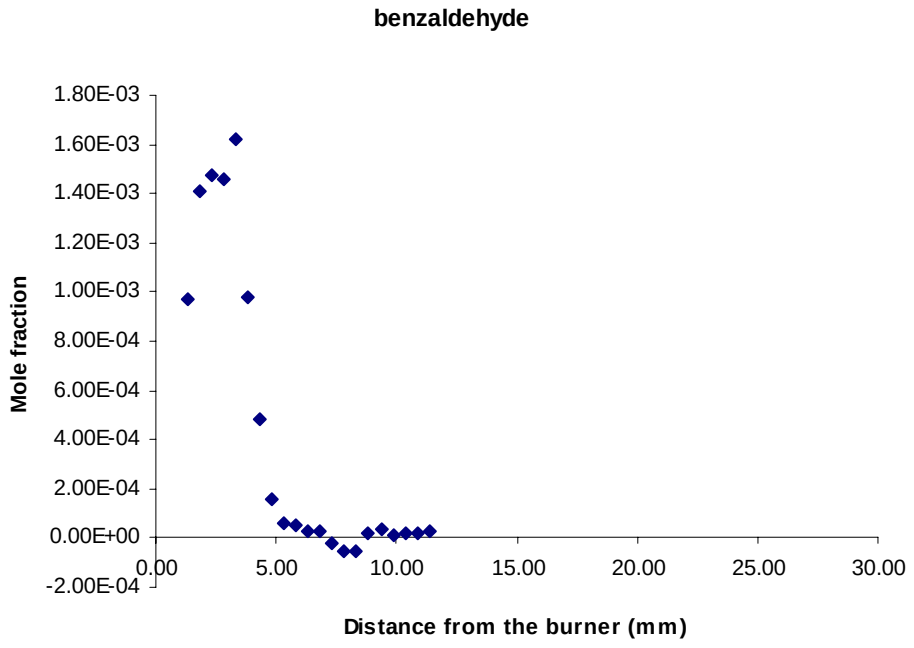

Figure 3.70. Mole fraction profile of benzaldehyde in the fuel-lean toluene flame.

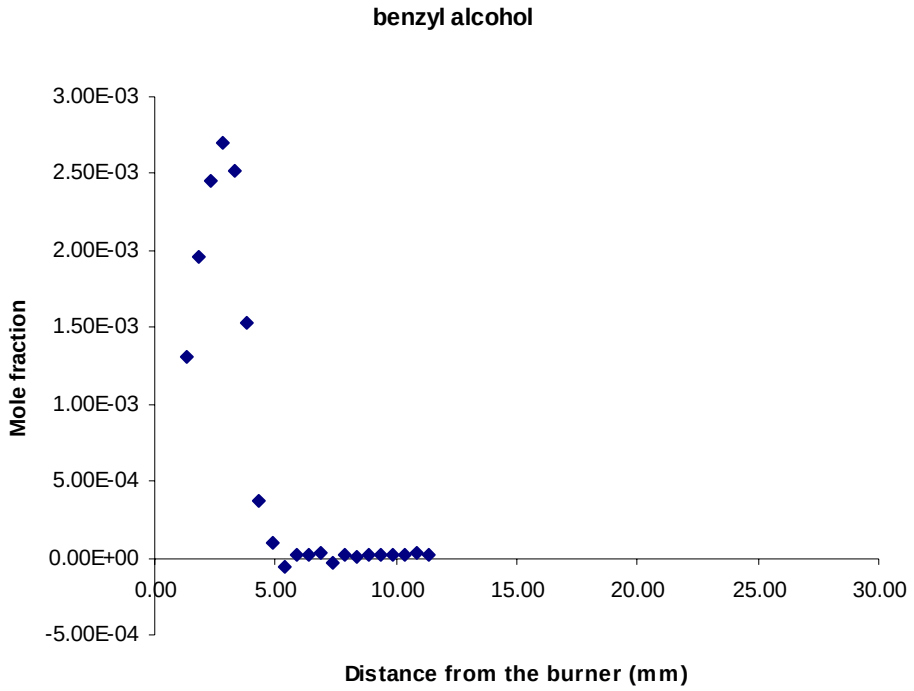

Figure 3.71. Mole fraction profile of benzyl alcohol in the fuel-lean toluene flame.

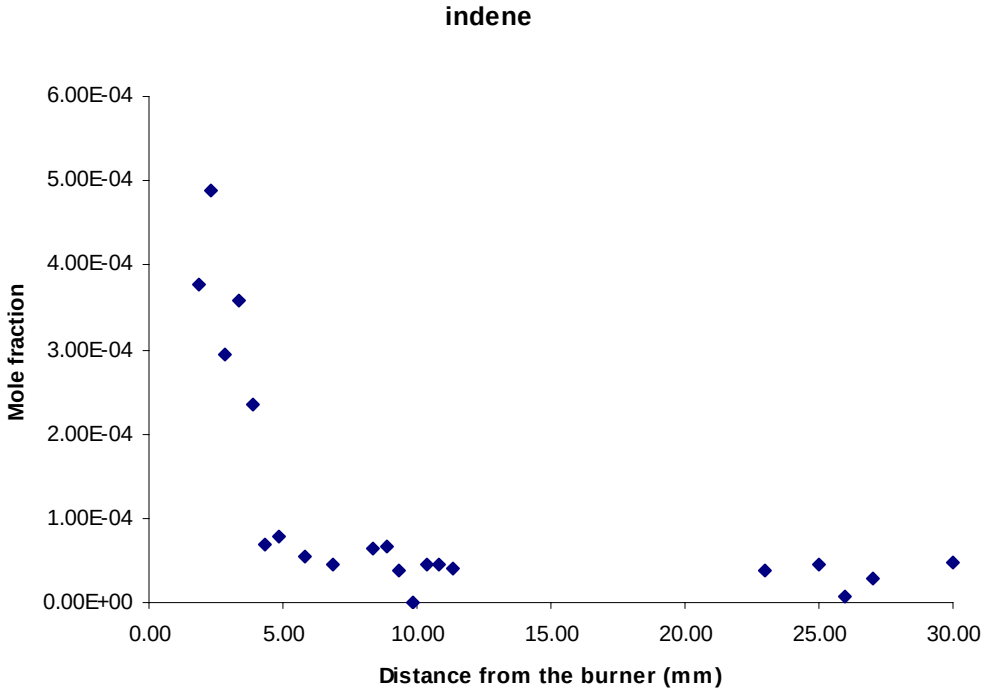

Figure 3.72. Mole fraction profile of indene in the fuel-lean toluene flame.

Mass 1. The mass 1 species was not detected in the energy scan range of 8 to 11.155 eV. The species showed up at 14.37 eV burner scan. It was identified as hydrogen atom. The hydrogen atom mole-fraction profile is depicted in Figure 3.40. It shows an increase in hydrogen atom mole fraction away from the burner up to the post-flame zone. In the post-flame zone, the mole fraction reaches 0.349% of the post-flame gases.

Mass 2. As discussed in section 3.2.1, the mass 2 species was identified as molecular hydrogen. The hydrogen mole-fraction profile is depicted in Figure 3.41. Hydrogen mole fraction increases steadily away from the burner to about 3.87 mm, and then decreases to 9.82 mm from the burner, and then remains almost constant throughout the post-flame gases.

Mass 15. The mass 15 species was identified as methyl (CH_3) radical, as discussed in section 3.2.1. The mole-fraction profile is reported in Figure 3.42. It shows a peak in methyl radical mole fraction at 3.35 mm from the burner, falling to almost zero at 6.85 mm away from the burner.

Mass 16. The mass 16 signal was identified as methane (CH_4) and O. Neither species was detected in the energy scan as their respective ionization energies are higher than 11.5 eV. A 13.22 eV burner scan was used to obtain the methane mole-fraction profile (Figure 3.43). The mole-fraction profile shows a peak at 2.85 mm from the burner. A burner scan of mass 16 species at 14.37 shows that another species is present at that energy. This second species was identified as atomic oxygen. CH_4 signal was extrapolated from 13.22 eV energy to 14.37 eV and then subtracted from the total mass 16 signal. The subtracted signal was treated as being from the atomic oxygen. The

oxygen mole-fraction profile is depicted in Figure 3.44. It shows a scattered signal, but an overall gradual increase in oxygen mole fraction away from the burner is observed.

Mass 17. The mass 17 signal was treated as hydroxyl radical (OH). The mole-fraction profile shows a gradual increase to about 7.35 mm from the burner and then fluctuates a little towards the end of the post-flame zone. Figure 3.45 depicts the OH mole-fraction profile.

Mass 18. The mass 18 signal was identified as water. The mole-fraction profile of water is given in Figure 3.39.

Mass 26. The mass 26 species was identified as acetylene (C_2H_2), following the same principles as discussed in section 3.2.1. The mole-fraction profile of C_2H_2 is depicted in Figure 3.46. The profile shows a peak at 4.35 mm from the burner.

Mass 28. As discussed in the previous section, the mass 28 species found in the lean-toluene flame were identified as carbon monoxide (CO) and ethylene (C_2H_4). A peak for the C_2H_4 signal is observed at 2.85 mm from the burner. The CO mole fraction shows a peak at 5.35 mm from the burner. Figure 3.39 shows the CO mole fraction, and Figure 3.47 shows the C_2H_4 mole-fraction profile.

Mass 30. The mass 30 species was identified as formaldehyde (HCHO). Figure 3.48 depicts its mole-fraction profile. The profile shows a peak at 3.35 mm away from the burner.

Mass 32. The mass 32 species was identified as molecular oxygen (O_2). Figure 3.39 depicts its mole-fraction profile along with other major species. The oxygen profile shows a sharp decrease in oxygen mole fraction to 6.35 mm from the burner, and then it

shows a gradual decrease up to 11.35 mm from the burner. After that, it did not change much throughout the post-flame zone.

Mass 39. The mass 39 species was identified as propargyl (C_3H_3). Figure 3.49 depicts its mole-fraction profile. The propargyl profile shows a peak at 4.35 mm from the burner.

Mass 40. The mass 40 signal in the toluene flame consists of allene, propyne and argon. These species were resolved following the same procedure described in section 3.2.1. Figure 3.39 shows the mole-fraction profile for argon along with other major species in the flame. The argon mole-fraction profile shows a decrease to 5.35 mm away from the burner and then it remained steady. Figure 3.50 shows the mole-fraction profiles for allene and propyne.

Mass 42. The mass 42 species was identified as ketene (C_2H_2O). Its mole-fraction profile is depicted in Figure 3.51.A burner scan at 10.06 eV is used to get its mole-fraction profile. The profile shows a peak at 3.35 mm from the burner.

Mass 44. The mass 44 species was identified as carbon dioxide (CO_2). Although CO_2 did not show up in the energy scan (8 to 11.5 eV) as it has a higher ionization energy, but the mass 44 signal that is detected in 14.37 eV is considered as CO_2. Its profile is shown in Figure 3.39 along with other major species.

Mass 50. The mass 50 species was identified as 1,3-butadiyne or diacetylene. Figure 3.52 depicts its mole-fraction profile. The profile shows a peak at 4.35 mm from the burner.

Mass 52. The mass 52 species was identified as 1-buten-3-yne or vinylacetylene. Figure 3.53 depicts its mole-fraction profile. The profile shows a peak at 3.87 mm from the burner.

Mass 54. The mass 54 species was identified as 1,3-butadiene. Figure 3.54 depicts its mole-fraction profile. The profile shows a peak at 3.87 mm from the burner.

Mass 56. The mass 56 species was proposed to be methoxyacetylene. Its mole-fraction profile is depicted in Figure 3.55. The profile shows a peak at 2.35 mm from the burner.

Mass 64. The mass 64 species was identified as 1,3-pentadiyne (C_5H_4). Figure 3.56 depicts its mole-fraction profile. The profile shows a peak at 4.35 mm from the burner.

Mass 65. The mass 65 species was identified as cyclopentadienyl radical (C_5H_5). Figure 3.57 depicts its mole-fraction profile. The profile shows a peak at 3.87 mm from the burner.

Mass 66. The mass 66 species was identified as 1,3-cyclopentadiene (C_5H_6). Figure 3.58 depicts its mole-fraction profile. The profile shows a peak at 3.35 mm from the burner.

Mass 68. The mass 68 species was identified as 1,2-butadienone. Figure 3.59 depicts its mole-fraction profile. The profile shows a peak at 2.85 mm -from the burner.

Mass 74. The mass 74 species was identified as 1,3,5-hexatriyne or triacetylene (C_6H_2). Figure 3.60 depicts its mole-fraction profile. The profile shows a peak at 4.35 mm -from the burner.

Mass 76. The mass 76 species was identified as benzyne (C_6H_4). Figure 3.61 depicts its mole-fraction profile. The profile shows a peak at 4.35 mm from the burner.

Mass 78. From the PIE scan of mass 78, benzene and fulvene were identified. It seems that there is another species 1,5-hexadien-3-yne (I.E. 8.5 eV) at mass 78. From the PIE scan, however, it is evident that benzene is the dominant species as mass 78. Hence the total mass 78 signal is to be all benzene, and its mole fraction is obtained. Figure 3.62 depicts the benzene mole-fraction profile. It shows a peak at 3.35 mm from the burner.

Mass 80. The mass 80 species was identified as methylcyclopentadiene (C_6H_8). Figure 3.63 depicts its mole-fraction profile. A burner scan at 10.06 eV is used to get its mole-fraction profile. The profile shows a peak at 3.35 mm from the burner.

Mass 82. The mass 82 species was identified as 1,2-butadienone-3-methyl. Figure 3.64 depicts its mole-fraction profile. The profile shows a peak at 1.85 mm from the burner.

Mass 90. The mass 90 species was identified as 1,3-cyclopentadiene-5-ethenylidene. Figure 3.65 depicts its mole-fraction profile. The profile shows a peak at 3.87 mm from the burner.

Mass 91. The mass 91 species was identified as benzyl radical. Figure 3.66 depicts its mole-fraction profile. The profile shows a peak at 3.35 mm.

Mass 92. The mass 92 species was identified as toluene (C_7H_8).This is the fuel in the flame. Figure 3.39 depicts its mole-fraction profile. It shows that all the toluene is oxidized within 3.87 mm.

Mass 94. The mass 94 species was identified as phenol (C_6H_6O). Figure 3.67 depicts its mole-fraction profile. It shows a peak at 3.35 mm.

Mass 102. The mass 102 species was identified as phenylacetylene (C_8H_6). Figure 3.68 depicts its mole-fraction profile. It shows a peak at 4.35 mm.

Mass 104. The mass 104 species was identified as styrene (C_8H_8). Figure 3.69 depicts its mole-fraction profile. It showed a peak at 2.85 mm.

Mass 106. The mass 106 species was identified as benzaldehyde (C_7H_6O). Figure 3.70 depicts its mole-fraction profile. At 3.35 mm, it forms a peak.

Mass 108. The mass 108 species was identified as benzyl alcohol (C_7H_8O). Figure 3.71 depicts its mole-fraction profile. At 2.85 mm, it forms a peak.

Mass 116. The mass 116 species was identified as indene (C_9H_8). Figure 3.72 depicts its mole-fraction profile. At 2.35 mm, it forms a peak.

3.3.2 Check for mole-fraction-profile analysis

The mole-fraction profile obtained from the flame data is checked with the initial feed composition and a mole balance is performed with hydrogen and carbon atom balance in the feed and the post-flame zone of the flame.

Initial mole fraction of the feed gas going into the burner is obtained from the feed conditions of the toluene flame. This result is then compared against the mole fraction achieved for the first data point away from the burner. The comparison is tabulated in Table 3.6.

Table 3.6. Comparison of mole fraction of the feed composition to mole fraction at first data point away from the burner.

	Mole fraction in the feed gas	Mole fraction at 1.35 mm away from the burner
Toluene	0.045	0.0353
Oxygen	0.455	0.303
Argon	0.5	0.525

The toluene and oxygen mole fractions at the first data point show a decrease from their feed mole fractions. The argon mole fraction shows a slight increase. Toluene and oxygen mole fractions were expected to show a decrease. With the cyclohexane data analysis, it was found that the argon mole fraction also showed a decrease. In this flame, a slight increase occurs in the argon mole fraction, although the initial argon mole fraction obtained was very close to the feed condition. Therefore, the initial check for mole fraction analysis was satisfactory.

The carbon and hydrogen atom balance performed on the lean toluene data show that the both the carbon and hydrogen balances in the post flame zone overshoot the number of moles in the carbon atoms and the number of mole of hydrogen atoms in the feed. This comparison suggests that the background correction for the flame needs to be adjusted. The mismatch also might be due to the wrong values of OH, H and O. The profiles for these species need to be obtained with the UMass apparatus and included into the data analysis.

3.4 Toluene flame (Φ = 1.497) data analysis

The fuel-rich toluene flame feed conditions are tabulated in Table 3.4.

Table 3.7 Condition for the fuel-rich toluene flame

	Flow Rates	Pressure in the reaction chamber	Fuel equivalence ratio (Φ)
Toluene	1.2 ml/min	30 torr	1.497
Oxygen	1.516 SLM		
Argon	1 SLM		

The species identified in the toluene flame were reported in Table 3.8. The description of the mole-fraction profiles of these species follows below. An 8.5 to 11.0 eV energy scan was used to identify the species in the toluene flame.

Table 3.8. List of species measured in the fuel-rich toluene flame, ionization energies of the species as reported in (NIST Chemistry WebBook), ionization energy observed, and ionization energy used to measure the profile.

AMU	Species Identified	Ionization energy from literature (eV)	Ionization energy observed (eV)	Burner scan Energy (eV)
1	H	13.59844	-	14.35
2	H_2	15.42593±0.00005	-	16.22
15	Methyl (CH_3) radical	9.84±0.01	9.775	9.98
16	Methane (CH_4)	12.61±0.01	-	13.20
16	Oxygen atom (O)	13.61806	-	14.35
17	Hydroxyl radical (OH)	13.017±0.002	-	13.20
18	Water (H_2O)	12.621 ±0.002	-	13.20
26	Acetylene (C_2H_2)	11.4±0.002	-	12.30
28	Ethylene (C_2H_4)	10.5138±0.0006	10.5138	12.30
28	Carbon monoxide (CO)	14.014±0.0003	-	14.35
30	Formaldehyde (HCHO)	10.88±0.01	10.875	11.52
32	Oxygen (O_2)	12.0697±0.0002	-	12.30
39	Propargyl (C_3H_3) radical	8.67±0.02	8.675	9.98
40	Allene (C_3H_4)	9.692±0.004	9.675	9.98
40	Propyne (C_3H_4)	10.36±0.01	10.325	10.52
40	Argon (Ar)	15.759±0.001	-	16.22
42	Ketene(C_2H_2O)	9.617±0.003	9.625	11.52
42	Propene (C_3H_6)	9.73 ± 0.01	9.725	-
44	Carbon dioxide (CO_2)	13.797±0.001	-	14.35
50	1,3-Butadiyne (C_4H_2)	10.17	10.125	10.52
52	1-Buten-3-yne (C_4H_4)	9.58±0.02	9.575	9.98
54	1,3-Butadiene (C_4H_6)	9.072±0.007	9.075	9.98
56	Methoxyacetylene (C_3H_4O)	9.48	9.525	9.98
64	1,3-Pentadiyne (C_5H_4)	9.5 ± 0.02	9.5	9.98
65	Cyclopentadienyl (C_5H_5) radical	8.41/8.56	Below 8.5	9.98
66	1,3-Cyclopentadiene (C_5H_6)	8.57 ± 0.01	8.575	9.98

AMU	Species Identified	Ionization energy from literature (eV)	Ionization energy observed (eV)	Burner scan Energy (eV)
68	Cyclopentene (C_5H_8)	9.01 ± 0.01	Near 9	9.98
74	1,3,5-Hexatriyne (C_6H_2)	9.5±0.02	9.475	9.98
76	Unknown	-	8.575	-
76	Benzyne (C_6H_4)	9.03±0.05	9.03	9.98
78	Fulvene (C_6H_6)	8.36	Below 8.5	
78	Benzene (C_6H_6)	9.24378±0.00007	9.215	9.98
80	Methylcyclopentadiene (C_6H_8)	8.28±0.05	Below 8.5	9.98
82	1,2-Butadienone,3-methyl (C_5H_6O)	8.65	8.63	9.98
90	1,3-Cyclopentadiene,5-ethenylidene (C_7H_6)	8.29	Below 8.5	9.98
91	Benzyl radical (C_7H_7)	7.242±0.006	Below 8	9.98
92	Toluene (C_7H_8)	8.828±0.001	8.825	9.98
94	Phenol (C_6H_6O)	8.49±0.02	Slightly below 8.5	9.98
102	Phenylacetylene (C_8H_6)	8.82±0.02	8.775	9.98
104	Styrene (C_8H_8)	8.464±0.001	Slightly below 8.5	9.98
106	Paraxylene (C_8H_{10})	8.44±0.05	8.375	9.98
106	Benzaldehyde (C_7H_6O)	9.5±0.08	9.48	9.98
108	Benzyl alcohol (C_7H_8O)	8.26±0.05	Below 8.5	9.98
115	Indenyl radical (C_9H_7)	8.35	Below 8.5	9.98
116	Indene (C_9H_8)	8.14±0.01	8.13	9.98
118	Indane (C_9H_{10})	8.6 ± 0.1	8.625	9.98
120	1-Phenylethenol (C_8H_8O)	8.01 ± 0.03	Below 8.5	9.98
122	Phenol , 4-ethyl ($C_8H_{10}O$)	7.84	Below 8.5	9.98
126	1,4-Diethynylbenzene ($C_{10}H_6$)	8.58 ± 0.02	Near 8.5	9.98
128	Naphthalene ($C_{10}H_8$)	8.144 ± 0.001	-	9.98
130	Methyl Indene ($C_{10}H_{10}$)	-	-	9.98
132	C_9H_8O	-	-	9.98
140	1H-Indene,2-ethynyl ($C_{11}H_8$)	8.04	-	9.98

AMU	Species Identified	Ionization energy from literature (eV)	Ionization energy observed (eV)	Burner scan Energy (eV)
142	Naphthalene,1-methyl ($C_{11}H_{10}$)	7.96 ± 0.03	-	9.98
144	$C_{10}H_8O$	-	8.575	9.98
152	Acenaphthylene ($C_{12}H_8$)	8.12± 0.1	-	9.98
154	$C_{12}H_{10}$	-	-	9.98
156	($C_{12}H_{12}$)	-	-	9.98
166	($C_{13}H_{10}$)	-	-	9.98
168	($C_{13}H_{12}$)	-	-	9.98
180	$C_{14}H_{12}$	-	-	9.98
182	$C_{14}H_{14}$	-	-	9.98
184	$C_{14}H_{16}$	-	-	9.98

3.4.1 Mole-fraction profiles.

The mole-fraction profiles of the species identified are given below.

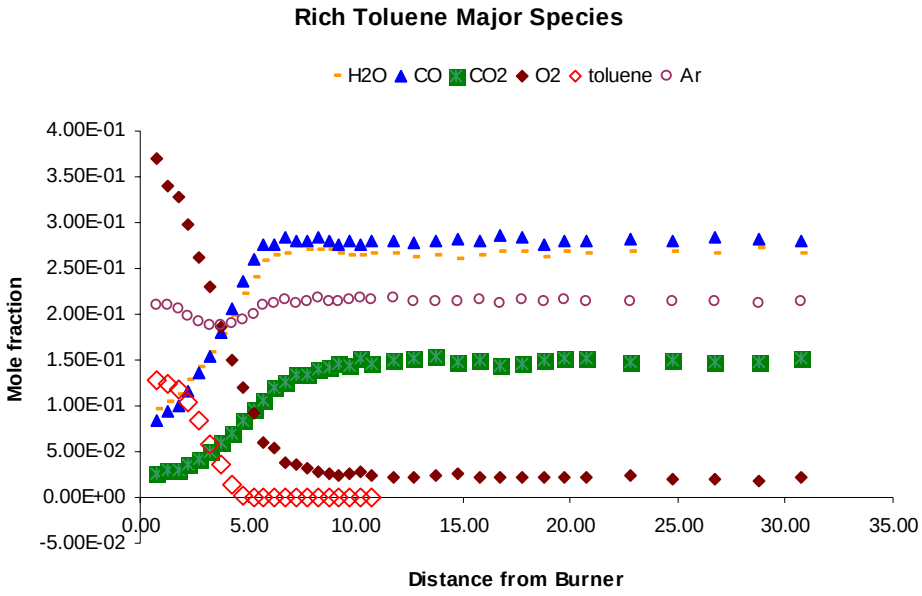

Figure 3.73. Mole-fraction profiles of major species in the fuel-rich toluene flame.

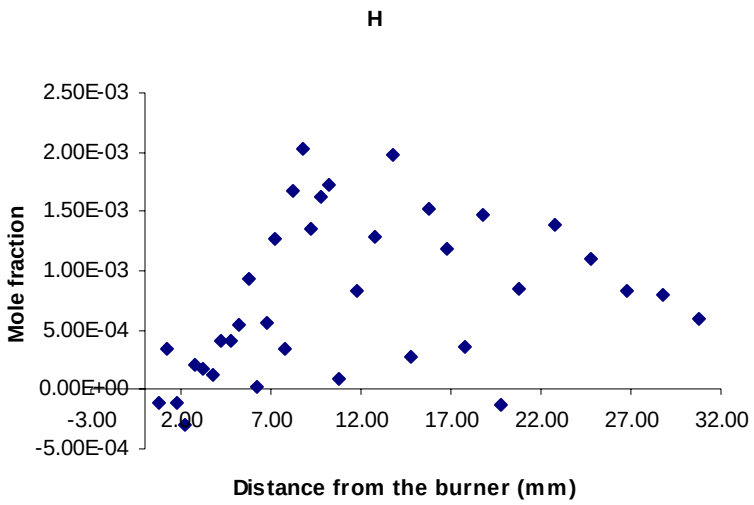

Figure 3.74. Mole-fraction profile of H atom in the fuel-rich toluene flame.

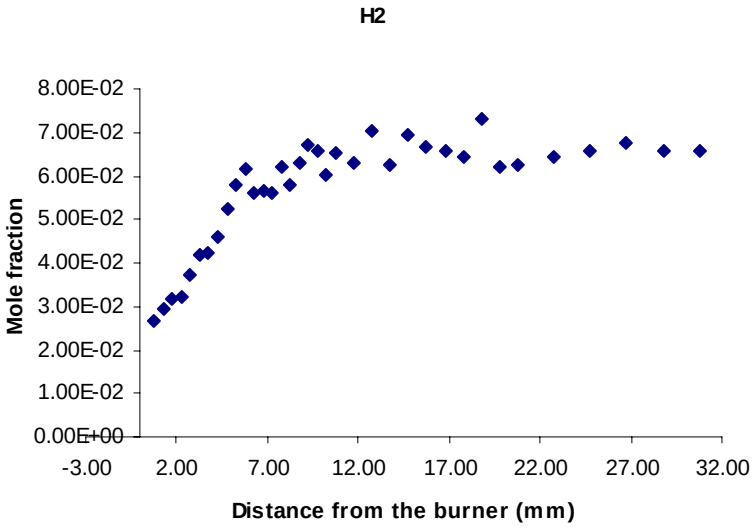

Figure 3.75. Mole-fraction profile of H_2 in the fuel-rich toluene flame.

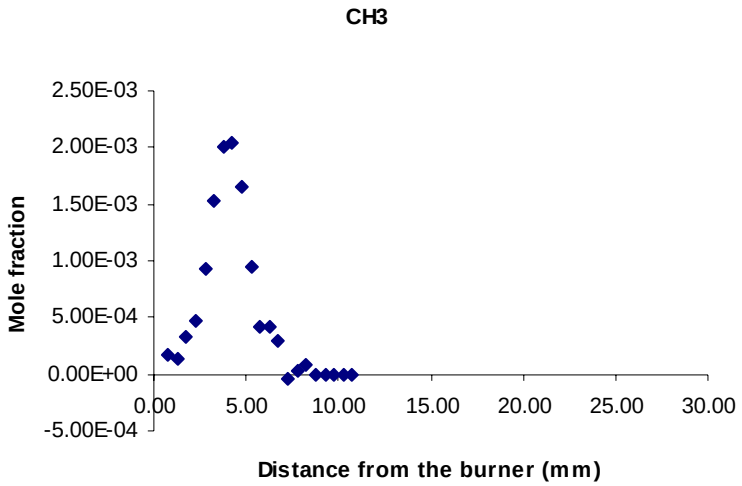

Figure 3.76. Mole-fraction profile of CH_3 radical in the fuel-rich toluene flame.

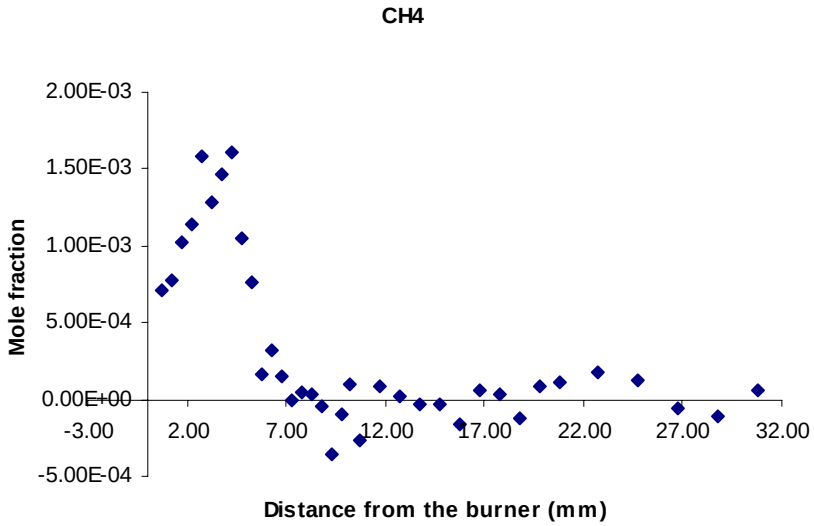

Figure 3.77. Mole-fraction profile of CH_4 in the fuel-rich toluene flame.

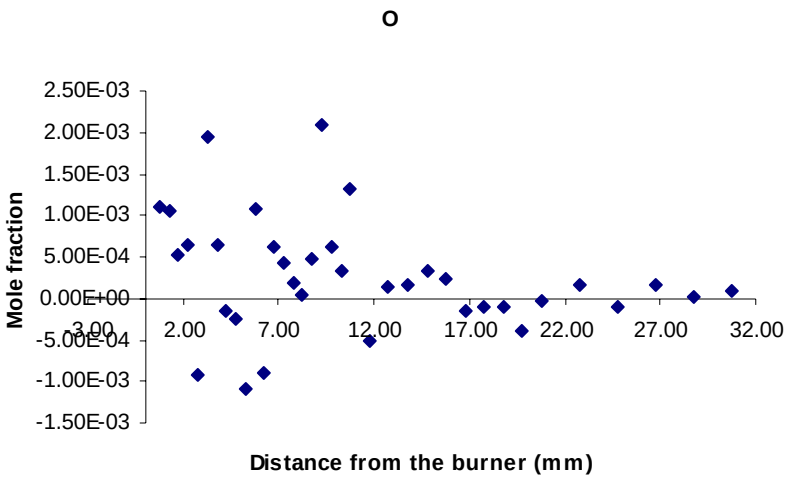

Figure 3.78. Mole-fraction profile of O in the fuel-rich toluene flame.

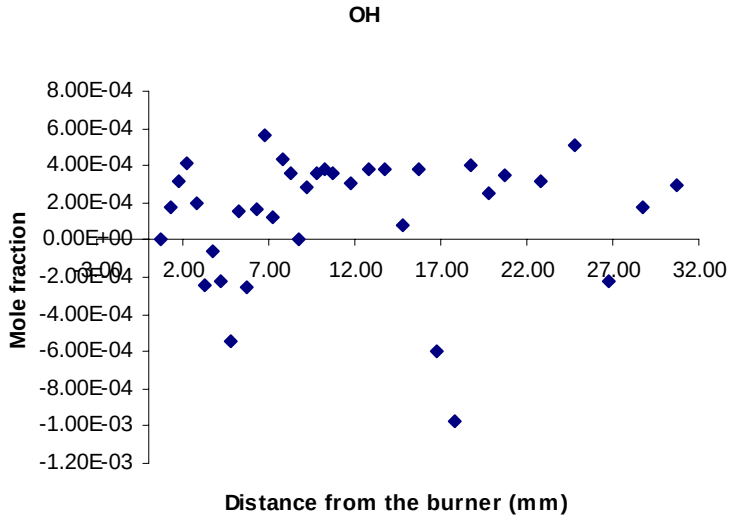

Figure 3.79. Mole-fraction profile of OH in the fuel-rich toluene flame.

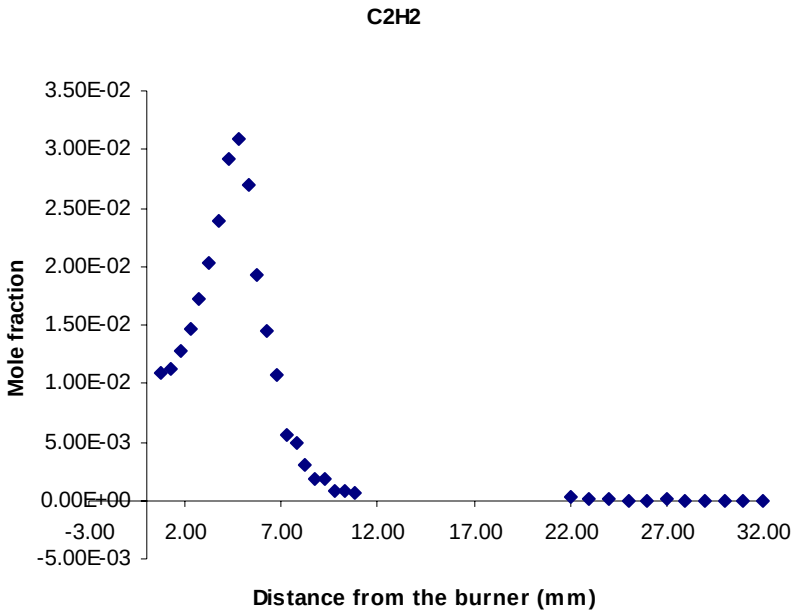

Figure 3.80. Mole-fraction profile of acetylene (C_2H_2) in the fuel-rich toluene flame.

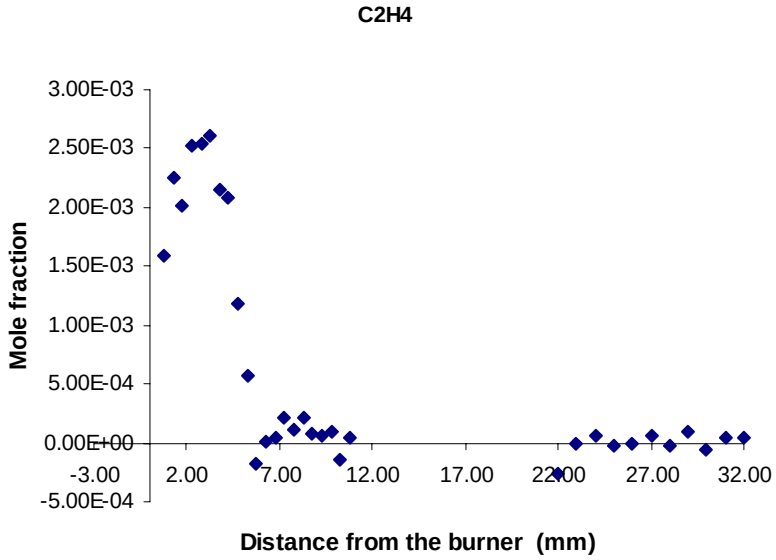

Figure 3.81. Mole-fraction profile of ethylene (C_2H_4) in the fuel-rich toluene flame.

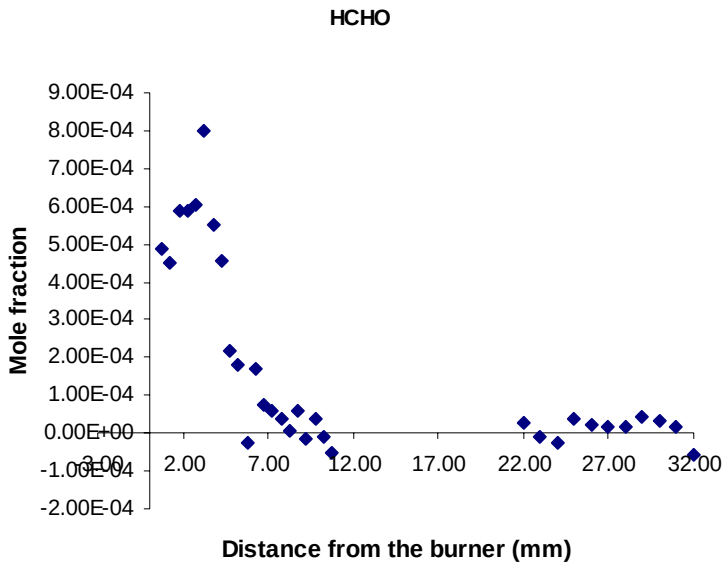

Figure 3.82. Mole-fraction profile of HCHO in the fuel-rich toluene flame.

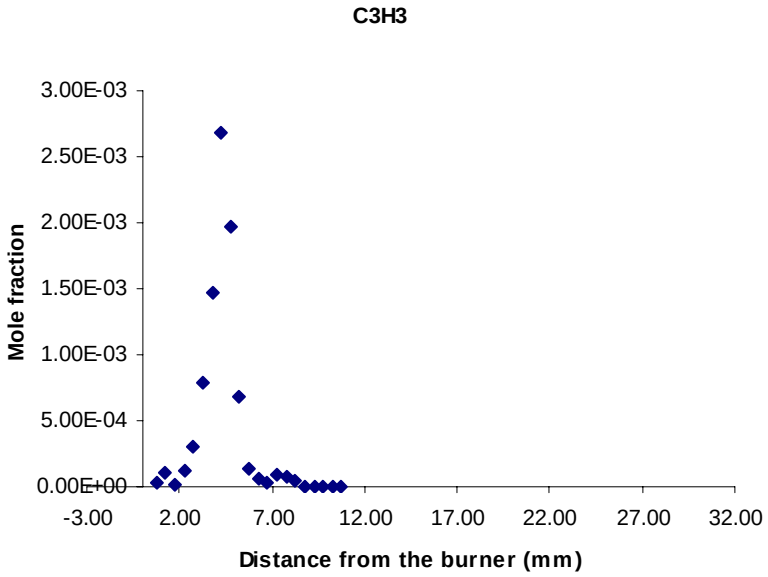

Figure 3.83. Mole-fraction profile of C_3H_3 in the fuel-rich toluene flame.

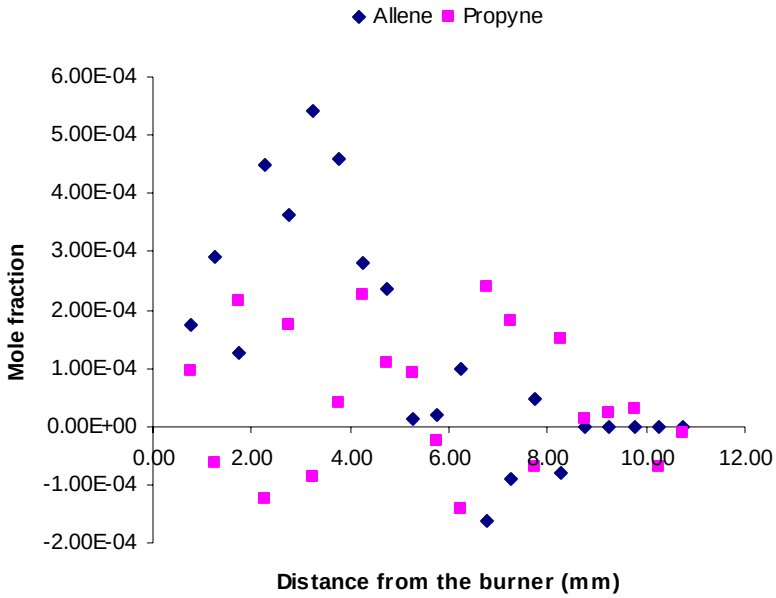

Figure 3.84. Mole-fraction profiles of allene and propyne in the fuel-rich toluene flame.

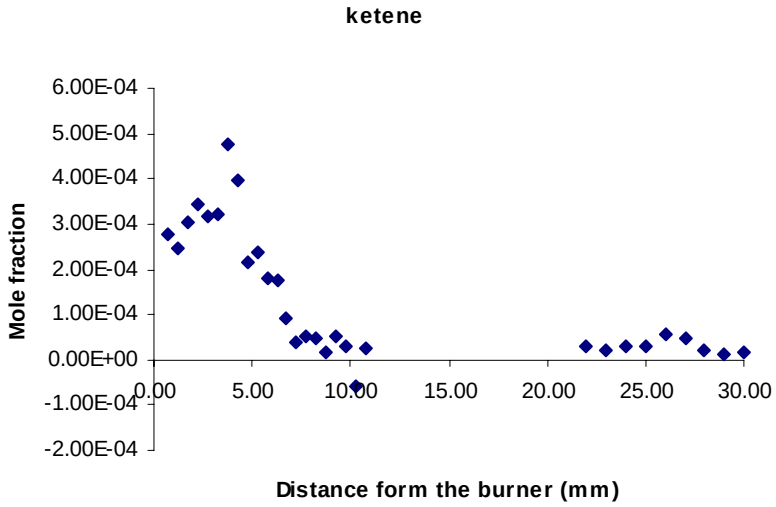

Figure 3.85. Mole-fraction profile of ketene in the fuel-rich toluene flame.

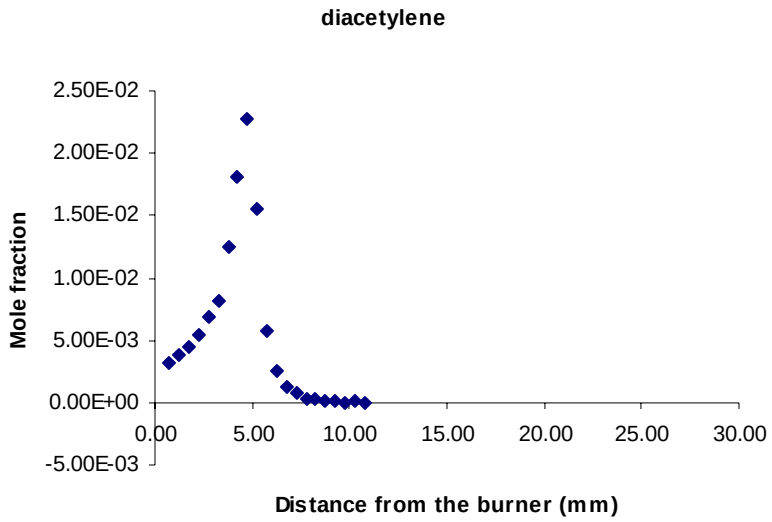

Figure 3.86. Mole-fraction profile of diacetylene in the fuel-rich toluene flame.

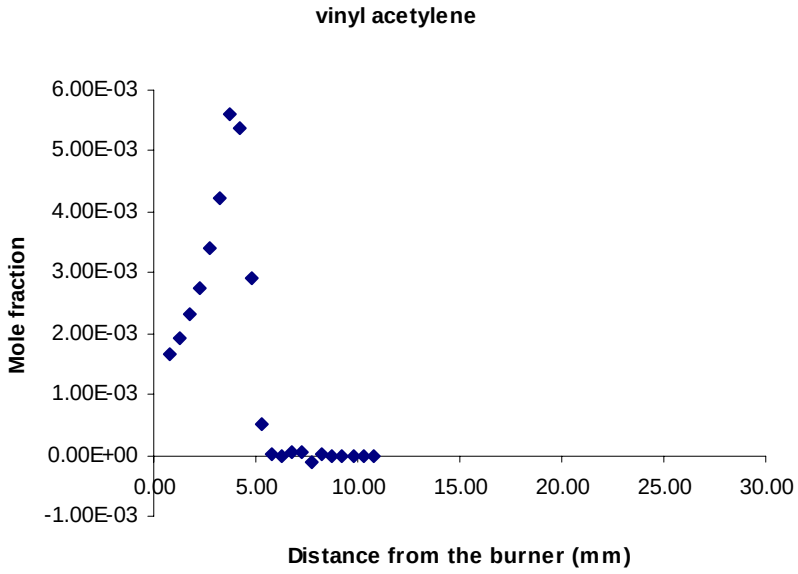

Figure 3.87. Mole-fraction profile of vinylacetylene in the fuel-rich toluene flame.

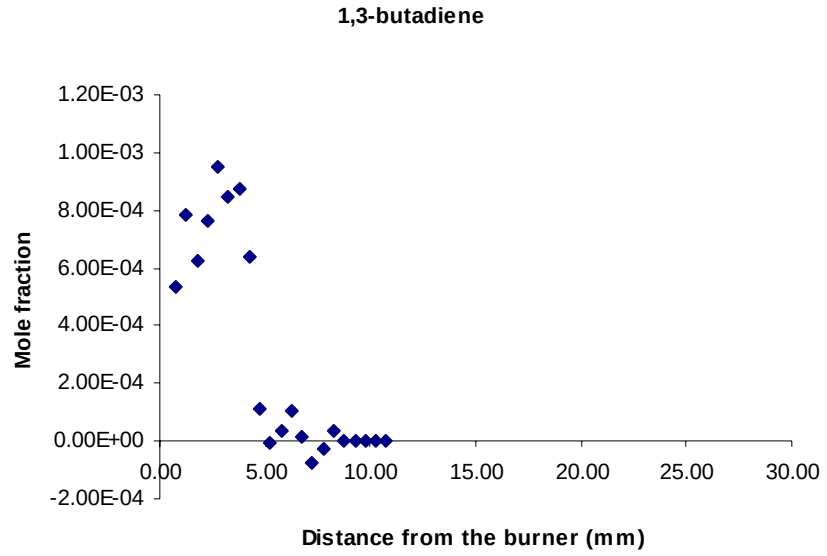

Figure 3.88. Mole-fraction profile of 1,3-butadiene in the fuel-rich toluene flame.

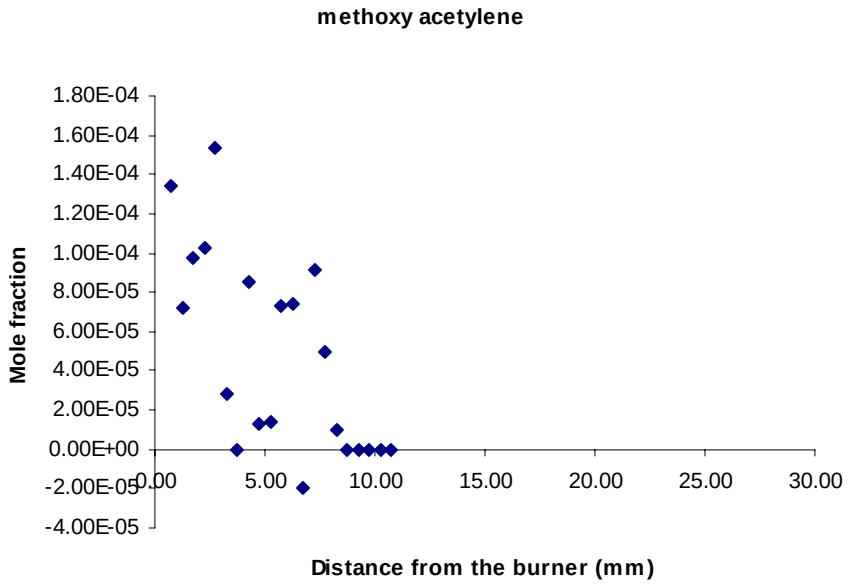

Figure 3.89. Mole-fraction profile of methoxyacetylene in the fuel-rich toluene flame.

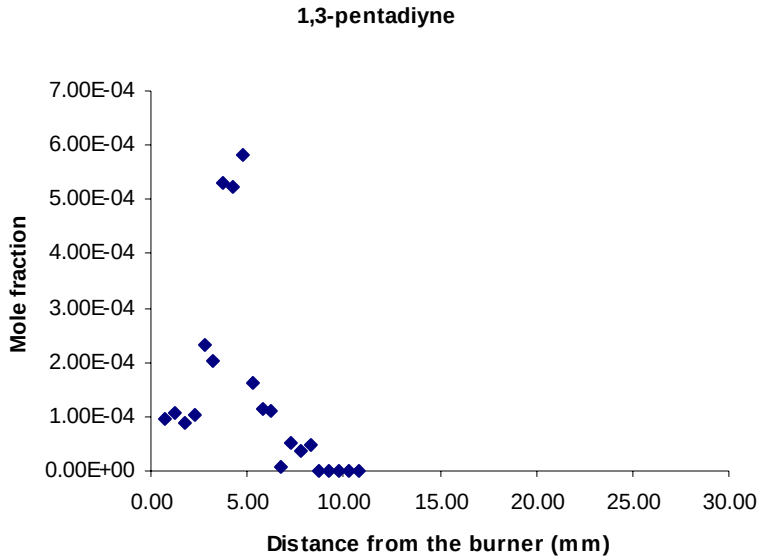

Figure 3.90. Mole-fraction profile of 1,3-pentadiyne in the fuel-rich toluene flame.

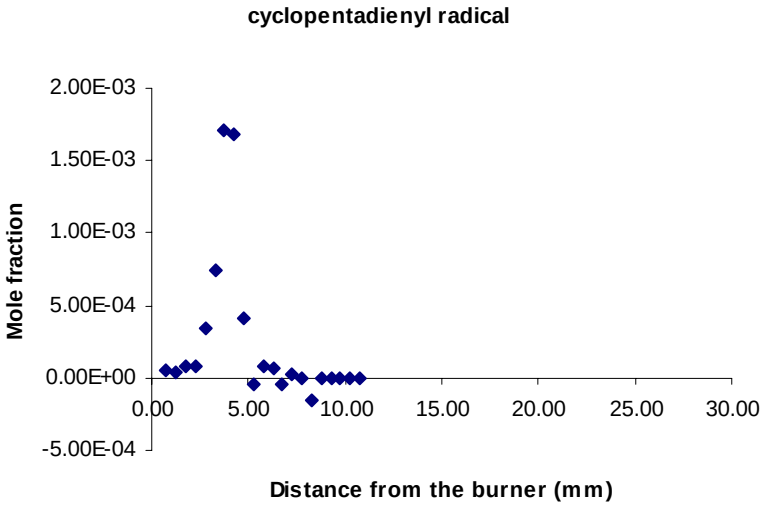

Figure 3.91. Mole-fraction profile of cyclopentadienyl radical in the fuel-rich toluene flame.

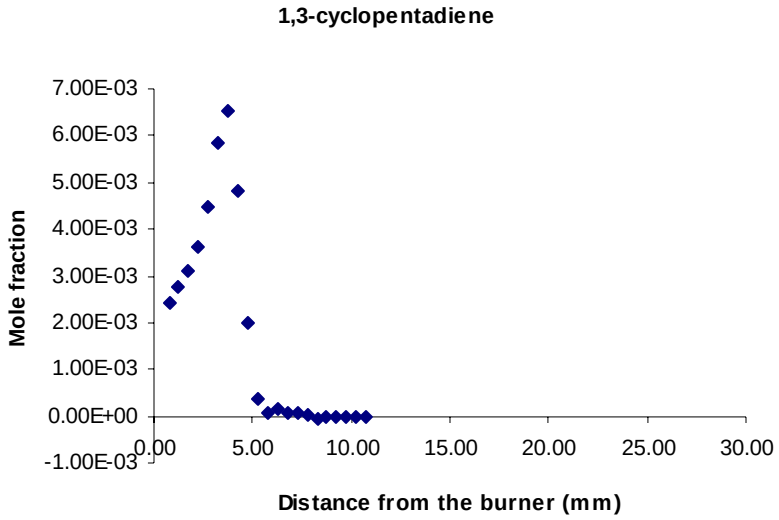

Figure 3.92. Mole-fraction profile of 1,3-cyclopentadiene in the fuel-rich toluene.

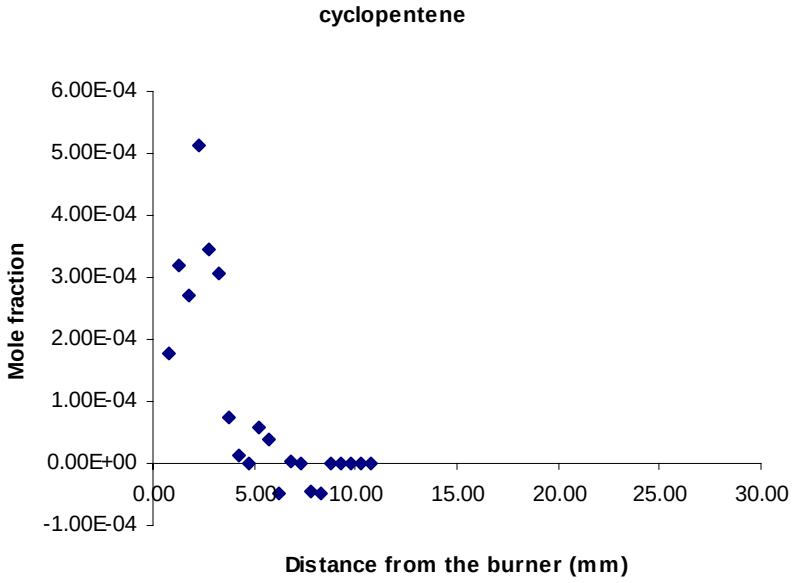

Figure 3.93. Mole-fraction profile of cyclopentene in the fuel-rich toluene flame.

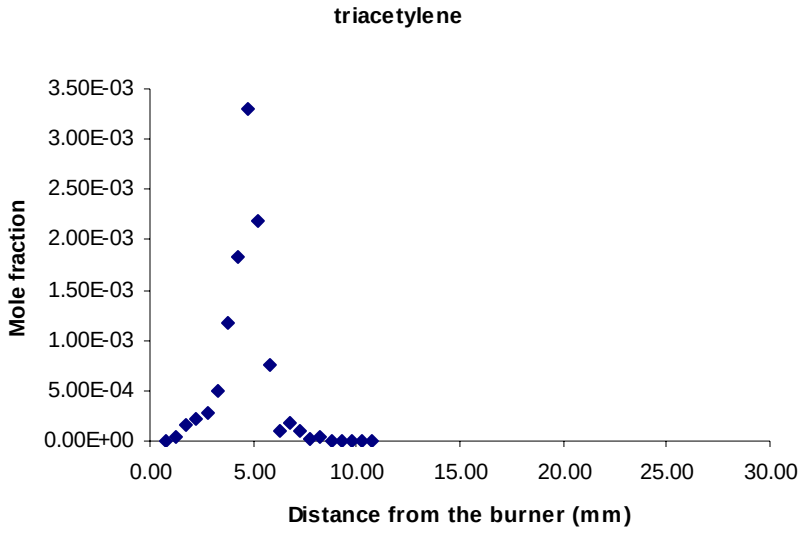

Figure 3.94. Mole-fraction profile of triacetylene in the fuel-rich toluene flame.

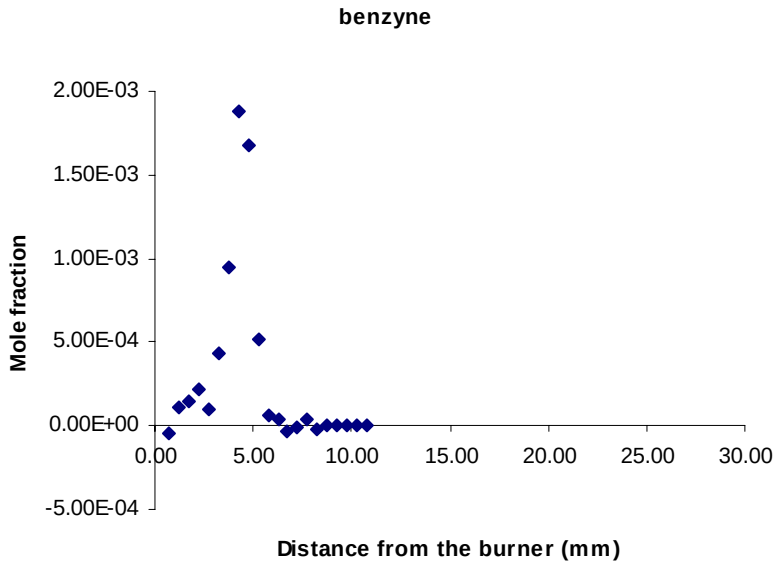

Figure 3.95. Mole-fraction profile of benzyne in the fuel-rich toluene flame.

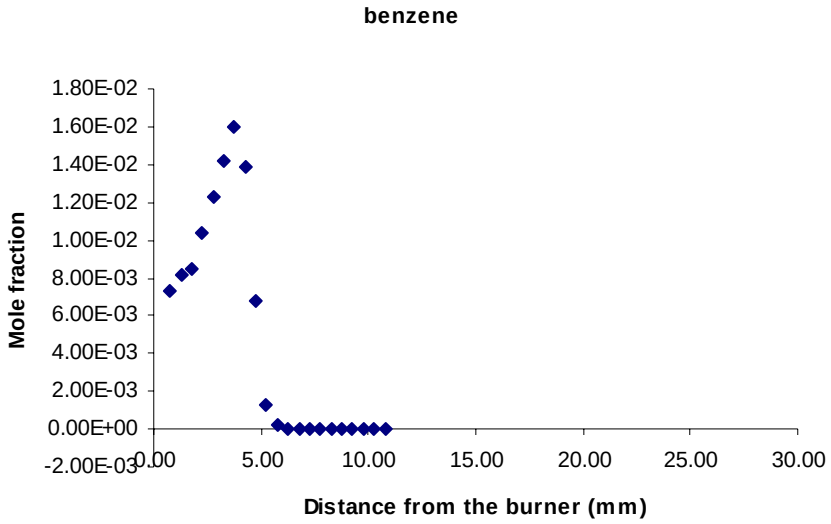

Figure 3.96. Mole-fraction profile of benzene in the fuel-rich toluene flame.

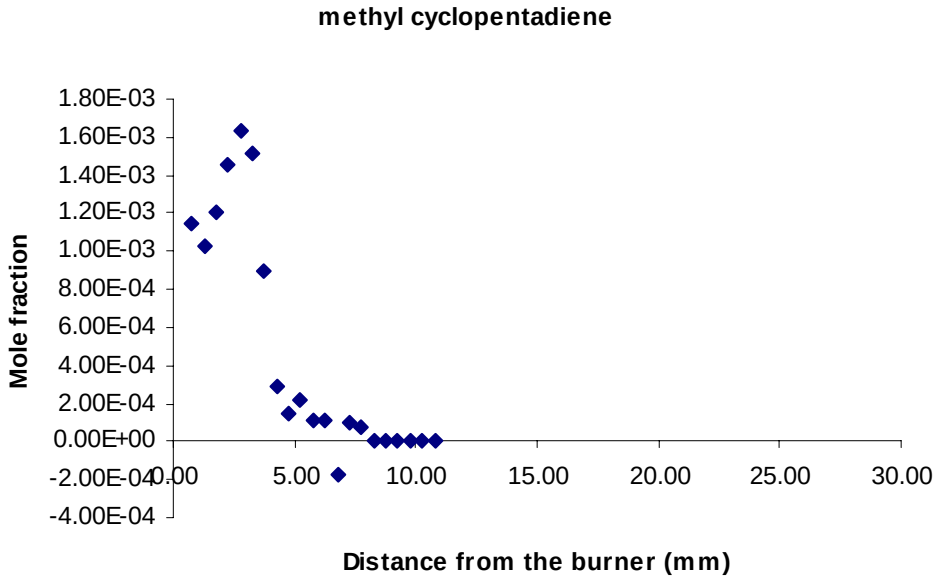

Figure 3.97. Mole-fraction profile of methyl cyclopentadiene in the fuel-rich toluene flame.

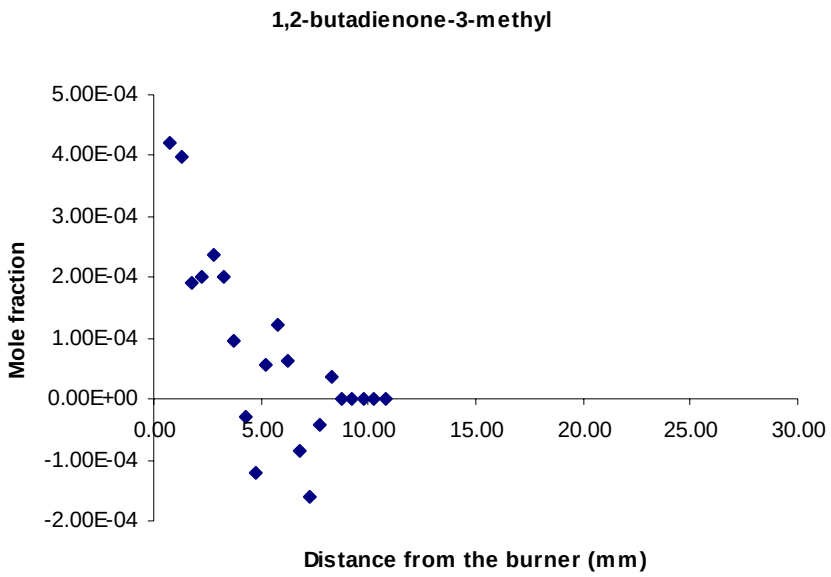

Figure 3.98. Mole-fraction profile of 1,2-butadienone-3-methyl in the fuel-rich toluene flame.

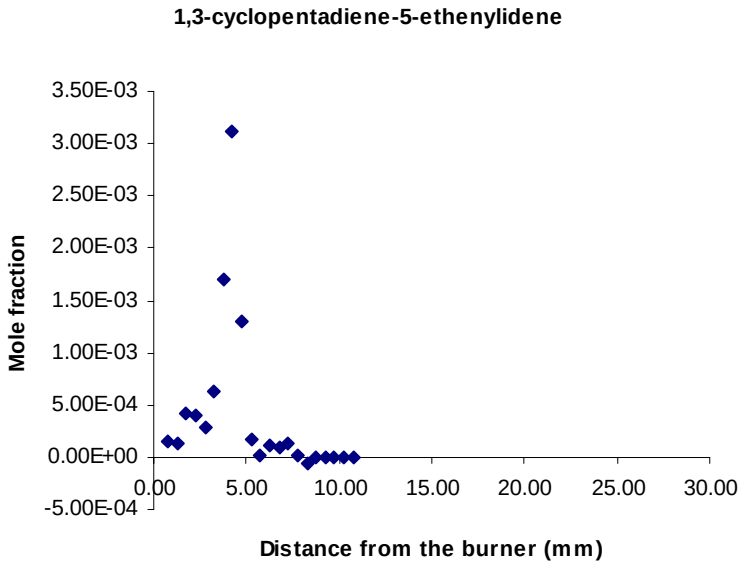

Figure 3.99. Mole-fraction profile of 1,3-cyclopentadiene-5-ethenylidene in the fuel-rich toluene flame.

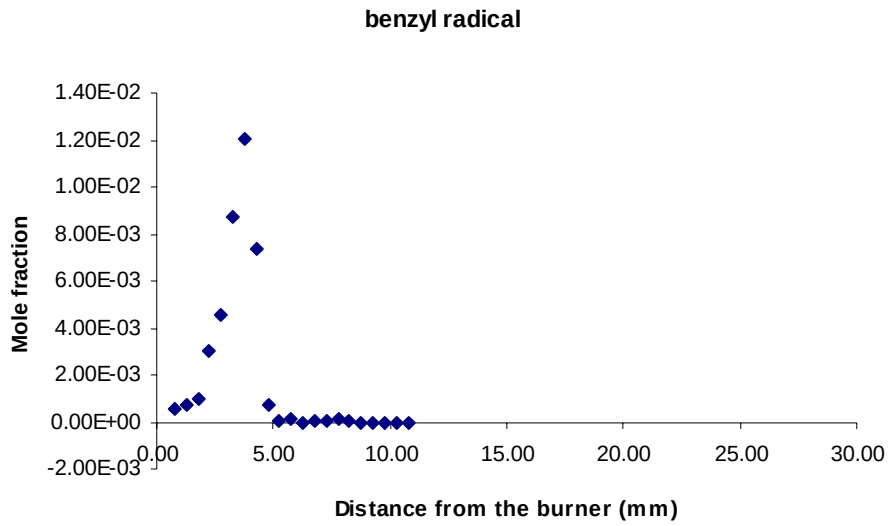

Figure 3.100. Mole-fraction profile of benzyl radical in the fuel-rich toluene flame.

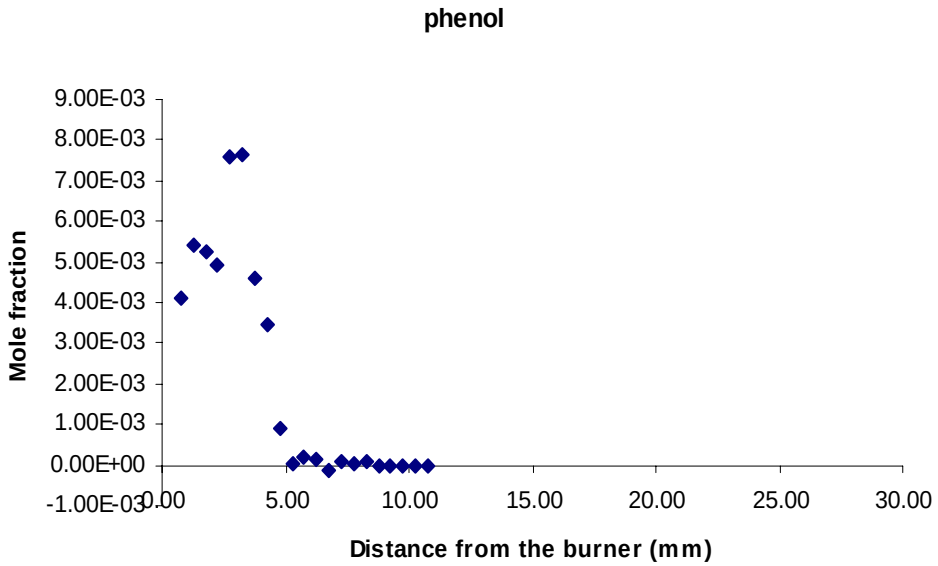

Figure 3.101. Mole-fraction profile of phenol in the fuel-rich toluene flame.

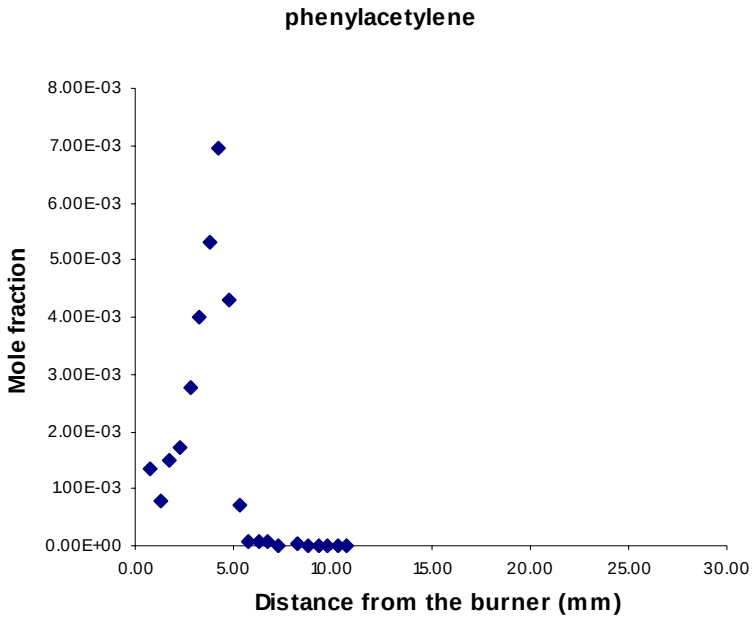

Figure 3.102. Mole-fraction profile of phenylacetylene in the fuel-rich toluene flame.

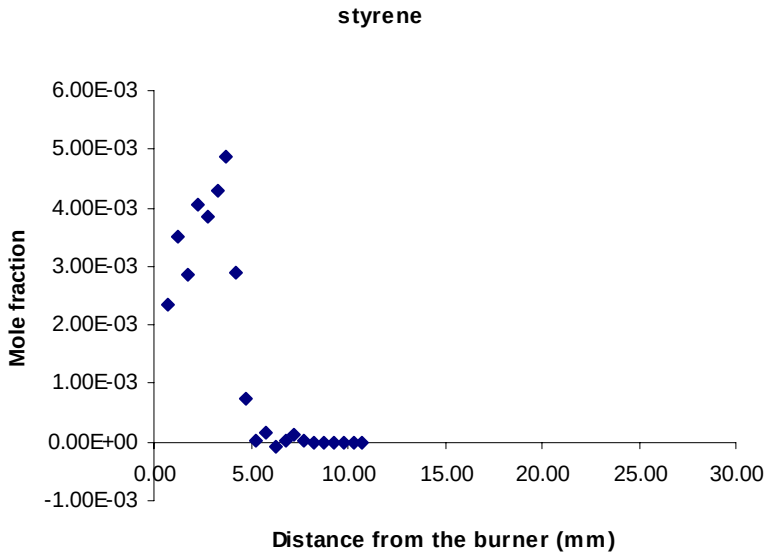

Figure 3.103. Mole-fraction profile of styrene in the fuel-rich toluene flame.

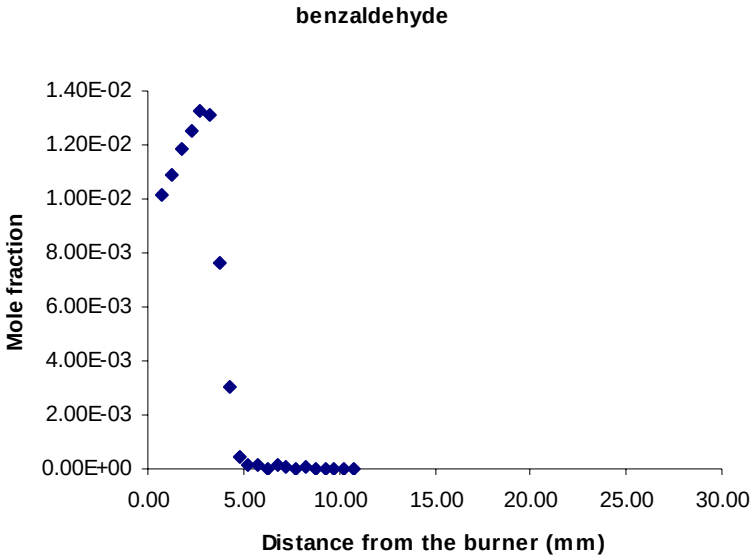

Figure 3.104. Mole-fraction profile of benzaldehyde in the fuel-rich toluene flame.

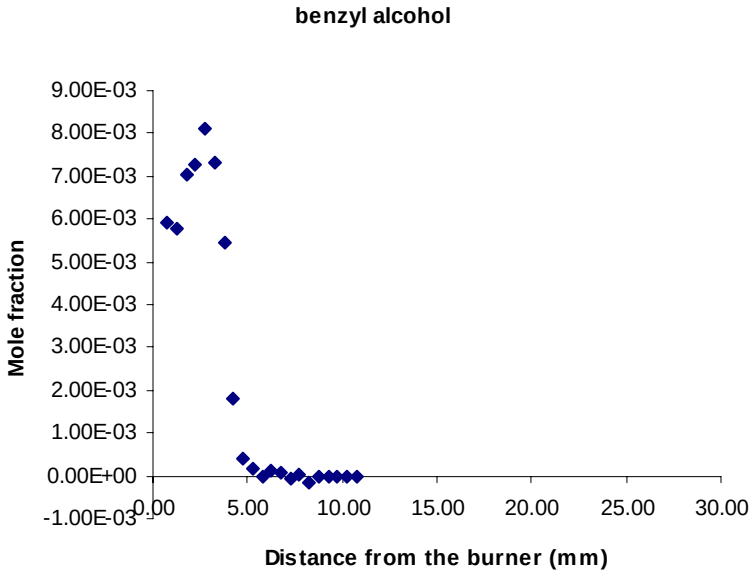

Figure 3.105. Mole-fraction profile of benzyl alcohol in the fuel-rich toluene flame.

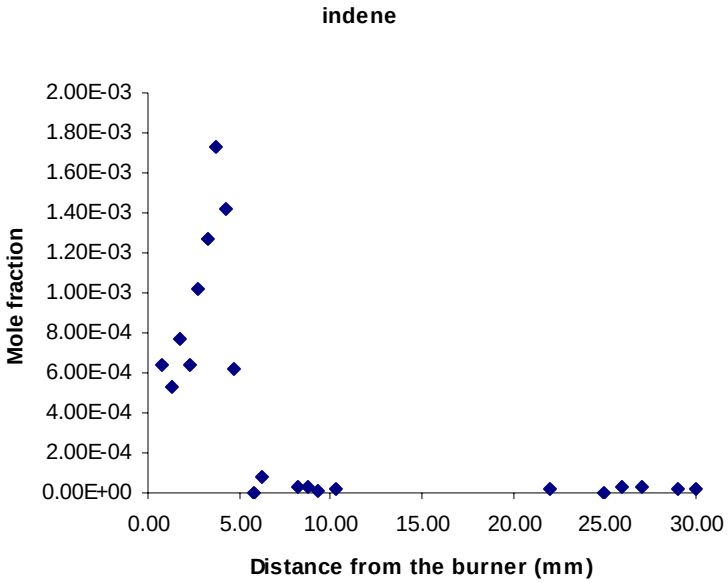

Figure 3.106. Mole-fraction profile of indene in the fuel-rich toluene flame.

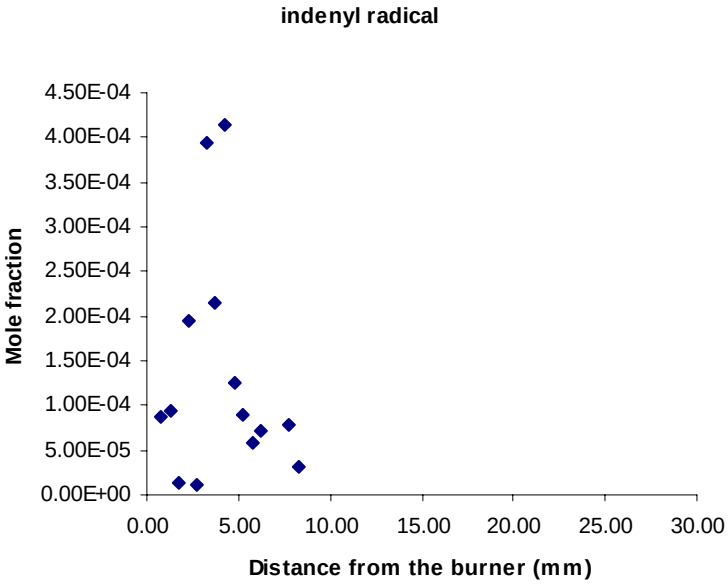

Figure 3.107. Mole-fraction profile of indenyl radical in the fuel-rich toluene flame.

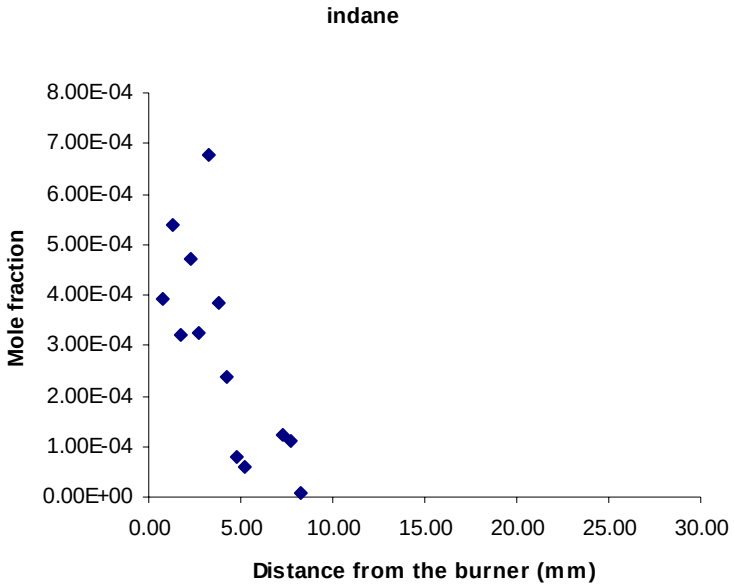

Figure 3.108. Mole-fraction profile of indene in the fuel-rich toluene flame.

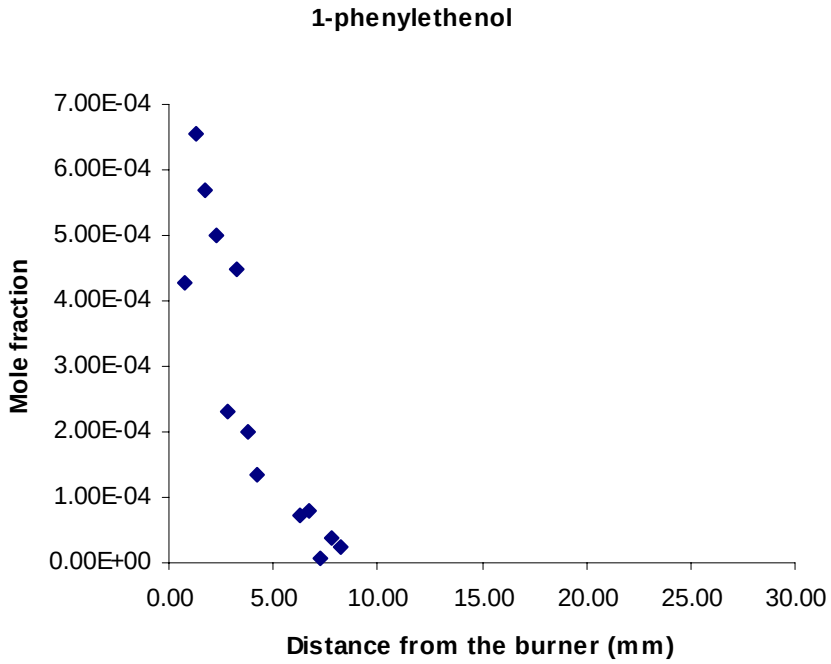

Figure 3.109. Mole-fraction profile of 1-phenylethenol in the fuel-rich toluene flame.

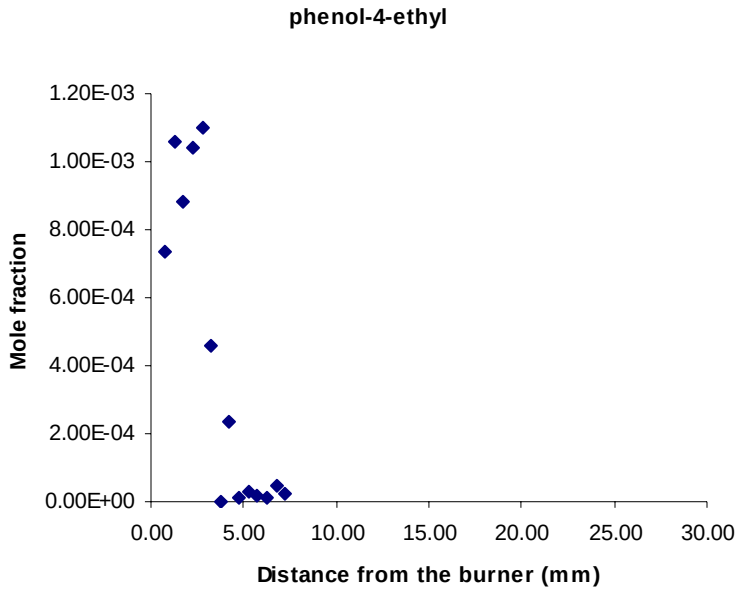

Figure 3.110. Mole-fraction profile of 4-ethylphenol in the fuel-rich toluene flame.

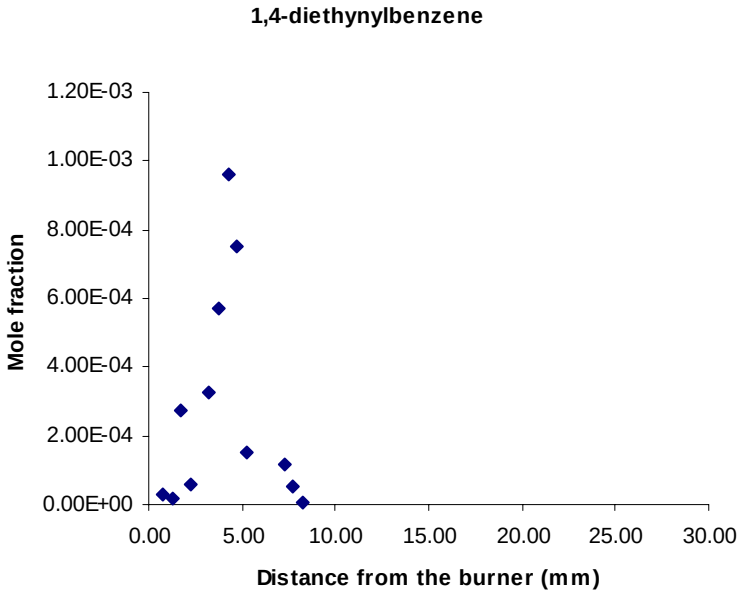

Figure 3.111. Mole-fraction profile of 1,4-diethynylbenzene in the fuel-rich toluene flame.

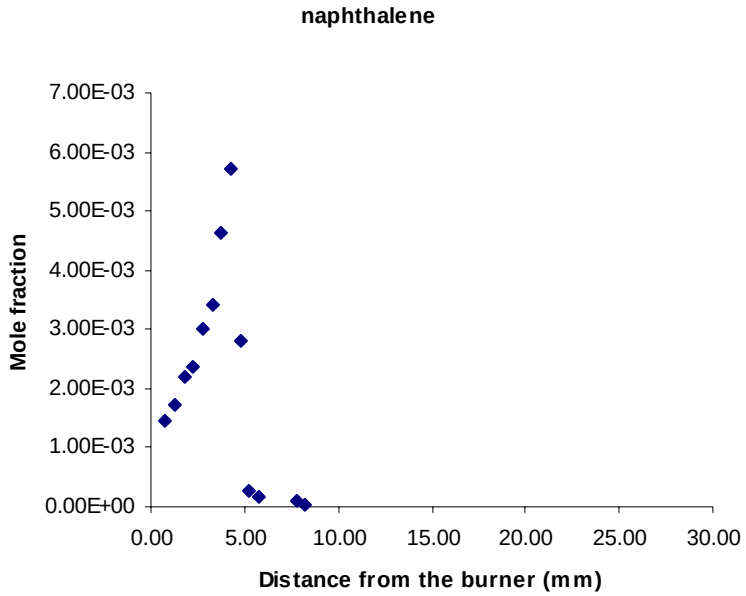

Figure 3.112. Mole-fraction profile of naphthalene in the fuel-rich toluene flame.

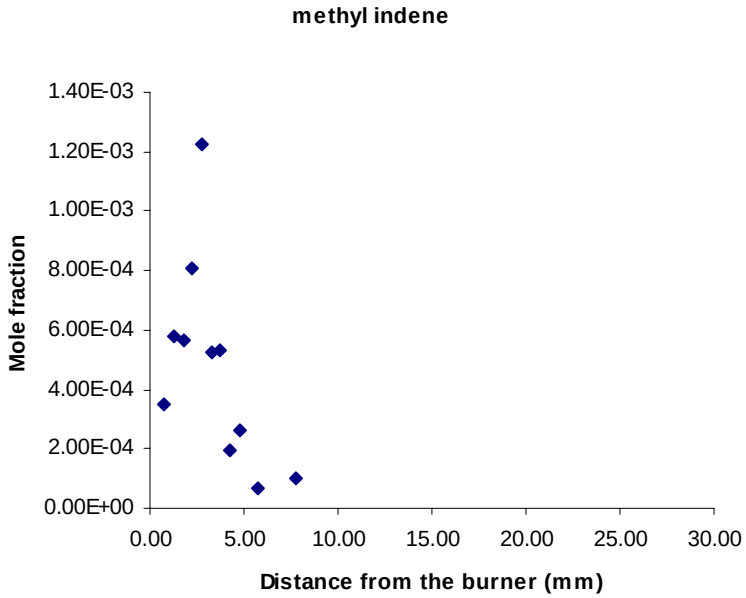

Figure 3.113. Mole-fraction profile of methylindene in the fuel-rich toluene flame.

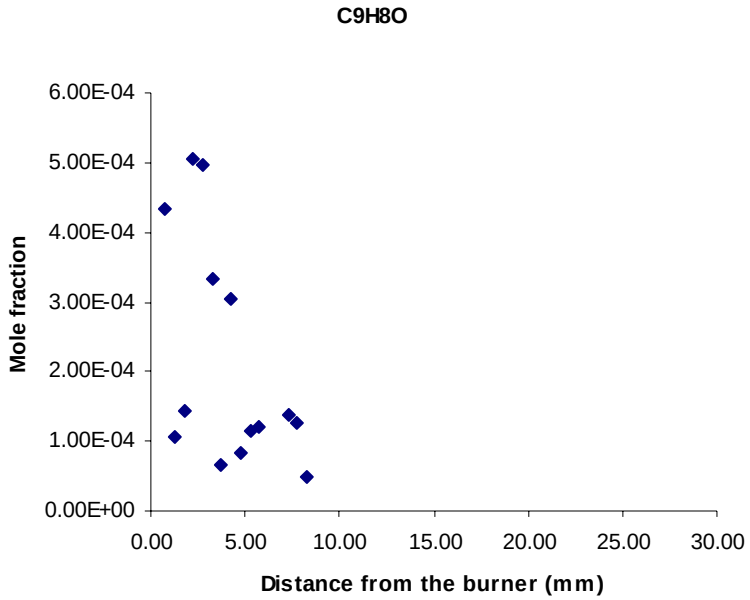

Figure 3.114. Mole-fraction profile of C_9H_8O in the fuel-rich toluene flame.

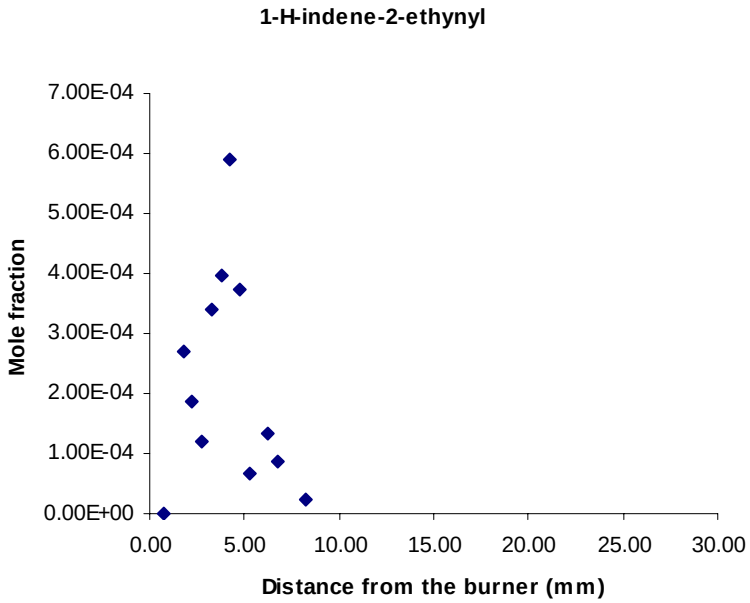

Figure 3.115. Mole-fraction profile of 1-H-indene-2-ethenyl in the fuel-rich toluene flame.

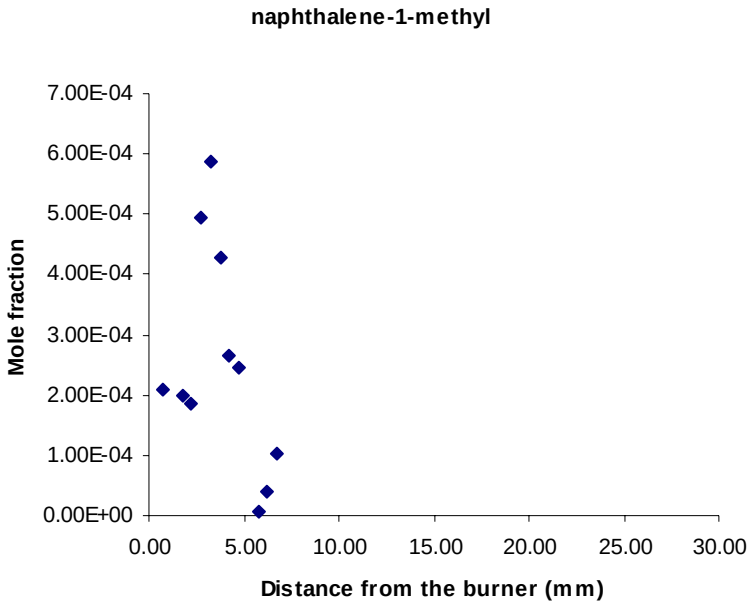

Figure 3.116. Mole-fraction profile of naphthalene-1-methyl in the fuel-rich toluene flame.

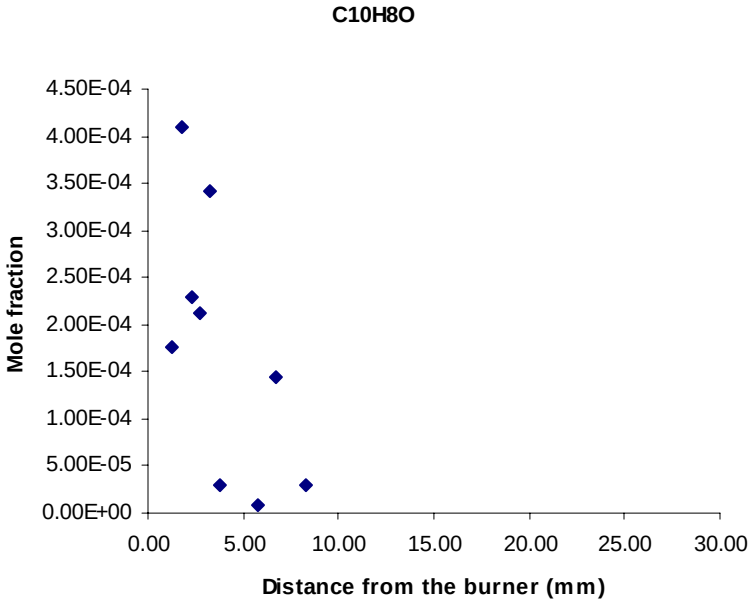

Figure 3.117. Mole-fraction profile of $C_{10}H_8O$ in the fuel-rich toluene flame.

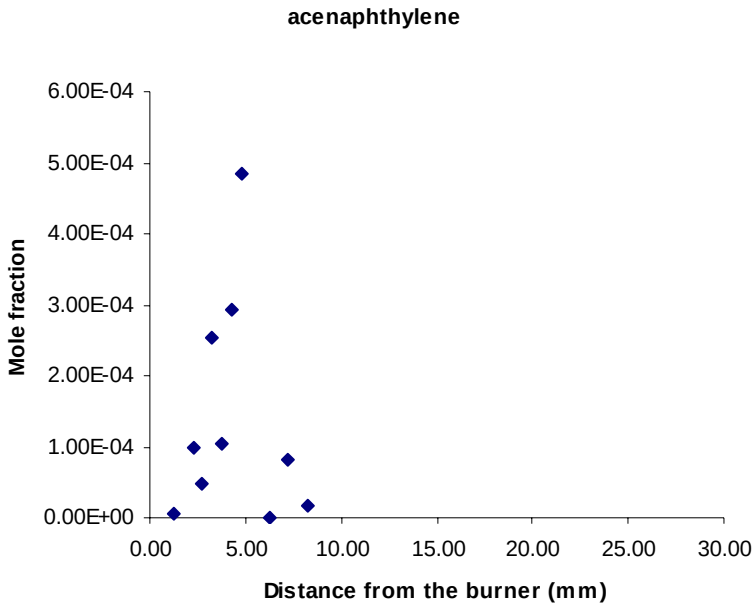

Figure 3.118. Mole-fraction profile of acenaphthylene in the fuel-rich toluene flame.

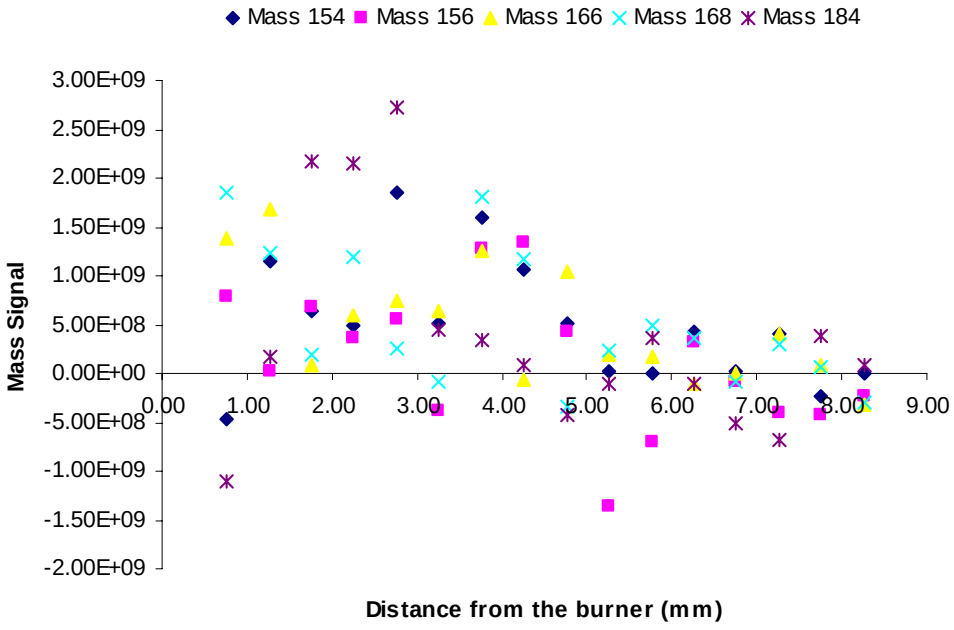

Figure 3.119. Signals of mass 154, 156, 166, 168 and 184 in the fuel-rich toluene flame.

Mass 1. The mass 1 species was not detected in the energy scan range of 8.5 to 11.0 eV. The species showed up at 14.35 eV burner scan. It was considered as hydrogen atom. The hydrogen atom mole-fraction profile is depicted in Figure 3.74. It shows an increase in hydrogen atom mole fraction away from the burner for a while and then shows a decrease into the post-flame zone.

Mass 2. The mass 2 species was not detected in the energy scan range of 8.5 to 11 eV. The species appeared at 16.2 eV burner scan. It was identified as hydrogen molecule. The hydrogen mole-fraction profile is depicted in Figure 3.75. Hydrogen mole fraction has a steady increase away from the burner to about 5.76 mm, and then it remains almost constant throughout the post-flame gases.

Mass 15. The mass 15 was identified as methyl (CH_3) radical, based on its mass and threshold ionization energy reported in Table 3.5. The mole-fraction profile was reported in Figure 3.78. It shows a peak in methyl radical mole fraction at 3.76 mm and then reaches near almost zero at 8.26 mm away from the burner.

Mass 16. The mass 16 signal was identified as methane (CH_4) and O. They were identified following the same principles as discussed in section 3.3.1. A 13.2 eV burner scan was used to obtain the methane mole fractionmole-fraction profile (Figure 3.77). The mole-fraction profile shows a peak at 2.76 mm. A burner scan at 14.35 eV was used to obtain the atomic oxygen mole fraction. The oxygen mole-fraction profile is depicted in Figure 3.78. It shows a peak at 3.26 mm.

Mass 17. The mass 17 signal was treated as hydroxyl radical (OH). A 13.2 eV burner scan was used to obtain its mole-fraction profile. The mole-fraction profile shows a scattered signal (Figure 3.79).

Mass 18. The mass 18 signal was identified as water. The mole-fraction profile of water is given in Figure 3.73.

Mass 26. The mass 26 was identified as acetylene (C_2H_2) based on the same principles discussed in section 3.2.1. The mole fraction profile is depicted in Figure 3.80. The profile shows a peak at 4.76 mm.

Mass 28. As discussed in the lean-toluene flame, carbon monoxide (CO) and ethylene (C_2H_4) were identified as the two species present as mass 28. The peak for the C_2H_4 signal is observed at 2.26 mm. The CO signal showed a gradual increase away from the burner and then it remained at steady state in the post-flame zone. Figure 3.73 shows the CO mole fraction and Figure 3.81 shows the C_2H_4 mole fraction profile.

Mass 30. The mass 30 species was identified as formaldehyde (HCHO). Figure 3.82 depicts its mole-fraction profile. The profile shows a peak at 3.26 mm.

Mass 32. The mass 32 species was identified as molecular oxygen (O_2). Figure 3.73 depicts its mole fraction profile along with other major species. The oxygen profile shows a sharp decrease in oxygen mole fraction to 5.76 mm away and becomes negligible in the post-flame zone.

Mass 39. The mass 39 species was identified as propargyl (C_3H_3). Figure 3.83 depicts its mole-fraction profile. The propargyl profile shows a peak at 4.26 mm.

Mass 40. Allene, propyne, and argon were found in the fuel-rich toluene flame. Figure 3.73 shows the mole fraction profile for argon along with other major species in the flame. The argon mole fraction profile shows a decrease to 5.26 mm away from the burner and then it remained steady. Figure 3.84 shows the mole fraction profile for allene and propyne.

Mass 42. The mass 42 species was identified as ketene (C_2H_2O). Its mole-fraction profile is depicted in Figure 3.85. The profile shows a peak at 3.78 mm.

Mass 44. The mass 44 species was identified as carbon dioxide (CO_2). Although CO_2 did not appear in the energy scan (8.5 to 11 eV) as it has a higher ionization energy, but the mass 44 signal that was detected at 14.35 eV was considered to be CO_2. Its profile is shown in Figure 3.73 along with other major species.

Mass 50. The mass 50 species was identified as 1,3-butadiyne or diacetylene. Figure 3.86 depicts its mole-fraction profile. The profile shows a peak at 4.76 mm.

Mass 52. The mass 52 species was identified as 1-buten-3-yne or vinylacetylene. Figure 3.87 depicts its mole-fraction profile. The profile shows a peak at 3.78 mm.

Mass 54. The mass 54 species was identified as 1,3-butadiene. Figure 3.88 depicts its mole-fraction profile. A burner scan at 9.977 eV was used to get its mole fraction profile. The profile shows a peak at 2.76 mm.

Mass 56. The mass 56 species was identified as methoxy acetylene. Its mole-fraction profile is depicted in Figure 3.89. The profile shows a peak at 2.76 mm.

Mass 64. The mass 64 species was identified as 1,3-pentadiyne (C_5H_4). Figure 3.90 depicts its mole-fraction profile. The profile shows a peak at 4.26 mm.

Mass 65. The mass 65 species was identified as cyclopentadienyl radical (C_5H_5). Figure 3.91 depicts its mole-fraction profile. The profile shows a peak at 3.78 mm.

Mass 66. The mass 66 species was identified as 1,3-cyclopentadiene (C_5H_6). Figure 3.92 depicts its mole-fraction profile. The profile shows a peak at 3.78 mm.

Mass 68. The mass 68 species was identified as cyclopentene. Figure 3.93 depicts its mole-fraction profile. The profile shows a peak at 2.26 mm.

Mass 74. The mass 74 species was identified as 1,3,5-hexatriyne or triacetylene(C_6H_2). Figure 3.94 depicts its mole-fraction profile. A burner scan at 9.977 eV was used to get its mole fraction profile. The profile shows a peak at 4.76 mm.

Mass 76. The mass 76 species was identified as benzyne (C_6H_4). Figure 3.95 depicts its mole-fraction profile. The profile shows a peak at 4.26 mm.

Mass 78. Fulvene (C_6H_6) and benzene (C_6H_6) were identified from the PIE scan of mass 78 signal. Benzene was found to be the dominant species at mass 78. Hence the total mass 78 signal was considered as benzene and its mole fraction was obtained. Figure 3.96 depicts the benzene mole-fraction profile. It shows a peak at 3.78 mm.

Mass 80. The mass 80 species was identified as methyl cyclopentadiene (C_6H_8). Figure 3.97 depicts its mole fraction profile. A burner scan at 9.977 eV was used to get its mole-fraction profile. The profile shows a peak at 2.76 mm.

Mass 82. The mass 82 species was identified as 1,2-butadienone-3-methyl. Figure 3.98 depicts its mole-fraction profile. The profile shows rapid decrease of the species away from the burner.

Mass 90. The mass 90 species was identified as 1,3-cyclopentadiene-5-ethenylidene. Figure 3.99 depicts its mole-fraction profile. The profile shows a peak at 4.26 mm.

Mass 91. The mass 91 species was identified as benzyl radical. Figure 3.100 depicts its mole-fraction profile. The profile shows a peak at 3.78 mm.

Mass 92. The mass 92 species was identified as toluene (C_7H_8).This is the fuel in the flame. Figure 3.73 depicts its mole-fraction profile. It shows that all the toluene is oxidized within 4.76 mm.

Mass 94. The mass 94 species was identified as phenol (C_6H_6O). Figure 3.101 depicts its mole-fraction profile. It shows a peak at 2.76 mm.

Mass 102. The mass 102 species was identified as phenylacetylene (C_8H_6). Figure 3.102 depicts its mole-fraction profile. It shows a peak at 4.26 mm.

Mass 104. The mass 104 species was identified as styrene (C_8H_8). Figure 3.103 depicts its mole-fraction profile. It showed a peak at 3.78 mm.

Mass 106. The mass 104 species was identified as benzaldehyde (C_7H_6O). Figure 3.104 depicts its mole-fraction profile. At 2.76 mm it forms a peak.

Mass 108. The mass 108 species was identified as benzyl alcohol (C_7H_8O). Figure 3.105 depicts its mole-fraction profile. At 2.76 mm it forms a peak.

Mass 115. The mass 115 species was identified as indenyl radical (C_9H_7). Figure 3.107 depicts its mole-fraction profile. At 2.76 mm it forms a peak.

Mass 116. The mass 116 species was identified as indene (C_9H_8). Figure 3.106 depicts its mole-fraction profile. At 2.76 mm it forms a peak.

Mass 118. The mass 118 species was identified as indane (C_9H_{10}). Figure 3.108 depicts its mole-fraction profile. At 3.26 mm it forms a peak.

Mass 120. The mass 120 species was identified as 1-phenylethenol (C_8H_8O) . Figure 3.109 depicts its mole-fraction profile. At 1.26 mm it forms a peak.

Mass 122. The mass 122 species was identified as phenol,4-ethyl ($C_8H_{10}O$) . Figure 3.110 depicts its mole-fraction profile. At 1.26 mm it forms a peak.

Mass 126. The mass 126 species was identified as 1,4-diethynylbenzene ($C_{10}H_6$). Figure 3.111 depicts its mole-fraction profile. At 4.26 mm it forms a peak.

Mass 128. The mass 128 species was identified as naphthalene ($C_{10}H_8$). Figure 3.112 depicts its mole-fraction profile. At 4.26 mm it forms a peak.

Mass 130. The mass 130 species was identified as methyl indene. Figure 3.113 depicts its mole-fraction profile. At 2.76 mm it forms a peak.

Mass 132. A species shows up as mass 132. Its ionization energy is below 8.5 eV, and it forms close to the burner surface. It might be an oxygenated species (C_9H_8O). With a carefully estimated cross section for this species, its mole-fraction profile is obtained and given in figure 3.114.

Mass 140. The mass 140 species was proposed to be as 1H-indene-2-ethynyl. Figure 3.115 depicts its mole fraction profile. At 4.26 mm it forms a peak.

Mass 142. The mass 142 species was proposed to be as 1-methylnaphthalene. Figure 3.116 depicts its mole-fraction profile. At 3.26 mm it forms a peak.

Mass 144. A species shows up as mass 144. Its ionization energy is below 8.5 eV, and it forms close to the burner surface. It might be an oxygenated species ($C_{10}H_8O$). With a carefully estimated cross section for this species, its mole-fraction profile is obtained and given in Figure 3.117.

Mass 152. The mass 152 species was identified as acenaphthylene ($C_{12}H_8$). Figure 3.118 depicts its mole-fraction profile. At 4.76 mm it forms a peak.

Other higher hydrocarbons. Species with mass 154, 156, 166, 168, and 184 were detected in the flame. These signals are weak and the ionization energies of these species appear to be below 8.5 eV. Further investigation is needed to identify these species. The raw signals for these species are depicted in Figure 3.119.

3.4.2 Checks for mole-fraction-profile analysis

The mole-fraction profiles obtained from the flame data was checked with the initial feed composition, and a mole balance was performed with hydrogen and carbon atom balances in the feed and the post-flame zone of the flame.

Initial mole fraction of the feed gas going into the burner was obtained from the feed conditions of the toluene flame. This result was then compared against the mole fraction achieved for the first data point away from the burner. The comparison is tabulated in Table 3.9.

Table 3.9. Comparison of mole fraction of the feed composition and mole fraction obtained at the first data point away from the burner.

	Mole fraction in the feed gas	Mole fraction at 1.35 mm away from the burner
Toluene	0.091	0.128
Oxygen	0.548	0.37
Argon	0.361	0.21

The initial check suggests that something is wrong with the data or data analysis as the initial mole fraction of toluene is slightly higher than that in the feed gas. This implies a need for re-measuring the species profiles in the flame.

3.5 Temperature measurements for the toluene and methane flames

Experiments were done to measure the temperature profiles of the two toluene flames discussed beforehand and a stoichiometric methane flame. But after the experiments were done it was found that, there was an air leak while the flow conditions were calibrated. This air leak led to low flow rate of oxygen and made the toluene flames fuel-rich. After the air leak was fixed the exact flow rates for these flames were found out

and hence their fuel equivalence ratios were recalculated. Although the species measurements were not done with these flames, the temperature profile for these flames is reported here, as these data might be useful in the future.

Figure 3.120 depicts the temperature for the methane flame. Figure 3.121 depicts the temperature profile for a toluene flame (Φ=2.03) and Figure 3.122 depicts the temperature profile for a toluene flame (Φ=3.97).

The difference between the heated and unheated temperature for the toluene flame (Φ=3.97) is significantly less compared to the difference between the two in other flames. This attributes to an error while measuring the temperature in this toluene flame. While the thermocouple was being heated up with the resistive circuit, it was heated up to 18 mV (approximately). The data points were far away from the calibration curve and they were linearly extrapolated to get the crossing point between the data points and the calibration curve. This led to the error in getting the heated temperature accurately. However the unheated temperature that was measured with the thermocouple would be able to provide an estimation of temperature for the toluene flame.

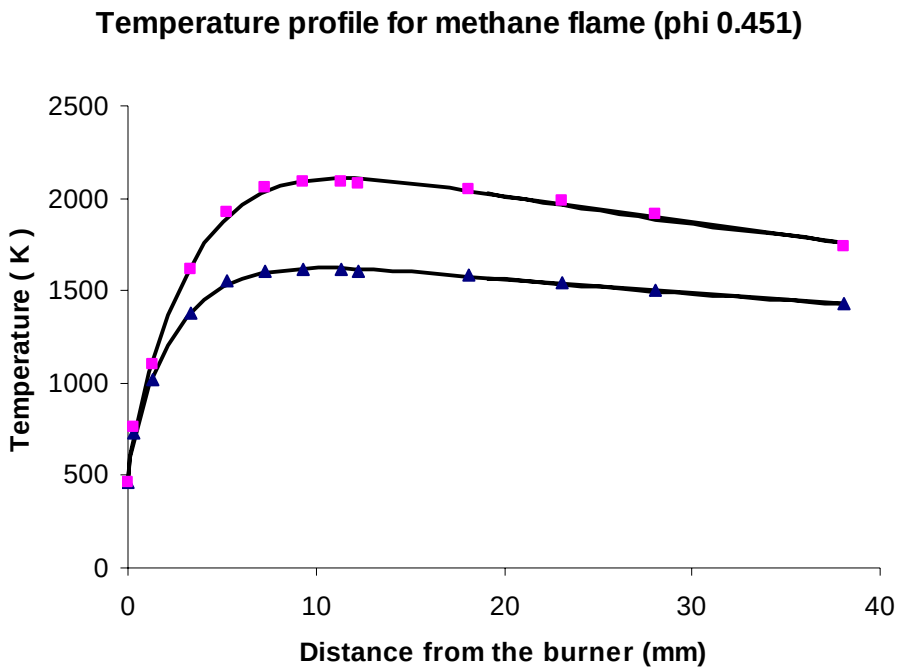

Figure 3.120. Temperature profile for methane flame (Φ =0.451) (■ Heated temperature, ▲unheated temperature).

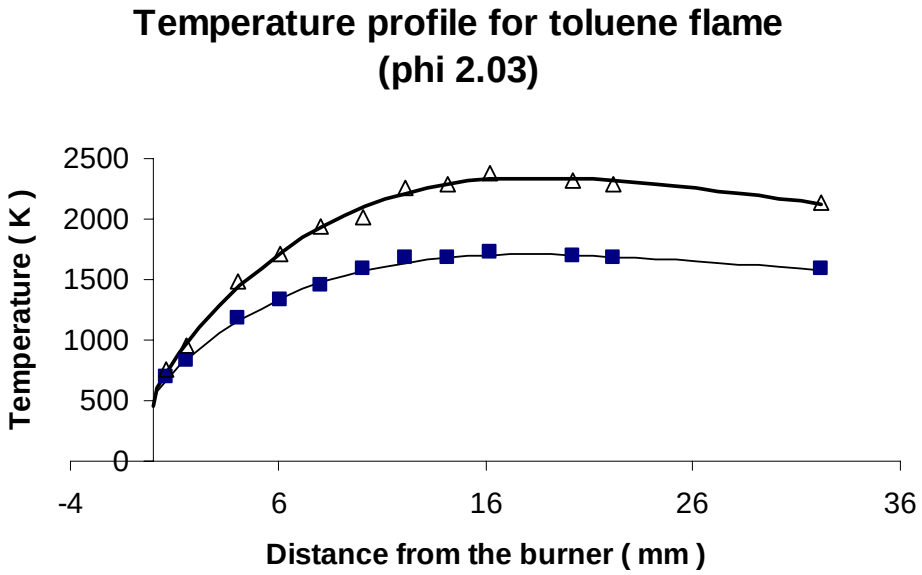

Figure 3.121. Temperature profile for toluene flame (Φ = 2.03)

(Δ Heated temperature, ■ unheated temperature).

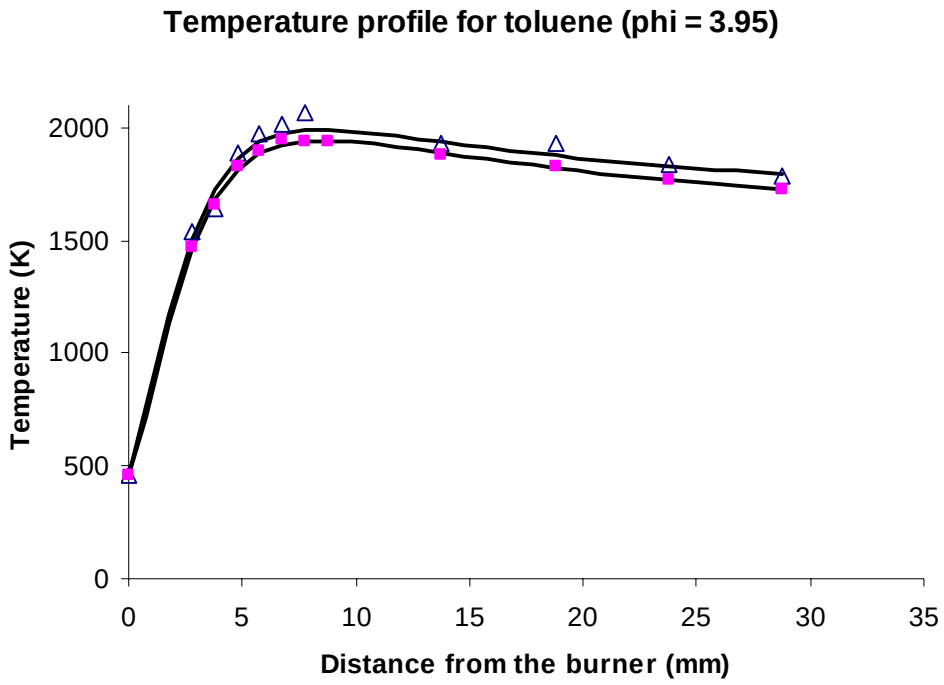

Figure 3.122. Temperature profile for toluene flame (Φ = 3.97)

(Δ Heated temperature, ■ unheated temperature).

CHAPTER 4

CONCLUSIONS AND RECOMMENDATIONS

4.1 Conclusions

Measurements. Three flames were studied with the MBMS system at the ALS during the course of this dissertation. One fuel-rich cyclohexane flame was studied to compare against a stoichiometric cyclohexane flame studied in the group before. Two toluene flames (one fuel-rich and the other fuel-lean) were studied to understand the hydrocarbon growth chemistry in combustion. Toluene was chosen as it was believed that more and more higher hydrocarbons would be observed in the toluene flame.

Several species were identified in these three flames. Their mole-fraction profiles were obtained. Species identification and their mole-fraction profiles contribute significantly to highlight the reactions going on in the flame. Thus, a useful basis for an understanding of the hydrocarbon flame kinetics was obtained during this study.

The fuel-rich cyclohexane flame analysis showed formation of some higher hydrocarbons that were not observed in the stoichiometric cyclohexane flame measured in the group previously. These species are triacetylene (C_6H_2), p-xylene (C_8H_{10}), indene (C_9H_8), styrene (C_8H_8), and naphthalene (C_8H_{10}). The formation of triacetylene indicates that when fuel equivalence ratio is increased, the polyacetylene chemistry in the flames become significant. It has been a long-standing debate whether these linear long-chain molecules contribute much to the formation of soot. The other group of thought is that the polyaromatic hydrocarbons (PAH) like indene and naphthalene are the precursors for soot. Although these PAHs were observed in the flame and their mole-fraction profiles

were obtained, the concentrations for these species were very low and the mole-fraction profiles looked scattered. Tetra-acetylene (C_8H_2) (I.E. 9.09 ± 0.02 eV) was believed to be in the flame, but the presence of cyclohexanone (I.E 9.16 ± 0.02 eV) dominates any signal from it. These species have the same mass number (98) and their ionization energies are very close. The burner scan of mass 98 shows a species close to the burner surface; hence, for this study it was considered that the mass 98 species was more likely cyclohexanone because the polyacetylenes form only at high temperatures. A richer cyclohexane flame could be studied in the future to look for the formation of higher hydrocarbons in cyclohexane flames.

Cyclohexane flame modeling. Preliminary modeling was performed for the fuel-rich cyclohexane flame with CHEMKIN. The convergence of the code was achieved only without considering thermal diffusion. A previous analysis with a stoichiometric cyclohexane flame modeling showed that the change in the mole fraction profile of the major species does not change much when thermal diffusion is considered. Suitable adjustments should be made in the mechanism or the code so that the calculation will converge while it accounts for thermal diffusion.

The preliminary modeling results are discussed in Appendix C. A SENKPLOT analysis of the major reaction pathways for the cyclohexane flame has been performed and is discussed in Appendix C as well. A qualitative comparison between the experimental results and the model prediction shows similarity in shape for the mole fraction profiles of major species Ar, H_2O, CO, CO_2, O_2 ,cyclohexane and H_2 in the flame.

Species in the toluene flames. The two toluene flames that have been studied in the current research show several species that were not detected in the fuel-rich cyclohexane flame.

- The radicals H, OH and O were observed in the toluene flames. These radicals should have been observed in the fuel-rich cyclohexane flame as well because these radicals play key roles in the combustion chemistry of all the hydrocarbons. This problem has been identified as one of the weakness of the ALS system because with this system, the data for H, O, and OH for different hydrocarbon flames are not consistent.
- In the fuel-lean toluene flame, the mass 42 species was identified as ketene only. In the rich toluene flame both ketene and propene were identified.
- In the fuel-rich toluene flame, several higher hydrocarbons were observed as well. These mass species are mass 115, mass 128, mass 130, mass 132, mass 140, mass 142, mass 144, mass 152, mass 154, mass 156, mass 166, mass 168, mass 180, mass 182 and mass 184. The presence of these species once again is consistent with the importance of PAHs in soot formation.

Temperatures. Temperature measurement is an important aspect of combustion studies. The temperature measurements were carried out in the UMass apparatus for the fuel-rich cyclohexane flame, two toluene flames, and a lean methane flame as well. These temperature measurements should be helpful in understanding the detailed reaction chemistry of combustion for these fuels.

4.2 Recommendations

Recommendation 1. The liquid feed delivery system for the UMass apparatus can be upgraded for better accuracy and ease of experimentation.

- The current set-up uses four syringes in a syringe pump (Model PHD 2000, Harvard Apparatus). The operating limit of atmospheric pressure for these syringes makes it hard for the experiment. When the pressure in the vaporizer goes below atmospheric, air leaks into the syringes, which imparts error to the liquid flow rate. When the pressure in the vaporizer goes above atmospheric, the vapor starts pushing the liquid out of the syringes, which again imparts error in the liquid flow rate and creates a flame hazard in the lab as well. It takes lot of time and effort to build the right pressure in the vaporizer and get a stable flame with this setup.
- Even after a stable flame is achieved, the storage capacity of the syringes brings further limitation in operation. Two syringes can deliver 100 ml of fuel altogether. When two syringes are emptied, the other two syringes are filled and the direction of the syringe pump needs to be reversed. There is always a possibility that the flame may go out during this transition. Even if the flame survives the transition, it takes about 20 minutes approximately to make the flame stable.
- Getting rid of the air bubbles from the syringes is a laborious process, as the whole syringe-pump assembly needs to be held upright while the pump is running, and the buoyancy of the bubbles helps to get rid of them. A syringe pump assembly with a big single syringe standing upright can work better to resolve this issue.

Recommendation 2. While measuring the temperature profile with the UMass system, it was found that the voltage reading fluctuates within a small range. The upper and lower bounds of that range were noted, and the average voltage was used to measure the temperature. Manual reading might incorporate error in the experimental data, hence a computer-controlled data acquisition system for reading the data over a period of time and averaging them might be more accurate way of reporting the data.

Recommendation 3. The tubing that carries the liquid vapor to the burner for the UMass system is heated with heating tapes and variable autotransformers. The temperature of the tubing is read at three points with a Type K thermocouple thermometer. This arrangement gives us a limited control over the actual temperature at which the tube can be heated. Care should be taken that the tubing is heated uniformly.

Recommendation 4. Measuring the area-expansion ratio profiles of the flames would bring more accuracy for modeling the flame. The area expansion ratios for the studied hydrocarbon flames need to be found and incorporated in the modeling.

Recommendation 5. The issue related to the uncertainty in seeing the important radicals O, OH and H with the ALS system should be investigated. Careful preparation of the quartz sampling probe should resolve this issue. As one aspect, surface-catalyzed radical recombination reactions might be the key. In order to make the quartz probe outer surface perfect, the surface of the quartz probe was polished with sandpaper and crocus cloth until a good water-jet test was achieved with the cone (an aligned water jet produced in the probe from pressurized water at the probe tip). The experimental results showed a better signal intensity for these radicals detected in ALS. However the probe surface was cleansed with distilled water at that point. A dilute solution of hydrofluoric

acid would be able to cleanse the surface properly, and a second wash with distilled water would minimize the catalyzed radical recombination on the probe surface as suggested by Law (2005). This cleansing method should be incorporated to see if this solves the OH, H and O detection problem at the ALS.

Recommendation 6. The UMass apparatus was able to detect the radicals O, H, and OH in hydrocarbon flames. The mole fraction profiles of these radicals should be found for the cyclohexane and toluene flames.

Recommendation 7. Some of the higher hydrocarbons in the fuel-rich toluene flame were not identified sufficiently. The energy scans for these species were conducted at a range of 8.5 to 11.0 eV. The PIE scans of these species were observed to be below 8.5 eV, as mentioned in Chapter 3. Most of these higher hydrocarbons show a peak at 4.26 mm away from the burner; however, some of the oxygenated species show maxima closer to the burner surface (at 1.76 mm away from the burner). A PIE scan in the range of 7 to 11 eV at 3 mm away from the burner would be helpful to identify these species.

Recommendation 8. In the fuel-rich cyclohexane and fuel-rich toluene flames, both propene and ketene were found at mass 42, but as their ionization energies lie very close to each other, these species were not resolved with the ALS equipment. The UMass equipment has better mass resolution than the ALS equipment. These species need to be resolved with the UMass system for the flames mentioned above.

Recommendation 9. Detailed modeling needs to be done for the cyclohexane and toluene flames. The reactions leading to the high-molecular weight species found in the fuel-rich toluene flame might clarify interesting aspects in understanding the hydrocarbon growth mechanism in flames.

Recommendation 10. When the flow conditions for the fuel-lean toluene flame were being set for temperature measurements with UMass system, there was an air leak that created a different toluene flame from that which was desired. It became a fuel-rich ($\Phi = 2.02$) flame. The temperature profile that was measured with this flame showed a very gradual increase in temperature away from the burner. The flame stood away from the burner, it was very stable, and the luminous reaction zone was very wide (approximately 25 mm). The flame was not emitting soot. The wide reaction zone of this flame would lead to wider peaks for the intermediate hydrocarbons formed in the flame. This flame would be interesting to study. The mole-fraction profiles for this flame should be analyzed, and this flame should be modeled as the temperature profile for this flame has already been measured in the current work. A similar air-leak problem was also encountered while temperature profiles were being measured for a stoichiometric methane flame and a rich-toluene flame. As the temperature profile for these flames has already been measured, their mole fraction profiles can be measured, so that these flames could be modeled.

Recommendation 11. The photo-ionization cross sections for different hydrocarbons are not readily available in the literature, and there is ambiguity for the specific photo-ionization cross sections of different species in the literature as well. In this current research, the photo-ionization cross sections that had been measured in the ALS/MBMS group were mainly used. For several intermediate species, an expression used by Koizumi (1990) was used. Although this might be a good first approximation, the expression suggests that the photo-ionization cross section decreases with increasing

photon energy, which is contradictory to the experimental findings. Hence, a better way for approximating the photo-ionization cross sections needs to be investigated.

APPENDIX A

PHOTOIONIZATION CROSS-SECTIONS AND MASS DISCRIMINATION FACTORS

A.1 Photo-ionization cross-sections used:

This appendix presents the values used in this work for photo-ionization cross-sections. The values are given in megabarn (mbarn). The notations used for references are as follows.

A Palenius et al. (1976)

B Collaboratory for Multi-Scale Chemical Science, ALS Low Pressure Flames data base (cmcs.org)

C Samson and Pareek, 1985

D Dehmer, 1984

E Measured in the group

F Measured with the expression used by Koizumi, 1991

G Holland et al., 1993

H Cool et al., 2003

I Samson, and Stolte, 2002

Table A.1 Photo-ionization cross-sections

Mass (amu)	Name	IP (eV)	Energy measured at (eV)	Photo-ionization cross-section (mbarn)	References
1	Hydrogen atom (H)	13.59844	14.37	4.85	A
2	Hydrogen molecule (H_2)	15.42593 ±0.00005	16.22	8.032	B
15	Methyl radical (CH_3)	9.84±0.01	10.0	8	B
16	Methane (CH_4)	12.61 ±0.01	13.21	3.75	B
16	Oxygen (O)	13.61806	14.37	4.962	C
17	Hydroxyl radical (OH)	13.017 ±0.002	13.21	4	D
18	Water (H_2O)	12.621 ±0.002	13.21	7.2	B
26	Acetylene (C_2H_2)	11.4±0.00 2	12.32	29.77	E
28	Ethylene (C_2H_4)	10.5138 ±0.0006	12.32	11.48	B
28	Carbon monoxide (CO)	14.014 ±0.0003	14.37	26.542	B
29	Formyl radical (HCO)	8.12±0.04	10.00	6.913	F
30	Formaldehyde (HCHO)	10.88 ±0.01	11.52	10.129	B
32	Oxygen (O_2)	12.0697 ±0.0002	12.32	2.2	G
39	Propargyl (C_3H_3)	8.67±0.02	10.00	8.3	B
40	Allene (C_3H_4)	9.692 ±0.004	10.00	8.308	H
40	Propyne (C_3H_4)	10.36 ±0.01	10.52	23.06	H
40	Argon (Ar)	15.759 ±0.001	16.22	32.2	I
41	Allyl radical (C_3H_5)	8.18±0.07	10.00	6.2	B
42	Propene (C_3H_6)	9.73±0.01	10.00	6.316	B
42	Ketene (C_2H_2O)	9.617 ±0.003	11.52	6.9	F
44	Carbon dioxide (CO_2)	13.777±0. 001	14.37	20.65	B

Mass (amu)	Name	IP (eV)	Energy considered (eV)	Photo-ionization cross-section (mbarn)	References
50	1,3-butadiyne(C_4H_2)	10.17	10.52	23.82	E
52	1-Buten-3-yne(C_4H_4)	9.58±0.02	10.06	24.57	E
54	1,3-Butadiene (C_4H_6)	9.072±0.007	10.00	7.53	E
56	Methoxyacetylene (C_4H_8)	9.48	10.06	9.94	F
56	1-Butene	9.55±0.06	10.00	9.45	B
64	1,3-Pentadiyne (C_5H_4)	9.5 ± 0.02	10.00	8.2	F
65	Cyclopentadienyl (C_5H_5) radical	8.41/8.56	10.00	7.22	F
66	1,3-Cyclopentadiene (C_5H_6)	8.57 ± 0.01	10.00	7.39	F
68	1,3-Pentadiene (C_5H_8)	8.6	10.00	7.42	F
68	1,2-Butadienone (C_4H_4O)	8.68±0.05	10.06	7.45	F
70	2-Pentene (C_5H_{10})	9.01±0.03	10.00	7.89	F
74	1,3,5-Hexatriyne (C_6H_2)	9.5±0.02	10.00	8.48	F
76	Benzyne (C_6H_4)	9.03±0.05	10.00	7.91	F
78	Benzene (C_6H_6)	9.24378±0.00007	10.00	24.28	B
80	1,3-Cyclohexadiene (C_6H_8)	8.25	10.00	7.047	F
80	Methylcyclopentadiene (C_6H_8)	8.28±0.05	10.06	7.022	F
82	Cyclohexene (C_6H_{10})	8.95±0.01	10.00	7.817	F
82	1,2 Butadienone 3 methyl (C_5H_6O)	8.65	10.06	7.4	F
83	Cyclohexyl radical (C_6H_{11})	7.66±0.05	10.00	6.46	F

Mass (amu)	Name	IP (eV)	Energy measured at (eV)	Photo-ionization cross-section (mbarn)	References
84	Cyclohexane (C_6H_{12})	9.88±0.03	10.00	2.12	E
90	1,3-Cyclopentadiene,5-ethenylidene (C_7H_6)	8.29	10.06	7.03	F
91	Benzyl radical (C_7H_7)	7.242±0.006	10.06	6.02	F
92	Toluene (C_7H_8)	8.828±0.001	10.06	35	E
94	Phenol (C_6H_6O)	8.49±0.02	10.06	7.303	F
98	Cyclohexanone	9.16±0.02	10.00	8.06	F
102	Phenyl acetylene (C_8H_6)	8.82±0.02	10.00	7.67	F
104	Styrene (C_8H_8)	8.464±0.001	10.00	7.27	F
106	Para-xylene (C_8H_{10})	8.44±0.05	10.00	7.248	F
106	Benzaldehyde (C_7H_6O)	9.5±0.08	10.06	8.41	F
108	Benzyl alcohol (C_7H_8O)	8.26±0.05	10.00	7.06	F
115	Indenyl Radical (C_9H_7)	8.35	9.98	11.62	F
116	Indene (C_9H_8)	8.14±0.01	10.00	6.93	F
120	1-Phenylethenol (C_8H_8O)	8.01 ± 0.03	9.98	12.25	F
122	Phenol , 4-ethyl ($C_8H_{10}O$)	7.84	9.98	12.53	F
126	1,4-Diethynylbenzene ($C_{10}H_6$)	8.58 ± 0.02	9.98	11.23	F
128	Naphthalene ($C_{10}H_8$)	8.144 ±0.001	10.00	6.96	F
130	Methyl Indene ($C_{10}H_{10}$)	8.27	9.98	11.79	F
140	1H-Indene,2-ethynyl ($C_{11}H_8$)	8.04	9.98	12.2	F
142	Naphthalene,1-methyl ($C_{11}H_{10}$)	7.96 ± 0.03	9.98	12.34	F

Mass (amu)	Name	IP (eV)	Energy measured at (eV)	Photo-ionization cross-section (mbarn)	References
152	Acenaphthalene ($C_{12}H_8$)	8.12± 0.1	9.98	12.06	F

A.2 Mass discrimination factors used

Mass discrimination factors are used to rectify the error in the signal due to different velocities of ions of different masses. According to (Chernushevic et al., 2001), the velocity component of an ion in a monoenergetic beam in a time-of-flight mass spectrometer is inversely proportional to its mass-to-ion ratio. Thus lighter ions spread out over a distance larger than heavier ions. To account for this effect, mass discrimination factors are used. A sample gas with known mole fraction of the target species (whose mass discrimination factor is required) is fed into the instrument. The mass spectrometer detects its signal, and with known photo-ionization cross section of the species at a particular energy, its mass discrimination factor is measured. Mass discrimination factors measured for the ALS equipment were used for the data analysis in this study. The mass discrimination factors for a few species were measured, and the mass discrimination for the rest of the species were found by fitting a suitable curve through them. The data measured and the interpolated data with respect to argon are given below.

Table A.2 Experimental results of mass discrimination factors measured in ALS in January, 2006

Species	Mass	Mass discrimination factor
H_2	2.02	0.21
D_2	4.03	0.47
CH_4	16.04	0.47
C_2H_2	26.04	0.69
CO	28	0.70
Ar	39.948	1.00
C_3H_4	42.08	1.04
CO_2	44.01	1.06
C_6H_6	78.11	0.91
Mass 84	84	1.05
Mass 132	132	0.55

Table A.3 Interpolated mass discrimination factors relative to argon for other mass species

Mass	Mass discrimination	Mass	Mass Discrimination	Mass	Mass Discrimination
1	0.252	45	1.045	89	1.047
2	0.281	46	1.052	90	1.040
3	0.309	47	1.059	91	1.033
4	0.337	48	1.066	92	1.026
5	0.365	49	1.073	93	1.019
6	0.391	50	1.079	94	1.011

Mass	Mass discrimination	Mass	Mass Discrimination	Mass	Mass Discrimination
7	0.418	51	1.084	95	1.003
8	0.443	52	1.090	96	0.995
9	0.469	53	1.095	97	0.987
10	0.493	54	1.099	98	0.978
11	0.517	55	1.103	99	0.969
12	0.541	56	1.107	100	0.960
13	0.564	57	1.111	101	0.951
14	0.587	58	1.114	102	0.942
15	0.609	59	1.116	103	0.932
16	0.630	60	1.119	104	0.922
17	0.651	61	1.121	105	0.912
18	0.671	62	1.122	106	0.902
19	0.691	63	1.124	107	0.892
20	0.711	64	1.124	108	0.881
21	0.730	65	1.125	109	0.871
22	0.748	66	1.125	110	0.860
23	0.766	67	1.125	111	0.849
24	0.784	68	1.125	112	0.837
25	0.801	69	1.124	113	0.826
26	0.817	70	1.123	114	0.814
27	0.833	71	1.122	115	0.803
28	0.849	72	1.120	116	0.791

Mass	Mass discrimination	Mass	Mass Discrimination	Mass	Mass Discrimination
29	0.864	73	1.118	117	0.779
30	0.879	74	1.116	118	0.767
31	0.893	75	1.113	119	0.754
32	0.906	76	1.110	120	0.742
33	0.920	77	1.107	121	0.729
34	0.932	78	1.104	122	0.716
35	0.945	79	1.100	123	0.704
36	0.957	80	1.096	124	0.691
37	0.968	81	1.091	125	0.677
38	0.979	82	1.087	126	0.664
39	0.990	83	1.082	127	0.651
40	1.000	84	1.077	128	0.637
41	1.010	85	1.071	129	0.624
42	1.019	86	1.066	130	0.610
43	1.028	87	1.060	131	0.596
44	1.036	88	1.054	132	0.582

APPENDIX B

EXPERIMENTAL CALIBRATIONS

B.1 Gas flow calibration methods

As discussed in Chapter 2, the gas flow is calibrated against a dead volume. One sample calculation for setting up the flow condition for the cyclohexane flame is tabulated below. The required flow rate for oxygen and argon for the cylohexane flame is 1.058 slm and 0.564 slm respectively. The volume of the cylinder is 43.364 l. The temperature in the room was 294 K. Ideal gas law was applied to calculate the number of moles (M) in the cylinder. F refers to the molar flow rate.

Table B.1 Gas flow required.

Gas	Flow required (SLM)	Flow required (mole/sec)
Oxygen	1.058	0.000787
Argon	0.564	0.000412

Table B.2 Pressure and time reading for set point 52 for argon

Set point	Pressure (Torr)	Time (sec)	dt (sec)	M (moles)	dM (moles)	F (dM/dt) (moles/sec)	Average (moles/sec)
51	22.05	0	0	5.22E-02			4.06E-04
	24.02	11.67	11.67	5.68E-02	4.66E-03	3.99E-04	
	26.06	23.61	11.94	6.16E-02	4.82E-03	4.04E-04	
	28.05	35.14	11.53	6.63E-02	4.71E-03	4.08E-04	
	32.06	58.36	23.22	7.58E-02	9.48E-03	4.08E-04	
	35.05	75.61	17.25	8.29E-02	7.07E-03	4.10E-04	

The following graph represents the molar flow rate versus set point for the argon.

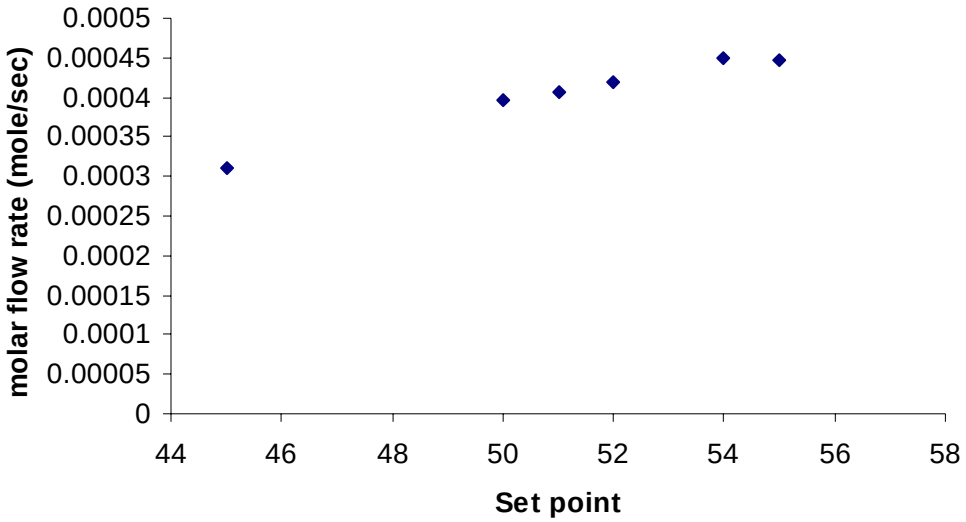

Figure B.1. Molar flow rate against set point in argon.

A similar procedure was followed to find the proper flow conditions for all the flames.

B.2 Calibration for the syringe pump

The syringe pump flow was calibrated using water at room temperature (20 ° C). The pump flow rate was set at a certain value, and then the pump was run for a known period of time. The water that came out of the pump was collected and weighed. From the density of water, the total volume delivered by the pump was calculated. Using this known volume and time, the volumetric flow rate was calculated.

Figure B.2 presents the actual flow rate against the target flow rate. The straight line represents the ideal case when actual flow rate equals the target flow rate. The points in the graph represents the data points. The deviation of the data points from the straight line represents the error involved with the syringe pump delivery rate.

It shows that as the target flow rate is decreased, the error decreases significantly. During the course of experiment, the maximum target flow rate required by the syringe pump was 0.6 ml/min. It was assumed that at this flow rate the error involved was negligible, but a fluctuation observed in the toluene and cyclohexane flame while measuring their temperature suggested that the syringe pump delivery rate might have fluctuated with time. This source of error needs to be further investigated.

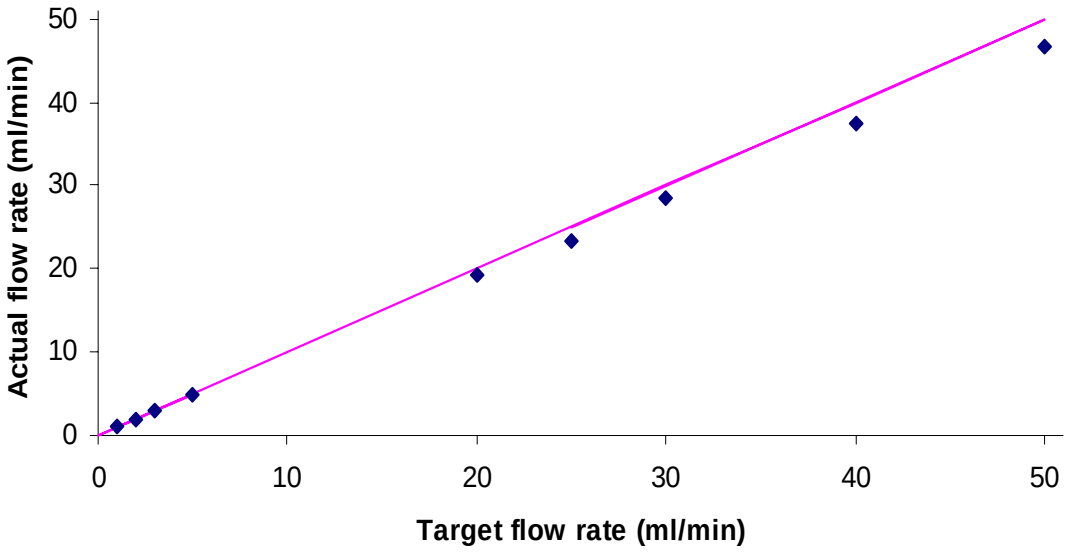

Figure B.2. Syringe pump calibration

(The straight line represents the ideal case where the actual flow rate equals the target flow rate, the diamonds represent the actual data point)

APPENDIX C

MODELING OF FUEL-RICH CYCLOHEXANE FLAME

CHEMKIN, a code developed by Sandia, was used for the preliminary flame modeling. A general description of the numerical properties of the code is discussed below.

C.1 Overview of the code

The code solves the one-dimensional transport equations and, in principle, the energy-balance equations. The flame is called one-dimensional because there is assumed to be no radial velocity gradient and temperature gradient across the burner. The common practice is to measure the temperature profile in the flame and fit that data into the code to solve the transport equation because the energy conservation equation can not be solved efficiently without knowing the energy losses in different flames to its surroundings. The modeling approach of the combustion system uses a combination of time-dependent and steady-state methods. The idea of coarse-to-fine grid refinement was used as a means to enhance the convergence properties of the steady state approach and as a means to provide optimal mesh placement. The model can be used for analyzing species profiles in flame experiments with a known mass flow rate.

C.2 Structure of the code.

The code depends on data and subroutines from the CHEMKIN and transport packages. Therefore to solve a flame problem, a command procedure needs to be set up that would allow for the execution of several preprocessor programs, the access to several

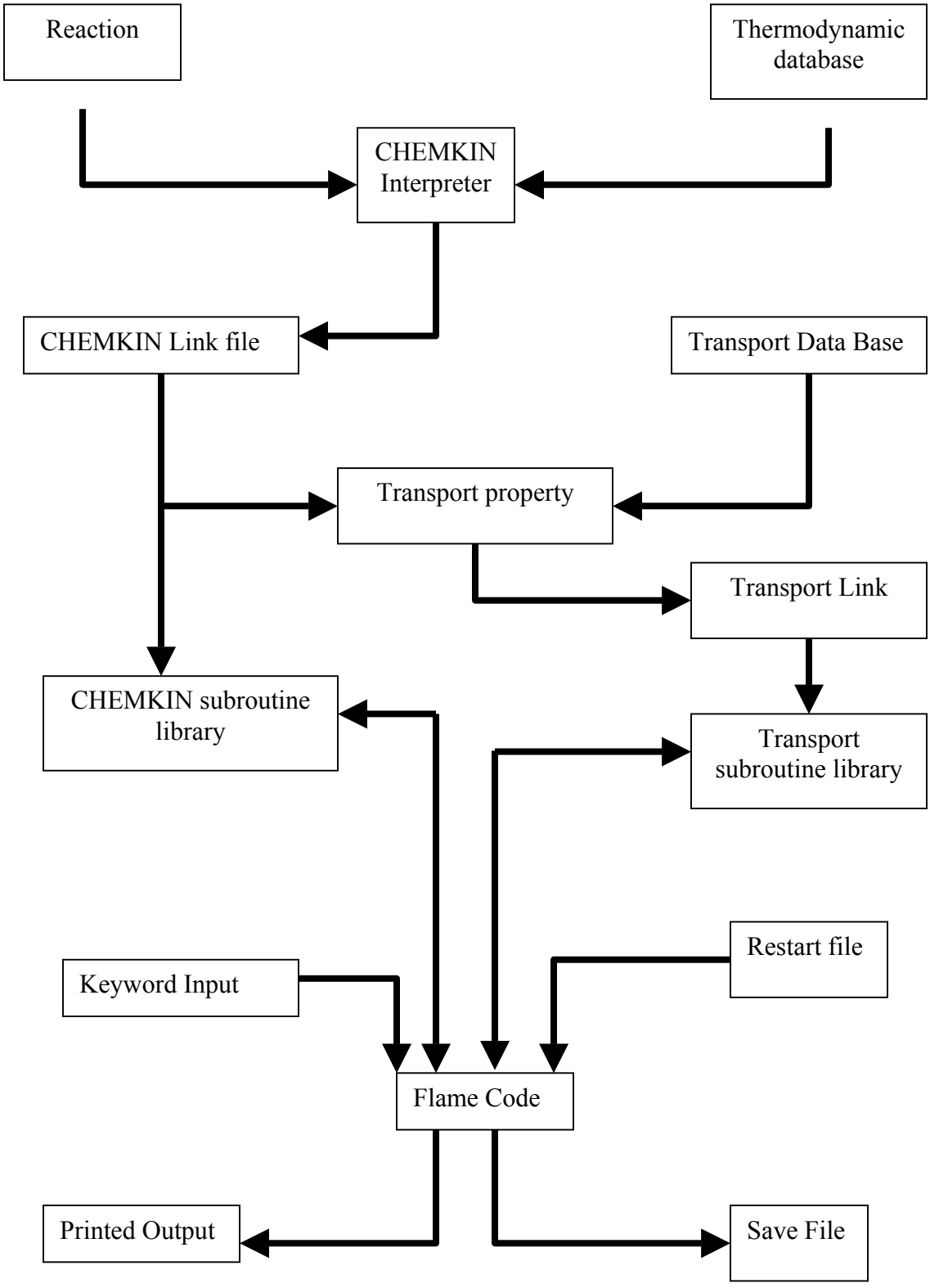

Figure C.1. Structure of the CHEMKIN code.

data bases, the loading of subroutines from several libraries, and the passing of files from one process to another. Figure C.1 shows the flow chart of the CHEMKIN code.

The first step executes the CHEMKIN interpreter. It reads the user-supplied information about the species and chemical reactions for a particular reaction mechanism. It then extracts further information about the species thermodynamic properties from a data base. This information is stored in the CHEMKIN linking file, a file that is needed by the transport property-fitting program TRANFIT and later by the CHEMKIN subroutine library, which is accessed by the flame-model program.

The next program that is executed is the TRANFIT program. It needs input data from a transport property database and from the CHEMKIN subroutine library. Its purpose is to compute polynomial representations of the temperature dependent parts of the individual species viscosities, thermal conductivities and binary diffusion coefficients. Like the CHEMKIN interpreter, the TRANFIT program produces a linking file that is later needed in the transport-property subroutine library, which will evaluate mixture properties during the course of flame computation.

The CHEMKIN and the transport subroutine libraries must be initialized before use and the flame program makes the appropriate initialization calls. The purpose of the initialization is to read the linking files and set up the internal working and storage space required by all subroutines in the libraries.

The input that defines a particular flame and the parameters needed to solve it are read by the flame program in keyword format. The flame program can begin iteration from a previously computed flame solution. In this case the old solution is read from a

restart file. The program saves the solution, which can be used to continue iterating or can be read as a starting estimate for a different flame.

C.3 Numerical Method Used

In the premixed laminar quasi-one dimensional (flat) flame, the following assumptions were made in modeling the flame. steady state, isobaric system, and the Dufour effect as well as external forces were negligible. The flame equations may then be written as:

Conservation of mass. $\dot{M} = \rho u A$ (C.1)

Energy conservation.

$$\dot{M}\frac{dT}{dx} - \frac{1}{c_p}\frac{d}{dx}(\lambda A\frac{dT}{dx}) + \frac{A}{c_p}\sum_{k=1}^{K}\rho Y_k V_k c_{pk}\frac{dT}{dx} + \frac{A}{c_p}\sum_{k=1}^{K}\dot{w}_k h_k W_k = 0 \qquad \text{(C.2)}$$

Species continuity.

$$\dot{M}\frac{dY_k}{dx} + \frac{d}{dx}(\rho A Y_k V_k) - A\dot{w}_k W_k = 0 \qquad (k = 1, 2, \ldots, K) \qquad \text{(C.3)}$$

Equation of state. $\rho = \frac{p\overline{W}}{RT}$ (C.4)

where $\dot{M}$ is the mass flow rate, ρ is the mass density, u is the velocity of the fluid mixture, A is the area expansion ratio, T is the temperature, x is the spatial coordinate, c_p is the constant pressure heat capacity of the mixture, λ is the thermal conductivity of the mixture, Y_k is the mass fraction of the k th species (there are K species), V_k is the diffusion velocity of the k th species, c_{pk} is the constant pressure heat capacity of the k th

species, $\dot{w}_k$ is the molar rate of production of the k th species, h_k is the specific enthalpy of the k th species, W_k is molecular weight of the k th species, $\overline{W}$ is the mean molecular weight of the mixture, p is the pressure, and R is the universal gas constant.

C.4 Modeling of thermodynamic properties

Conventionally specific heats, standard state enthalpies and standard state entropies are expressed by polynomial fits of arbitrary orders. Seven-parameter fits developed by Gordon and McBride (1971) at NASA are used. These fits take the following form.

$$\frac{C_{pk}^0}{R} = a_{1k} + a_{2k}T + a_{3k}T^2 + a_{4k}T^3 + a_{5k}T^4 \tag{C.5}$$

$$\frac{H_k^0}{R} = a_{1k} + \frac{a_{2k}}{2}T + \frac{a_{3k}}{3}T^2 + \frac{a_{4k}}{4}T^3 + \frac{a_{5k}}{5}T^4 + \frac{a_{6k}}{T} \tag{C.6}$$

$$\frac{S_k^0}{R} = a_{1k}\ln T + a_{2k}T + \frac{a_{3k}}{2}T^2 + \frac{a_{4k}}{3}T^3 + \frac{a_{5k}}{4}T^4 + a_{7k} \tag{C.7}$$

Other thermodynamic properties are then calculated in terms of these parameters. To account for the variation of these properties with the temperature, two sets of seven coefficients are calculated, one for low temperature (300 - 1000 K) and one for high temperature (1000 – 3000 K).

C.5 Transport processes

The dominant transport processes in flames are diffusion, thermal conduction and thermal diffusion. As stated earlier, viscosity effects are neglected. Thermal conductivities and diffusion coefficients for the individual species are estimated using

methods available in the literature. For example, diffusion velocity is assumed to be composed of three parts. ordinary diffusion velocity V_k , thermal diffusion velocity ψ_k, and correction velocity V_c (included to make sure that the mass fractions sum to unity).

$$V_k = \nu_k + \psi_k + V_c \tag{C.8}$$

$$\upsilon_k = -D_k \frac{1}{X_k} \frac{dX_k}{dx} \tag{C.9}$$

$$D_k = \frac{1 - Y_k}{\sum_{j \neq k}^{K} X_j / D_{kj}} \tag{C.10}$$

$$\Psi_k = \frac{D_k k_{T_k}}{X_k} \frac{1}{T} \frac{dT}{dx} \tag{C.11}$$

where X_k is the mole fraction, D_k is the mixed average diffusion coefficient, D_{kj} is the binary diffusion coefficient, and K_{T_k} is the thermal diffusion ratio.

C.6 Boundary conditions

The burner surface is taken as cold boundary and a distance far away from the burner, usually 30 mm from the burner surface, represents the hot boundary. For premixed flame, $\dot{M}$ is a known constant. Temperature and mass flux fractions at the cold boundary are specified. Vanishing gradients are imposed at the hot boundary.

C.7 Modeling results and comparison with experimental data.

The fuel-rich cyclohexane flame was modeled using CHEMKIN. The reactions for production of triacetylene, styrene, indene and naphthalene were added into the existing mechanism of stoichiometric cyclohexane flame. The total number of species considered in the set of 891 reactions is 105. The temperature profile that was measured for this particular flame, in the UMass Amherst lab was used in the modeling.

The model results are compared here for the major species.

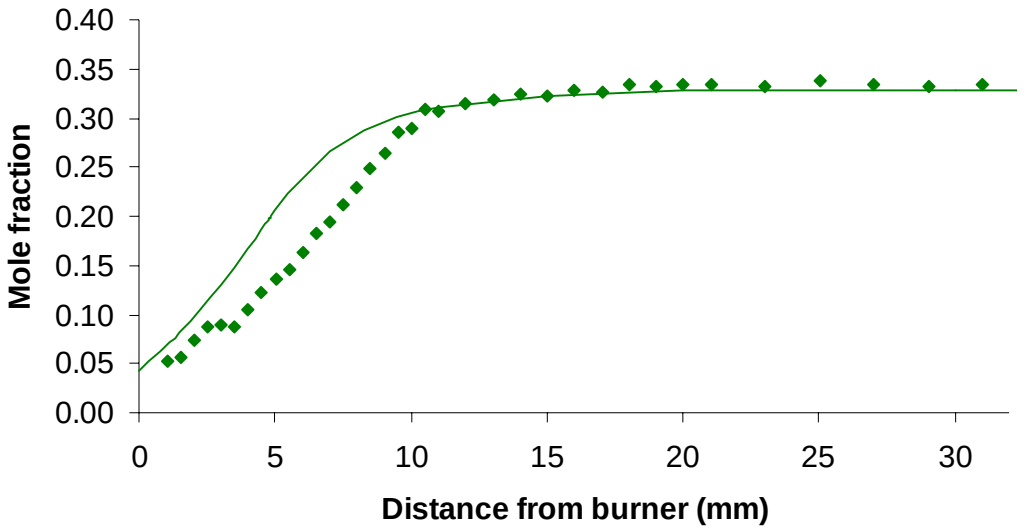

Figure C.2. Comparison of code result and experimental result for production of CO (the line represents model prediction, the diamonds represents experimental results).

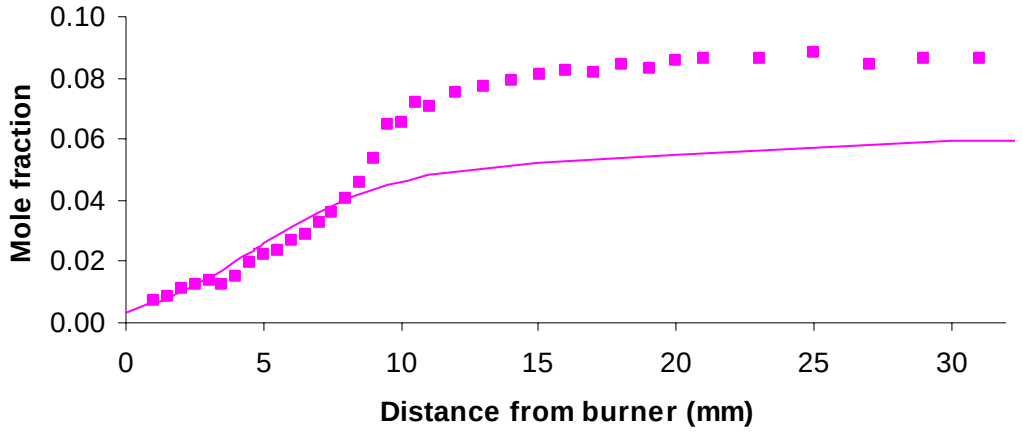

Figure C.3. Comparison of code result and experimental result for production of CO_2 (the line represents model prediction, the squares represents experimental results).

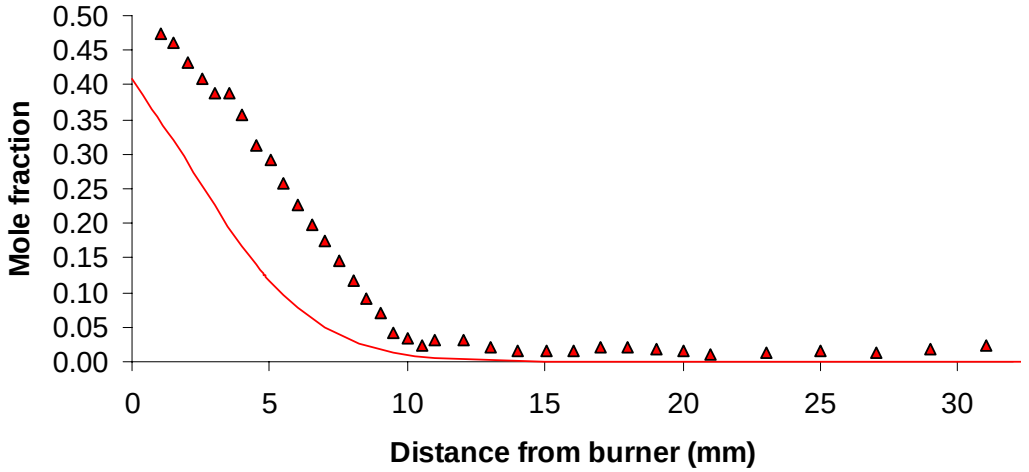

Figure C.4. Comparison of code result and experimental result for consumption of O_2 (the line represents model prediction, the triangles represents experimental results).

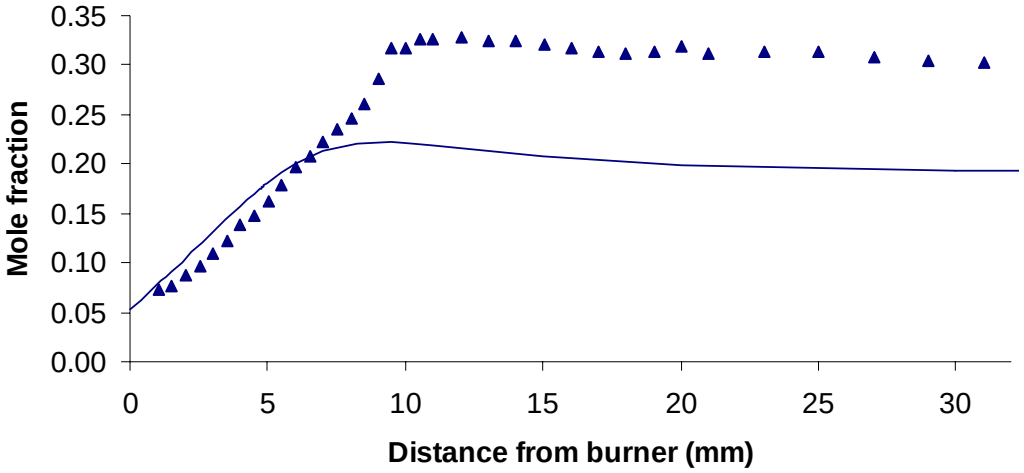

Figure C.5. Comparison of code result and experimental result for production of H_2O (the line represents model prediction, the triangles represents experimental results).

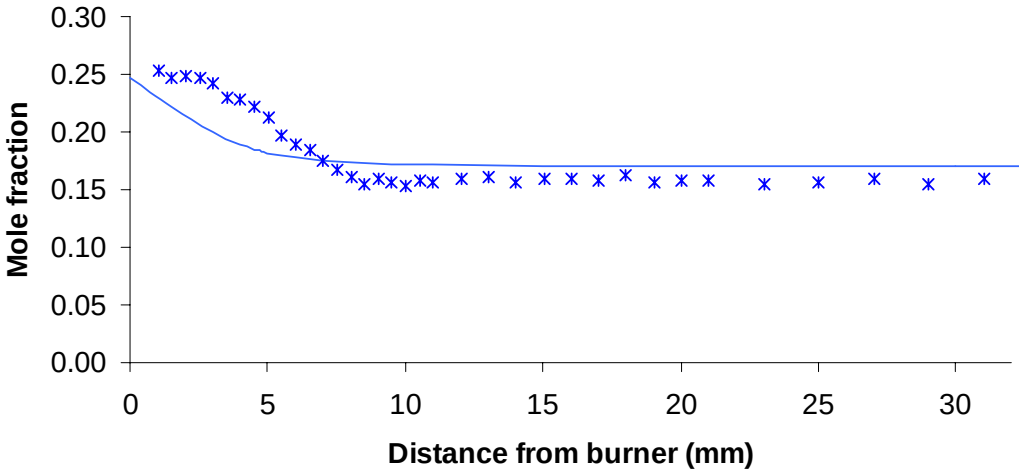

Figure C.6. Comparison of CHEMKIN code result and experimental result for production of Ar (the line represents model prediction, the stars represents experimental results).

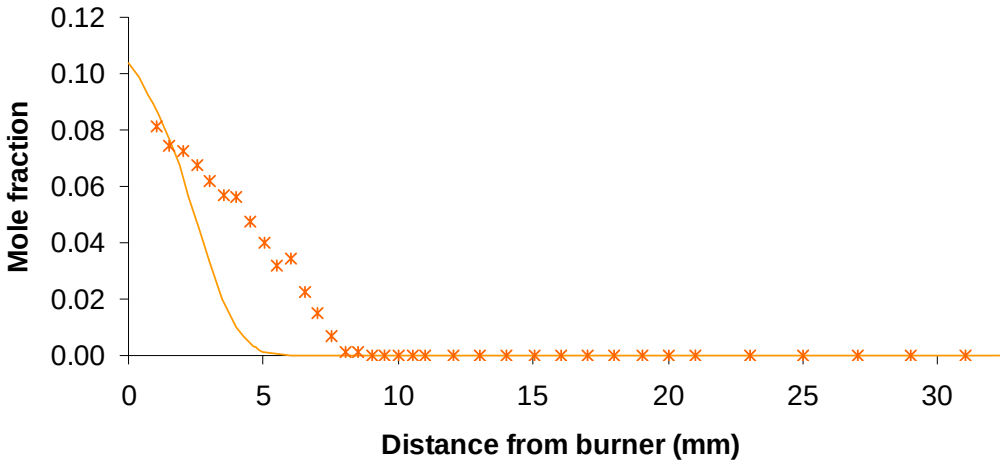

Figure C.7. Comparison of code result and experimental result for cyclohexane oxidation (the line represents model prediction, the stars represents experimental results).

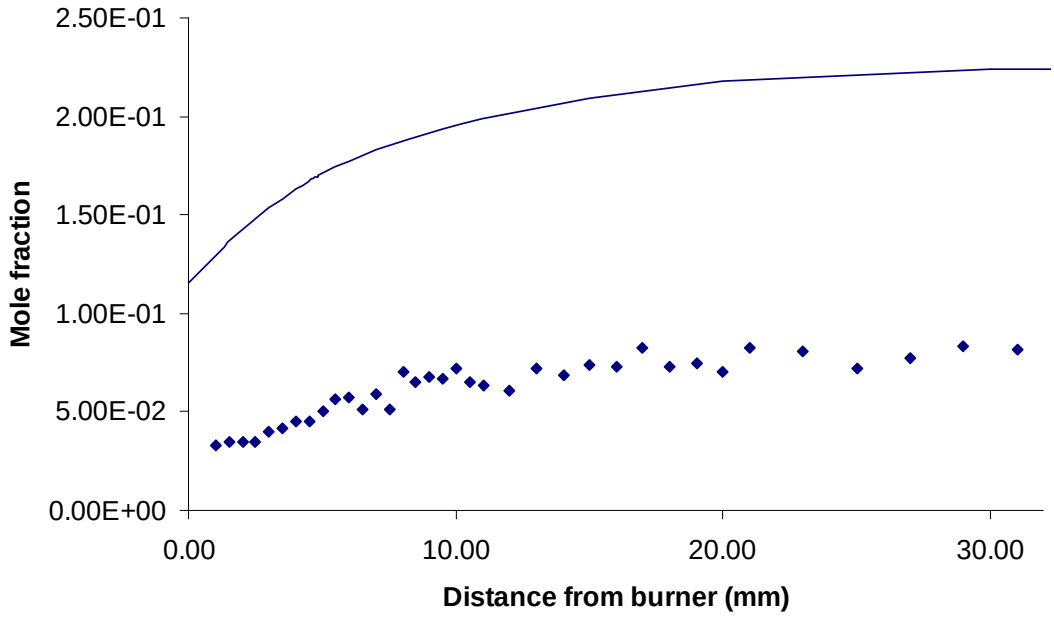

Figure C.8. Comparison of code result and experimental result for H_2 productin (the line represents model prediction, the stars represents experimental results).

The results show qualitative similarity in the shape for all the species compared. For CO and Ar, the model prediction and experimental result matches well. For CO_2, O_2 , and H_2O production, the model underpredicts the experiment. For cyclohexane combustion, the model predicts a faster combustion of cyclohexane compared to the experiment. For H_2 the model overpredicts the experimental findings by almost 4 times. This deviation is a major concern. The overprediction of H_2 and underprediction of H_2O suggest that H_2 and O_2 reactions in the mechanism need to be reinvestigated.

C.8 Reaction pathway analysis of the cyclohexane flame

Using the mechanism file for the code and its prediction, a SENKPLOT analysis was done to find out the major reaction pathways for this mechanism in the fuel-rich cyclohexane flame. Figure C.9 shows the major reaction pathways, where CYC6H12 refers to the cyclohexane, A refers to benzene, and CY refers to cyclic species. The reaction pathway analysis shows that cyclohexane forms cyclohexyl radical first, which then opens and forms a linear species. This species upbeat-scissions into C_4H_7 and C_2H_4. C_4H_7 further breaks up into 1,3-butadiene (iiiC_4H_6). 1,3-Butadiene breaks up into C_2H_4 and C_2H_3. C_2H_2 forms HCCO and CO. HCCO further gets oxidized to CO. C_2H_3 gets oxidized to HCO, which forms CO. CO then gets oxidized by OH to form CO_2.

The pathway analysis also suggests that hydrogen abstraction reactions of cyclohexane are the major benzene formation reactions for this particular flame, which supports the findings of (Law, 2005) for a stoichiometric cyclohexane flame.

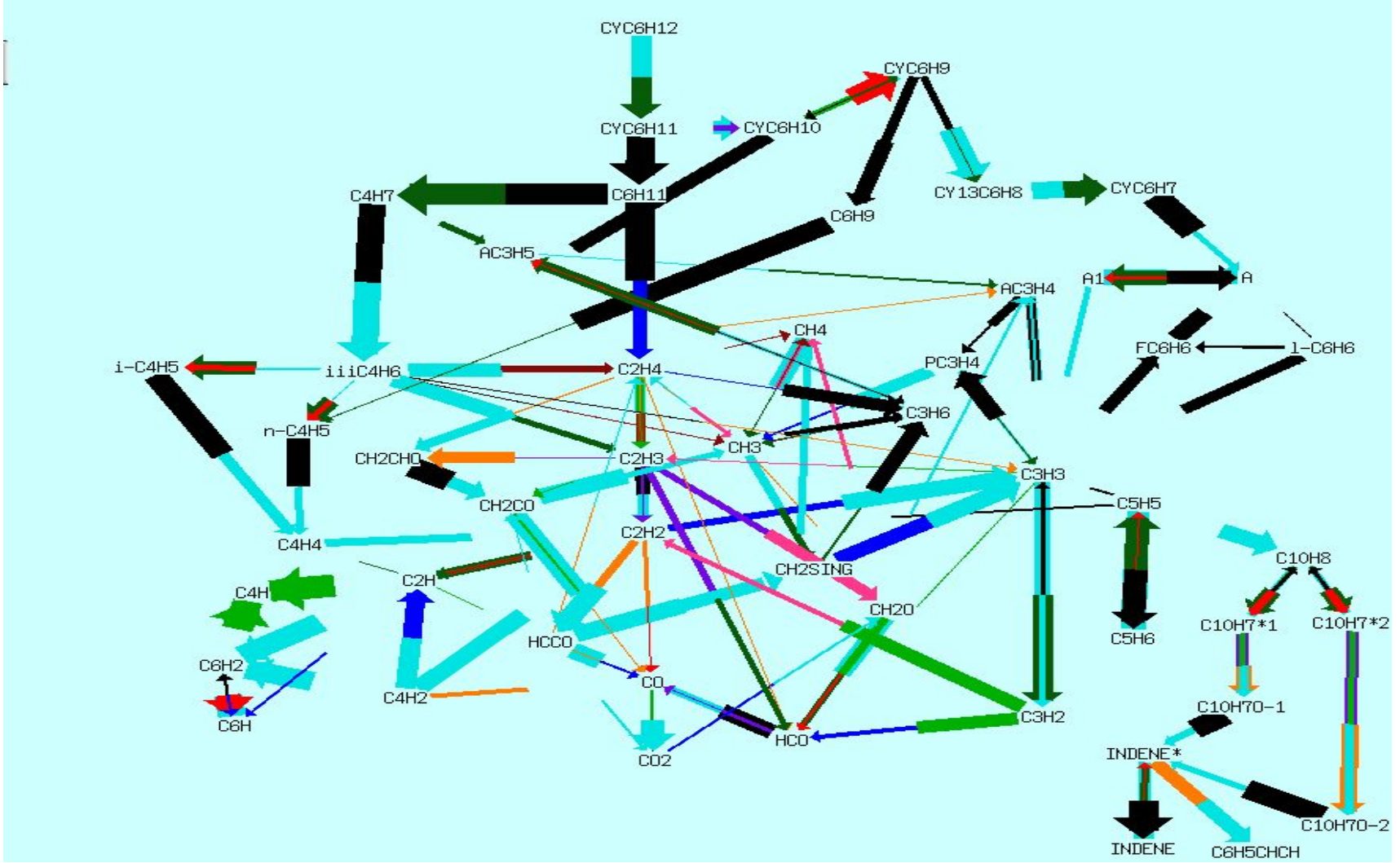

Figure C.9. Major reaction pathways for the cyclohexane flame.

BIBLIOGRAPHY

Anderson, J. B., Andres, R. P., and Fenn, J. B., "Advances in atomic and molecular physics, Vol. 1," Bates, D. R., and Easterman, I. (eds.), Academic Press, New York (1965), p 347.

Atakan, B., Lamprecht, A., and Kohse-Höinghaus, K., "An experimental study of fuel-rich 1,3-pentadiene and acetylene/propene flames," *Combustion and Flame*, 133, 431-440, 2003.

Bhargava, A., "A molecular beam mass spectrometry study and modeling of ethylene flames," Ph. D. Dissertation, Department of Chemical Engineering, University of Massachusetts Amherst (1997).

Biordi, J. C., Lazzara, C. P., and Papp, J. F., "Flame structure studies of CF_3Br – inhibited methane flames," *Proceedings of the Combustion Institute*, 14, 367-381, 1973.

Biordi, J. C., Lazzara, C. P., and Papp, J. F., "Molecular beam mass spectrometry applied to determining the kinetics of reactions in flames. I. Empirical characterization of flame perturbation by molecular beam sampling probes," *Combustion and Flame, 23*, 73 – 82, 1974.

Biordi, J. C., "Molecular beam mass spectrometry for studying the fundamental chemistry of flames," *Progress in Energy and Combustion Science*, 3, 151-173, 1977.

Borghi, R., and Destriau, M., "Combustion and Flames: Chemical and Physical Principles," Editions Technip (1998), p 85.

Brosi, A. R., and Harkins, W. D., "The abundance ratio of the isotopes of natural and isotopically separated carbon," *Physical Review*, 52, 472 – 474, 1937.

Busch maintenance and repair manual, models 0010 through 0100 R5 – Series single stage rotary vacuum pumps.

Calcote, H. F., "Mechanism of soot nucleation in flames. A critical review," *Combustion and Flame*, 42, 215-242, 1981.

Chernushevich, I. V., Loboda, A. V., and Thomson, B. A., "An introduction to quadrupole-time-of-flight mass spectrometry," *Journal of Mass Spectrometry*, 36, 849-865, 2001.

Collaboratory for Multi-Scale Chemical Science, ALS Low Pressure Flames website,https.//cmcs.ca.sandia.gov/cmcs/portal/group/ALS_Low_Pressure_Flames/js_pane/200.

Cool, T. A., Nakajima, K., Mostefaoui, T. A., Qi, F., Mcllroy, A., Westmoreland, P. R., Law, M. E., Poisson, L., Peterka, D. S., and Ahmed, M., "Selective detection of isomers with photoionization mass spectrometry for studies of hydrocarbon flame chemistry ," *Journal of Chemical Physics*, 119, 8356 – 8365, 2003.

Dehmer, P. M., "Photoionization of OH in the region 750-950 A° ," *Chemical Physics Letters*, 110, 79-84, 1984.

Dixon-Lewis, G., "Kinetic mechanism, structure & properties of premixed flames in Hydrogen-Oxygen-Nitrogen mixtures," *Philosophical Transactions of the Royal Society of London*, Series A, Mathematical and Physical Sciences, 292, 1388, 45-99, 1979.

Fristrom, H. M., "Flame Structure and Processes," Oxford University Press, New York (1995), pp 3, 17, 23.

Holland, D. M. P., Shaw, D. A., McSweeney, S. M., MacDonald, M. A., Hopkirk, A., and Hayes, M. A., "A study of the absolute photoabsorption, photoionization and photodissociation cross sections and the photoionization quantum efficiency of oxygen from the ionization threshold to 490Å," *Chemical Physics*, 173, 315-331, 1993.

Homann, K. H., and Wagner, H. G., "Chemistry of carbon formation in flames," *Proceedings of Royal Society of London, Series A, Mathematical and Physical Sciences*, 307, 1489, 141-152, 1968.

Kee, R. J., Grcar, J. F., Smooke, M. D., and Miller, J. A., "A Fortran computer package for the evaluation of gas-phase multicomponent transport properties," SAND 87-8246, Sandia National Laboratories, Livermore, California (1986), Modification of TRANLIB version 1.6, 1990.

Kee, R. J., Rupley, F. M., and Miller, J. A., " The CHEMKIN thermodynamic database," SAND 87-8215, Sandia National Laboratories, Livermore, California (1987).

Kent, J. H., "A noncatalytic coating for platinum-rhodium thermocouples, " *Combustion and Flame*, 14, 279-288, 1970.

Knuth, E. L., "Engine emissions. Pollutant formation and measurement," Springer G. S. and Patterson D. J. (eds), Plenum Publishing, New York (1973), p 320.

Koizumi, H., "Predominant decay channel for superexcited organic molecules," *Journal of Chemical Physics*, 95, 5846-5852, 1991.

Kramers, S., "Heat transfer from spheres to flowing media," *Physica*, 12, 61-68, 1946.

Law, M. E., "Molecular-beam mass spectrometry of ethylene and cyclohexane flame," Ph. D. Dissertation, Department of Chemical Engineering, University of Massachusetts Amherst, (2005).

Marr, G. V., "Photoionization process in gases," Academic Press, New York/London (1967), p 1.

McEnally, C. S., and Pfefferle, L. D., "Experimental study of fuel decomposition and hydrocarbon growth processes for cyclohexane and related compounds in nonpremixed flames," *Combustion and Flame*, 136, 155-167, 2004.

Morel, A., "Molecular beam mass spectrometric measurements on propene and related flames," M. S. Dissertation , Department of Chemical Engineering, University of Massachusetts Amherst (2005).

Nicholson, A. J. C., "Photo-ionization efficiency curves. Measurement of ionization potentials and interpretation of fine structure," *The Journal of Chemical Physics*, 39, 954-961, 1963.

NIST Chemistry WebBook, http.//webbook.nist.gov/chemistry/, 2005.

Omega Engineering Inc., "The temperature handbook," 2nd Edition, 2000.

Öktem, B., Tolocka, M. P., Zhao, B., Wang, H., and Johnston, M. V., "Chemical species associated with the early stage of soot growth in laminar premixed ethylene-oxygen-argon flame," *Combustion and Flame*, 142, 364-373, 2005.

Palenius, H. P., Kohl, J. L., and Parkinson, W. H., "Absolute measurement of the photoionization cross-section of atomic hydrogen with a shock tube for the extreme ultraviolet," *Physical Review A*, 13, 1805-1816, 1976.

Samson, J. A. R., and Pareek, P. N., "Absolute photoionization cross sections of atomic oxygen," *Physical Review A*, 31, 1470-1476, 1985.

Samson, J. A. R., and Stolte, W. C., "Precision measurements of the total photoionization cross-sections of He, Ne, Ar, Kr, and Xe," *Journal of Electron Spectroscopy and Related Phenomena*, 123, 265-276, 2002.

Shaddix, C. R., "Correcting thermocouple measurements for radiation loss. A critical review", *Proceedings of the 33rd National Heat Transfer Conference*, 1-10, 1999.

Smyth, K. C., and Miller, J. H., "Chemistry of molecular growth processes in flames," *Science*, 236, 1540-1546, 1987.

Stavropoulos, P., Michalakou A., Skevis G., and Couris S., "Quantitative local equivalence ratio determination in laminar premixed methane-air flames by laser induced breakdown spectroscopy (LIBS)," *Chemical Physics Letters*, 404, 309-314, 2005.

Taatjes, C. A., Hansen, N., Mcllroy, A., Miller, J. A., Senosiain, J. P., Klippenstein, S. J., Qi, F.,Sheng, L., Zhang, Y., Cool, T. A., Wang, J., Westmoreland, P.R., Law, M. E., Kasper, T., Hoinghaus, K. K., "Enols are common intermediates in hydrocarbon oxidation," *Science*, 308, 1887 – 1889, 2005.

Turbiez, A., Devynck P., Desgroux P., and Pauwels, J. F., "Coupling of gas chromatography and molecular beam/mass spectrometry analytical techniques. Application to flame structure study," *Review of Scientific Instruments*, 70, 2828 – 2835, 1999.

Wang, H., and Frenklach, M., "A detailed kinetic modeling study of aromatics formation in laminar premixed acetylene and ethylene flames," *Combustion and Flame*, 110, 173-221, 1997.

Westmoreland, P. R., Dean, A. M., Howard, J. B., and Longwell, J. P., "Forming benzene in flames by chemically activated isomerization," *Journal of Physical Chemistry*, 93, 8171-8180, 1989.

Weissman, M., and Benson, S. W., "Pyrolysis of methyl chloride, a pathway in the chlorine-catalyzed polymeriazation of methane," *International Journal of Chemical Kinetics*, 16, 307-333, 1984.

Zervas, E., Montagne, X., and Lahaye, J., "Influence of fuel and air/fuel equivalence ratio on the emission of hydrocarbons from a SI engine. 1. Experimental findings," *Fuel*, 83, 2301-2311, 2004.